3-26-2015

Advancements of In-Flight Mass Moment of Inertia and Structural Deflection Algorithms for Satellite Attitude Simulators

Jonathan W. Wright

Follow this and additional works at: https://scholar.afit.edu/etd

Part of the Aerospace Engineering Commons

Recommended Citation

**ADVANCEMENTS OF IN-FLIGHT MASS
MOMENT OF INERTIA AND STRUCTURAL
DEFLECTION ALGORITHMS FOR
SATELLITE ATTITUDE SIMULATORS**

DISSERTATION

Jonathan W. Wright, Captain, USAF

AFIT-ENY-DS-15-M-261

**DEPARTMENT OF THE AIR FORCE
AIR UNIVERSITY**

AIR FORCE INSTITUTE OF TECHNOLOGY

Wright-Patterson Air Force Base, Ohio

ADVANCEMENTS OF IN-FLIGHT MASS MOMENT

OF INERTIA AND STRUCTURAL DEFLECTION ALGORITHMS

FOR SATELLITE ATTITUDE SIMULATORS

DISSERTATION

Presented to the Faculty

Graduate School of Engineering and Management

Air Force Institute of Technology

Air University

Air Education and Training Command

in Partial Fulfillment of the Requirements for the

Degree of Doctor of Philosophy

Jonathan W. Wright, BAE, MS

Captain, USAF

26 March 2015

AFIT-ENY-DS-15-M-261

ADVANCEMENTS OF IN-FLIGHT MASS MOMENT

OF INERTIA AND STRUCTURAL DEFLECTION ALGORITHMS

FOR SATELLITE ATTITUDE SIMULATORS

Jonathan W. Wright, BAE, MS
Captain, USAF

Committee Membership:

Dr. E. D. Swenson
Chair

Dr. R. G. Cobb
Member

Dr. F. A. Leve
Member

Dr. D. R. Jacques
Member

ADEDEJI B. BADIRU, PhD
Dean, Graduate School of
Engineering and Management

AFIT-ENY-DS-15-M-261

Abstract

Experimental satellite attitude simulators have long been used to test and analyze control algorithms in order to drive down risk before implementation on an operational satellite. Ideally, the dynamic response of a terrestrial-based experimental satellite attitude simulator would be similar to that of an on-orbit satellite. Unfortunately, gravitational disturbance torques and poorly characterized moments of inertia introduce uncertainty into the system dynamics leading to questionable attitude control algorithm experimental results. This research consists of three distinct, but related contributions to the field of developing robust satellite attitude simulators. In the first part of this research, existing approaches to estimate mass moments and products of inertia are evaluated followed by a proposition and evaluation of a new approach that increases both the accuracy and precision of these estimates using typical on-board satellite sensors. Next, in order to better simulate the micro-torque environment of space, a new approach to mass balancing satellite attitude simulator is presented, experimentally evaluated, and verified. Finally, in the third area of research, we capitalize on the platform improvements to analyze a control moment gyroscope (CMG) singularity avoidance steering law. Several successful experiments were conducted with the CMG array at near-singular configurations. An evaluation process was implemented to verify that the platform remained near the desired test momentum, showing that the first two components of this research were effective in allowing us to conduct singularity avoidance experiments in a representative space-like test environment.

iv

to my loving and supportive family

Acknowledgements

First, I would like to thank my advisor Dr. Swenson. The lessons you taught while I was a master's student were some of the most memorable I've had and I'm truly glad I was able to study under you when returning to AFIT for my Ph.D. Dr. Cobb and Dr. Jacques, thank you for your insight and wisdom. It has truly been a pleasure being a student in your classroom and I sincerely thank you for the guidance you've provided me. Dr. Leve, thank you for your willingness to provide me with the firsthand knowledge of your steering law as well as always providing helpful feedback to numerous rewrites. Gentlemen, without your help, guidance, and wisdom this wouldn't have been possible.

I would like to thank my family for their love and support. I would like to thank my sister for always challenging me to challenge myself. Most of all, I'd like to thank my wife for her encouragement and support when I felt I had challenged myself too much.

<div align="right">Jonathan W. Wright</div>

Table of Contents

List of Figures

List of Tables

List of Abbreviations

ADVANCEMENTS OF IN-FLIGHT MASS MOMENT

OF INERTIA AND STRUCTURAL DEFLECTION

ALGORITHMS FOR SATELLITE ATTITUDE SIMULATORS

I. Introduction

Satellite attitude simulators have long been used to test satellite attitude controllers that may not be ready for on-orbit implementation on operational satellites [32]. In order to make inferences as to the on-orbit performance of a controller, the terrestrial-based satellite attitude simulator should respond to the controller in the same manner as the satellite will. Unlike on-orbit satellites that operate in micro-torque environments, satellite attitude simulators are exposed to potentially large gravitational disturbance torques. This research has three distinct, but related contributions to the field of developing robust satellite attitude simulators. In the first part of this research, existing approaches to estimate mass moments and products of inertia are evaluated followed by a proposition and evaluation of a new approach that increases both the accuracy and precision of these estimates using typical on-board satellite sensors. Next, in order to attempt to simulate a micro-torque environment, a new approach to balancing to counteract three different types of gravitational disturbance torques is implemented and verified. Finally, in the third area of research, several experiments were conducted on a new singularity avoidance algorithm that had only been previously validated analytically. In these experiments, the contributions of the first two areas of research were included which resulted in an experimental evaluation of this new steering law on a well-characterized terrestrial-based satellite simulator conducting maneuvers in a nearly micro-torque environment.

1.1 Research Motivation

Terrestrial-based satellite attitude simulators are typically used to test controller algorithms that may be too risky to operationally test after only numerical simulation. The attitude simulators act as a stepping stone to help increase the technology readiness level of these controllers and decrease the risk of implementation on operational satellites. If the satellite simulator is incorrectly characterized, then the experimental results of a controller that may otherwise be successful instead may result in inconclusive, false negative or false positive results. An example of this can be seen in our previous research attempting to experimentally validate a single-gimbal control moment gyroscope (CMG) steering law called Hybrid Steering Logic (HSL) on a terrestrial-based satellite attitude simulator Simulation Satellite (SimSat) [41]. Hybrid steering logic is a steering law for a four single gimbal control moment gyroscope (SGCMG) array that is intended to avoid singularities associated with SGCMG arrays which will be discussed in much more detail in Chapter V. After implementing three experimental maneuvers, two of which were deemed successful and the third experimental maneuver was deemed inconclusive as none of the steering laws, HSL included, were able to avoid the singularity. While attempting to analyze the inconclusive results we determined that there was very little additional information that could be gathered. Although we could and did compare the estimated angular momentum of the spacecraft to the angular momentum of the CMG–as they should be equal and opposite–all we were able to do was confirm our suspicions that the values were not equal and opposite meaning we had either a poorly characterized platform moment of inertia (MOI), poorly characterized CMG angular momentum, uncharacterized external disturbance torques, or any combination of the three.

After obtaining inconclusive results while testing the CMG steering algorithms, we decided that instead of delving deeper into why we obtained inconclusive results we

would attempt to avoid CMG singularity by calculating the desired controls a-priori and implementing a feed-forward control solution. After researching McFarland's [26] work on the implementation of feed-forward optimal control solutions on using the onboard reaction wheel (RW) array, we concluded that the current limiting factor on SimSat is not the implementation of control algorithms, but the agreement between the dynamics of SimSat and our simulator models. This disagreement was theorized to be primarily in the form of MOI mischaracterization and uncharacterized disturbance torques. It was therefore concluded that in order to move forward we need to take what appeared to be a step back and advance the characterization methodologies of terrestrial-based satellite attitude simulators. Accomplishing the increased characterization will give us a better understanding of the research platforms and allow us to better identify the error sources that are leading to inconclusive research. Additionally, the increased characterization will allow us to examine research topics that we are currently unable to implement such as accurate feed-forward optimal control solutions.

1.2 Problem Statement

Previous research by McFarland [26] suggests the need for higher precision and accuracy in the mass and torque characterization of a terrestrial-based satellite attitude simulator to thoroughly analyze the feed-forward implementation of optimal control solutions. While attempting to implement near real-time optimal control solutions, McFarland experienced difficulties in experimental implementation of optimal control solutions due to uncharacterized disturbance torques and errors in MOI estimates that led to a constant need to re-calculate the optimal control solution. With better characterization of the MOI and a better model of the disturbance torques the calculated optimal control solution will remain valid longer allowing for more time to

calculate the updated optimal control solution.

1.3   Research Objectives

The objective of this research is to develop novel methodologies to reduce the errors introduced when attempting to validate simulation results on an experimental platform. This research first focuses on developing and evaluating a new method to increase the precision and accuracy of the mass MOI estimate. Next, this research will develop a novel methodology to identify and decrease the disturbance torques that satellite attitude simulators are constantly exposed to. Finally, this research will take advantage of the increase in precision and accuracy of the MOI method developed in Chapter III and the decrease in gravitational disturbance torques developed in Chapter IV to experimentally analyze the SGCMG steering logic known as HSL developed by Leve [22].

1.4   Method Overview

The research presented in Chapter III begins with the analysis of previous MOI characterization methodologies and assumptions. Once the methodologies were thoroughly analyzed, we identified irregularities in the response to a common estimation maneuver. We then developed an estimation maneuver specifically to allow for better curve fitting of the sensor measurements to increase precision. To increase accuracy of the MOI estimates, additional steps are taken to correct for zero-order disturbance torques. Finally, the sensitivity to first-order disturbance torques is analyzed, the first-order disturbance torques are estimated, and a novel method for the correction of the first-order disturbance torques during post-processing is implemented.

Chapter IV presents the research in expanding on the post-processing correction of first-order disturbance torques presented in Chapter III and develops and exper-

imentally verifies a dynamic balancing method to correct of disturbance torques up to the third order. We begin by experimentally identifying verifying the presence of first-order torques other than an imbalance in the $Z-$axis, the body axis that is perpendicular to the plane of the satellite's tabletop. We then derive the equations for the disturbance torques resulting from structural deflection and identify a first-order component. Structural reinforcements are added to SimSat and the process to identify first-order torques was repeated. Finally, linear actuators were added to SimSat and a controller was developed to move masses to counteract first- to third-order disturbance torques.

Chapter V presents the experimental implementation and analysis of the HSL steering law developed by Leve [22] on SimSat. During his research, Leve conducted simulations to analyze how HSL performed when compared against the two steering laws that HSL is comprised of, Singular Direction Avoidance (SDA) and Local Gradient (LG). The comparison of the three steering laws was made during a single maneuver repeated three times to account for three different starting configurations of the CMG array–away from singularity, near a hyperbolic singularity, and near an elliptic singularity. Each of the three steering laws completed the same three maneuvers and the steering laws were then compared based on the amount of null-motion and torque error during the maneuver. We repeated the previously inconclusive experiment HSL experiment implemented on SimSat [41] by selecting the same HSL tuning parameters and conducting the same maneuvers that had previously been analyzed in simulation by Leve [22]. In addition to the steering-law induced null-motion and torque error, non-simulated hardware constraints such as a gimbal rate limitation of 1.5 rad/s was also taken into considered. When the maximum gimbal rates were exceeded an additional torque error independent of the three steering laws was experienced and analyzed. In addition to a direct comparison of HSL, SDA, and LG

conducted during this round of experimentation, we analyzed the benefit of increased characterization on the ability to draw additional conclusions about the validity of the experiment as well as any additional characterizations that may be required. Furthermore, the updated experimental results were compared against the previous experimental results for a better identification of what may have been the source of the original inconclusive results in an attempt to better validate the steering laws and obtain better agreement between future simulations and experiments.

1.5   Research Contributions

A novel method to increase the both the precision and accuracy of in-flight mass MOI and product of inertia (POI) of a satellite attitude simulator has both immediate and future impact. To begin with, an immediate impact of the increased precision of in-flight MOI estimation is that previous research in the field of in-flight MOI estimation as a means-to-an-end now become much more viable. Two notable examples are Dabrowski's [6] research into the identification of parasitic satellites and Geitgey's [11] research on using MOI estimates to estimate the remaining onboard fuel. The results of both research topics relied on the precision of the MOI estimation methodology and an increase in the precision of in-flight MOI estimation results in more viability of these two capabilities.

The future contributions of increasing the precision and accuracy of mass characterization and disturbance torque correction are an increased confidence in experimental results and the ability to conduct experimental research on controllers that require a higher fidelity of characterization than is currently available. One example of a controller that requires higher accuracy MOI and disturbance torque characterizations is feed-forward optimal-control solutions. Previous research in the implementation of near real-time optimal-control solutions by McFarland [26] had difficulties in experi-

6

mental implementation due to uncharacterized disturbance torques and errors in MOI estimates leading to a constant need to re-calculate the optimal control solution. With better characterization of the MOI and a better model of the disturbance torques the calculated optimal control solution will remain valid longer allowing for more time to calculate the updated optimal control solution. Although this represents a single case, the experimental implementation of feed-forward optimal control solutions is only representative of an entire class of controllers that cannot currently be implemented. The ability to implement this class of controllers will greatly increase the functionality of satellite attitude simulators. In addition to implementing controllers that cannot currently be implemented, an increased characterization and disturbance torque reduction will allow for better experimental validation of simulated results for all controllers. This would allow a more in-depth analysis of the controllers and will ultimately result in a more seamless technology transition to operational satellites.

1.6   Dissertation Overview

This dissertation has six chapters, of which Chapters III through V are independent scholarly articles which are explained in Sections 1.6.1- 1.6.3. Although each of the three articles presented in Chapters III through V include a brief overview of the previous research that was critical to the research conducted within each chapter, Chapter II presents broader, more in-depth overview of the previous research conducted on the three presented topics.

1.6.1   Mass Moment of Inertia Estimation for Terrestrial-Based Satellite Simulators.

Chapter III addresses the in-flight estimation of the mass moment of inertia. The estimation process was developed in order to increase precision by reducing the num-

ber of assumptions implemented during the estimation of the POI as well as increase accuracy by correcting for disturbance torques that had been previously ignored. Additionally, the methodology has the benefit that it is not subject to errors associated with time delays.

1.6.2 Experimental Identification and Correction of Disturbance Torques.

Chapter IV presents the development and experimental verification of an approach to identify and reduce three types of disturbance torques that contaminate the experimental results of terrestrial-based satellite attitude simulators. The previous research on disturbance torque characterization and on balancing of satellite attitude simulators include a rigid body assumption. Although this assumption may be valid for many satellite attitude simulators, the research presented in Chapter IV evaluates the validity of the rigid body assumption when attempting to balance a terrestrial-based satellite simulator. Once the assumption is deemed invalid, a new balancing methodology is developed. Unlike previous balancing methodologies which implemented the rigid body assumption–referred to as "static" balancing–this balancing methodology may vary as SimSat changes orientation resulting in a "dynamic" approach to balancing. As a result, Chapter IV covers the development, implementation, and experimental validation of a methodology to correct for a dynamic imbalance of a satellite attitude simulator necessary in the presence of structural deflection.

1.6.3 Hardware Testing of Hybrid Steering Logic.

Single gimbal control moment gyroscope arrays experience multiple types of singularities as will be explained in further detail in Chapter V. There are various steering laws able to avoid singularities, but most are best implemented in the proximity of

a specific type of singularity. Hybrid Steering Logic is a recently developed SGCMG steering law that has been shown in simulation to be able to avoid multiple types of singularities while inducing adverse effects of singularity specific steering laws. Chapter V presents the experimental results of Leve's [21] HSL algorithm on SimSat and consists of the comparison of HSL to LG and SDA. One of the main reasons it was included in this dissertation is that it represents one of the vital roles in 3-degree-of-freedom (DOF) satellite attitude simulators, analysis of CMG steering laws, and is a prime example to the importance of the reduction of gravitational disturbance torques. In this experimental validation of Leve's HSL algorithm, a single maneuver is repeated with the CMG in three different configurations. The reason the CMG are in these specific configurations is that the purpose of the research is to determine the controllers' ability to sense and avoid the singularities that the CMG array is in proximity to in two of these three orientations. The singularities in the CMG array are dependent on the angular momentum of the CMG array and the presence of large disturbance torques may cause the array to re-orient to a less singular configuration, resulting in inconclusive results. This effect would only be exacerbated for future research efforts into the hardware testing of singularity escape algorithms [38].

II. Related Work

In this chapter, we will discuss related work in MOI estimation, disturbance torque characterization, and dynamic balancing of satellites and satellite attitude simulators. For a comprehensive background paper on types of satellite simulators and various experiments conducted before 2003, we will refer the reader to a paper written by Schwartz [32]. The research presented in this dissertation concentrates on the previous research pertaining to mass characteristic estimation and automatic balancing methods with an emphasis on the disturbance torques that exist when attempting to implement a terrestrial-based satellite attitude simulator to estimate in-orbit attitude dynamics [34]. First, we will discuss the differences between the MOI estimation methods by looking at the equations of motion that govern satellite attitude dynamics.

2.1 Governing Equations of Satellite Attitude Dynamics

The primary equations for satellite attitude dynamics and control are Euler's equations.

$$\mathbf{I}\dot{\vec{\omega}} = -\dot{\vec{h}}_{acs} - \vec{\omega} \times \left(\mathbf{I}\,\vec{\omega} + \vec{h}_{\texttt{acs}}\right) + \tau_{err} \tag{2.1}$$

where $\mathbf{I}$ is the mass moment of inertia, $\dot{\vec{\omega}}$ is the angular acceleration of the spacecraft, $\dot{\vec{h}}_{acs}$ is the time derivative of the angular momentum of the Attitude Control System (ACS), and τ_{err} are the disturbance torques. Equation (2.1) will be covered in more detail in the Chapter III but for now we will simply introduce the equations as a means to compare some of the MOI estimation methods. In addition to Euler's equation we will define the angular momentum of the spacecraft $\vec{Q}$ as

$$
\begin{aligned}
Q_x &= I_{xx}\omega_x + I_{xy}\omega_y + I_{xz}\omega_z \\
Q_y &= I_{xy}\omega_x + I_{yy}\omega_y + I_{xz}\omega_z \\
Q_z &= I_{xz}\omega_x + I_{xy}\omega_y + I_{zz}\omega_z
\end{aligned}
\tag{2.2}
$$

where Q_x, Q_y, and Q_z are the angular momentum of the spacecraft in the $X-$, $Y-$, and $Z-$axis, respectively. Many MOI estimation methods rely on variations of Eqs. (2.1) and (2.2) to estimate the MOI and POI [20; 16]. It is important to note that the estimation of $\vec{Q}$ require data from the ACS and the estimates of ω require data from the inertial measurement unit (IMU). Since the MOI and POI estimates require data from two different sensors, if either sensors has a time-delay in reporting the data then the MOI estimation will be comparing data from different time-steps. This difference in the reporting times can result in an error in the MOI estimate and in this dissertation that error will be referred to as the error associated with time delays.

$$
\dot{\omega} \neq 0. \tag{2.3}
$$

If we assume the spacecraft starts at zero angular momentum we can define the instantaneous MOI estimation as the ratio of the two components

$$
I = \frac{h_{rw}}{\omega_{sc}} \tag{2.4}
$$

where I is the MOI estimate about the rotation axis, h_{rw} is the angular momentum estimate calculated from the RW angular velocity measurements and ω_{sc} is the angular velocity measurements from the IMU. Table 2.1 shows the four possible outcomes that would result from a time difference in the data received from the IMU and the

11

RW angular velocity measurements.

Table 2.1. Results of Time Delays on MOI Estimation

	IMU Leads RW Data	IMU Lags RW Data
Angular Acceleration	MOI Underestimation	MOI Overestimation
Angular Deceleration	MOI Overestimation	MOI Underestimation

Although not explicitly identified in previous orbital MOI estimation methodologies, this can be mitigated on-orbit by implementing long maneuvers with mostly constant angular velocity. With rotation and experiment duration limitations for terrestrial-based satellite attitude simulators the error associated with time delays must be mitigated through alternative means. As a result, we will consider a method's ability to correct for time delays when analyzing an MOI estimation method.

Additionally, the disturbance torques acting on the satellite attitude simulator will integrate and introduce errors in the angular momentum estimate

$$I = \frac{-h_{rw}}{\omega_{sc}} + \frac{\int \tau_{err}}{\omega_{sc}}. \tag{2.5}$$

If we express the disturbance torques as a Taylor series expansion about a neutral position, in our case we define the neutral position as SimSat $Z-$axis being aligned with the negative gravity vector, we can approximate the disturbance torque as

$$\tau_{err} \approx \tau_0 + \tau_1 \delta\theta + \frac{\tau_2 \delta\theta^2}{2!} + \text{H.O.T.} \tag{2.6}$$

where θ is the angle between SimSat's $Z-$axis and the negative gravity vector. We can then approximate the MOI estimate as

$$I = \frac{-h_{rw}}{\omega_{sc}} + \frac{\int \tau_0}{\omega_{sc}} + \frac{\int \tau_1 \theta}{\omega_{sc}} + \frac{\tau_2 \delta\theta^2}{2!\omega_{sc}} + \frac{\int \text{H.O.T.}}{\omega_{sc}} \tag{2.7}$$

In this form it is apparent that non-zero disturbance torques may introduce errors to

the MOI estimate. As a result, we will assume that the disturbance torques on SimSat can be approximated as a zero-order torque plus a first-order torque and the MOI estimation method must have a means to correct for these two components of torque. We will then experimentally validate that second-order torques and the higher-order terms (H.O.T.) are trivial for the small maneuver that will be implemented.

2.2 SimSat II

The Air Force Institute of Technology (AFIT) SimSat was developed in 1999 by Colebank *et al.* [4] The original design was a dumbbell configuration allowing for full rotation about two axes and partial rotation about the third axis. Additionally, the original SimSat used pressurized air in a thruster simulator to dump the built-up angular momentum of the spacecraft. Two disadvantages of the cold-gas thruster system were that the thrusting would induce imbalances in the spacecraft that hindered the reproducibility of the experiments and the amount of air required meant limiting experiment duration to approximately 15 minutes. This first iteration of SimSat also experienced large gravitational disturbance torques due to a structural sag when rotating about the $X-$axis. The platform was reconfigured in 2008 by Roach *et al.* [30] from a dumbbell to a tabletop configuration. In order to reduce disturbance torques associated with thrusting and increase the length of the experiments, the air thrusters were replaced by three fan couples powered a pair of 5.5 Ah, 38 volt batteries allowing for continuous operation up to two hours.

2.3 Survey of MOI Estimation Techniques

The first paper presented in this dissertation (Chapter III) consists of a novel method of estimating the MOI of a terrestrial-based satellite attitude simulator. In this section, we will discuss previously developed MOI estimation methods and briefly

explain how the research presented in Chapter III differs from previous methods.

2.3.1 Direct Measurement.

When referring to direct measurement, we mean a methodology that does not rely on the onboard attitude control system, rather, it is done by external means. Such methods would include using a torsional [39] or bifilar pendulum [15] to estimate the MOI. The benefit to this methodology is that instead of a direct comparison to Euler's equations when using an on-board ACS, the equations of motion of pendulum motion are evaluated to estimate the resistance to angular acceleration. Instead of attempting to compare noisy sensor data instantaneously when using on-board ACS data, the pendulum oscillation frequency is estimated, which can be globally smoothed for highly precise estimations. Although these direct methodologies are highly accurate, there still exists a very strong desire to obtain this degree of precision from in-flight maneuvers. As a result, we will focus on evaluating in-flight estimation methodologies.

Before leaving this discussion on direct measurements, it is also important to identify a potential methodology for POI estimation. Wiener and Boynton [39] estimated the POI of an object by implementing a "Moment of Inertia Method." The method relies on the fact that plotted magnitudes of the mass characteristics in Cartesian space will result in an ellipsoid. Wiener and Boynton estimate the MOI about three test axis in a plane. From these three measurements, the MOI ellipse that is a cross section of the MOI ellipsoid can be estimated. Repeating this process about all three principal planes will result in the complete characterization of the ellipsoid. In Chapter III, we will implement a similar methodology, only we will be over-determining the system of equations and solving for the entire ellipsoid simultaneously. Further improvements include using a static optimization approach to account for differences in precision that may result from different maneuvers being dependent on multiple

RW.

2.3.2 In-Flight and Simulated MOI Estimation.

Due to the change in mass over the course of the satellite's life from the expenditure of propellant for momentum dumping and thrusting for station keeping, the satellite MOI is often re-estimated on-orbit. It is important to note that most of the on-orbit estimation processes rely on the assumption that there are no disturbance torques. This disturbance torque assumption will be shown invalid for terrestrial-based satellite attitude simulators in Chapter III. The following are examples of on-orbit MOI estimation.

Tanygin and Williams [35] not only used the conservation of angular momentum to estimate the MOI but they included conservation of energy into their analyses. By adding an additional constraint

$$\frac{dE}{dt} = \frac{d(\frac{1}{2}I\omega^2)}{dt} = 0 \tag{2.8}$$

they were able to better reject sensor noise and get a more precise estimation of the mass properties. By estimating the MOI during coasting maneuvers, they conserved not only momentum but also energy. By estimating both the energy and angular momentum, they were able to better reject noisy measurements and increase the precision of their estimate. The methodology also includes a rigid body assumption and a zero disturbance torque assumption.

Bordany *et al.* [2] developed an Extended Kalman Filter (EKF) to estimate the mass properties in real time as well as the thruster characteristics of the UoSat-12. In order to estimate these properties, the researchers assumed that the satellite was a rigid body experiencing no disturbance torque and had zero errors associated with time delays. Admittedly, the time delay assumption could be accounted for in using

Bordany's methodology which would require that all time delays be very well under-stood, a condition which is not easily satisfied, as discussed later in Subsection 2.3.3.

Wertz and Lee [20] estimated the MOI and POI of the Cassini spacecraft. During the estimation process, Euler's equations were greatly simplified by implementing pure rotations about a single axis. Wertz and Lee implemented the assumption that with a pure rotation about a body axis they can remove all inertial tensors not pertaining to the test axis allowing for easier estimation of the POI about the test axis. The assumption reduces Eq. (2.2) to

$$
\begin{aligned}
Q_x &\approx \mathtt{I}_{xx}\omega_x \\
Q_y &\approx \mathtt{I}_{xy}\omega_x \\
Q_z &\approx \mathtt{I}_{xz}\omega_x
\end{aligned}
\tag{2.9}
$$

Once the assumptions in Eq. (2.9) were implemented, a least-squares estimation of the MOI and POI were calculated using the RW angular momentum data and the spacecraft angular velocity readings. Although the assumption shown in Eq. (2.9) may appear valid on the surface, due to the presence of sensor noise and other unmodeled variables we cannot guarantee a pure rotation about the test axis which can introduce errors in the estimates of $\mathtt{I}_{xx}$, $\mathtt{I}_{xy}$, and $\mathtt{I}_{xz}$. As a result, the assumption that we can experimentally implement a pure rotation about the test axis on SimSat will be scrutinized in Sec. 3.3 and subsequently the assumption will be deemed is invalid for SimSat.

Research conducted by Ferguson [7] concluded in the design and implementation of an EKF to estimate the MOI matrix similar to Bordany, with an emphasis on IMU biases as opposed to thruster parameters. Similar to Bordany [2], the EKF designed by Ferguson required a rigid body assumption with zero disturbance torques and well

16

characterized time-delays.

Kim *et al.* [16] proposed an MOI estimation technique referred in the paper as a modified law of conservation of angular momentum and tested on STSAT-3. The assumption is that the angular momentum as a result of the POI is negligible when compared to the angular momentum due to the MOI. The assumptions implemented reduce Eq. (2.2) to

$$
\begin{aligned}
Q_x &\approx \quad \mathtt{I}_{xx}\omega_x \\
Q_y &\approx \quad \mathtt{I}_{yy}\omega_y \\
Q_z &\approx \quad \mathtt{I}_{zz}\omega_z.
\end{aligned}
\tag{2.10}
$$

The assumption implemented by Kim *et al.* has the possibility of introducing additional errors similar to Wertz and Lee [20] but for different reasons. Wertz discarded components of the angular momentum due to the assumption that a pure rotation about a body axis can be implemented while discarding the angular momentum associated with the non-test axes, this assumption will be analyzed further in Chapter III. Kim implemented a complex rotation and estimated the angular momentum about all three axes but implemented the approximation that the angular momentum of the platform was due to the MOI while discarding the angular momentum due to the POI. If the POI are sufficiently small then Kim's assumption is valid; however, as the POI for SimSat are unknown this method was also rejected.

Due to the micro-torque environment of space, all of the on-orbit estimation methods were able to assume that the disturbance torques were zero. This allows for large, long maneuvers without having to correct for disturbance torques. As we will show in this research that is not always the case for satellite attitude simulators. The next section discusses terrestrial-based mass characterization estimation.

2.3.3   Terrestrial-Based Satellite Attitude Simulators.

Terrestrial-based satellite attitude simulators are geometrically limited to rotate about the center of an air-bearing, not necessarily the center of mass. As a result, there are potentially large disturbance toques that can be generated as a result of any distance between the center of gravitational force and the center of rotation. Additionally, as the forces acting on the satellite simulator rotate with respect to the spacecraft as it slews, it is possible that the forces induce an imbalance that would result in additional torques. In order to estimate the MOI, these disturbance torques need to be accounted for. It is with an interest in the correction of these disturbance torques that we will analyze the previous MOI estimation methods. The first terrestrial-based MOI estimation method we will discuss was developed on SimSat by Dabrowski [6].

Dabrowski sought to identify a deviation in the MOI due to the presence of parasitic satellites. As a result, he was more concerned with the precision of the MOI estimation than the accuracy. In his methodology, he implemented both a positive step maneuver and a negative step maneuver about a desired test axis. The MOI was estimated from the angular velocity measurements from each step maneuver, and the two step maneuver results were averaged. By averaging the results from both maneuvers, Dabrowski was able to correct for a constant disturbance torque but his methodology is unable to correct for disturbance torques that vary as a function of the spacecraft's orientation, which will be shown to be a principal source.

During his analysis, Dabrowski analyzed three step maneuvers of various sizes in an attempt to identify the precision available for in-flight MOI estimation. One of the resulting conclusions from comparing three maneuvers was that Dabrowski was able to identify that even the simple act of varying the size of the step maneuver could greatly increase the obtainable precision. Although Dabrowski concluded that

the precision of his MOI estimation methodology is dependent on the maneuvers implemented, he stopped short of developing a maneuver specifically for the purpose of further increasing the precision of the MOI estimation. Following Dabrowski's research, Dabrowski's method was implemented by Geitgey [11]. He implemented the same step maneuvers in an attempt to identify remaining on-board fuel. Afterwards, the method was also attempted by Hines [13]. An additional consideration is that Dabrowski's method had no way of correcting for errors in the estimation as a result of time delays as discussed earlier in this chapter.

Schwartz and Hall [31] experimentally compared four methods, the torque method and the momentum integral method evaluated with three different smoothing methodologies, for MOI characterization and introduced a novel method for the correction of errors associated with time delays. Their methodology was applied to both simulated results with 10% sensor noise as well as experimental results from an air-bearing satellite attitude simulator. The simulation results were compared against truth, and the experimental results were compared against an a-priori MOI estimation from a summation of parts from the CAD design. They applied a step maneuver about the $Z-$axis and compared the various results against truth for the simulations and against an a-priori estimate for the experimental results. In addition to directly implementing and comparing the four MOI estimation algorithms, they implemented a methodology for the correction of errors associated with time delays. During simulation with truth data, they analyzed the sensitivity to time delays and noticed that certain MOI and POI components were under-represented by the MOI estimation algorithms for both time advances, as well as time delays. This resulted in peaks at time delay equal to zero. After the experiments were conducted, the MOI and POI estimations were plotted as a function of the time delay. With this in mind, they estimated the MOI and POI for a range of given time delays and chose the time

delay associated with the peak MOI estimated value. Although this method allows for the estimation and correction of errors associated with time delays, the method was only shown for a specific case and no inferences to the global applicability were made. Additionally, the experiment was conducted only about the $Z-$axis and no corrections for disturbance torques were implemented. Although this methodology may be valid for rotations about the $Z-$axis, this method cannot be implemented to estimate the MOI about all three axes and the correction of disturbance torques must also be considered.

Kim and Agrawal [19] conducted a series of experiments on the mass characteristic estimation and the imbalance estimation of satellite attitude simulators. The first component of their research consisted of simultaneously estimating the mass characteristics and imbalance of the satellite simulator using a batch estimation technique. The second component of their research consisted of developing a recursive estimation for the imbalance and will be discussed in more detail in Sec. 2.4.3. The batch estimation method for estimating the MOI and the imbalance, although successful, was based on the assumption that the spacecraft was a rigid body and assumed that there were no errors associated with time delays.

Norman and Peck [28] took a step towards the methods that had been implemented on-orbit by designing an EKF to simultaneously estimate both the MOI and RW misalignment. Similar to the previously implemented on-orbit EKF, Norman and Peck implemented the assumptions that the platform was a rigid, there were zero disturbance torque, and that there were no errors associated with time delays.

In this section we discussed existing methods to estimate the MOI and POI of terrestrial-based satellite attitude simulators with an emphasis on the assumptions that each researcher implemented. In the next subsection, we will briefly describe the proposed research effort and how it differs from the previous methods and the

previously implemented assumptions.

2.3.4   Proposed Mass Moment of Inertia Estimation.

From Subsections 2.3.2 through 2.3.3 there were three recurring assumptions. The first is that the satellite is assumed rigid. This assumption leads into the second assumption that the disturbance torques are assumed to be zero or strictly a result of the imbalance as is the case for Kim and Agrawal [19]. Although these two assumptions may be valid for on-orbit satellites, these assumptions should be verified for terrestrial-based satellite attitude simulators. As gravitational forces are applied to the mass of the satellite simulator, torques are induced. Although the torque about the center of rotation may be counteracted by an equal and opposite disturbance torque due to a second mass attached in the opposite side, the torques themselves induce stress on the structure of the satellite simulator. This stress and corresponding strain cannot be as easily corrected as a simple static imbalance. As a result, higher order disturbance torques need to be analyzed to ensure accuracy of MOI estimation. The third assumption corresponding to the previous research is that there are no errors associated with time delays. There is an exception in the work of Schwartz and Hall [31] but the methodology that they implemented to identify and correct for time delays was subjective and possibly spacecraft and maneuver dependent.

The research conducted in Chapter III focuses on an increase in precision and the correction of errors associated with time delays. Additionally, Chapter III addresses the rigid body assumption and designs and implements a maneuver that is capable of identifying a failure in the rigid body assumption. After the rigid body assumption is deemed invalid, we design and implement a methodology for correcting for the first-order disturbance torques associated with structural deflection allowing for inferences not only into the precision of the MOI estimation methodology, but also allowing us

21

to estimate the accuracy of the MOI estimation.

2.4 Survey of Disturbance Torque Reduction in Satellite Attitude Simulators

As stated in Subsection 2.3, Chapter III focuses on the applicability of assumptions and the accounting for disturbance torques during an MOI estimation procedure. This section focuses primarily on looking at work completed by other researchers to reduce the disturbance torques encountered by satellite attitude dynamics simulators. In doing so we will focus on the assumptions that were required to implement the disturbance torque reduction methodology and analyze the validity of the assumptions on SimSat. After the assumptions were deemed invalid we developed a novel methodology for the reduction of gravitational disturbance torques. This section addresses the previously developed methods for the reduction of gravitational disturbance torques as well as the assumptions that were implemented during the development of the gravitational disturbance torque reduction process. First, we will discuss the characterization of disturbance torques.

2.4.1 Disturbance Torque Characterization.

As referenced by Schwartz [32] in the historical review of air-bearings, Smith [34] derived the equations of various disturbance torques experience by satellite attitude simulators. During Smith's derivation of the disturbance torque associated with structural deflection, he assumed that the spacecraft was perfectly rigid in the $X-Y$ plane and only derived the disturbance torques associated with a deflection in the $Z-$axis. As a result, the equations for the disturbance torques due to structural deflection were underrepresented for small rotations. Subsequently, research concentrating on the disturbance torque reduction has focused on the avoidance of structural deflec-

tions instead of the identification and correction of the disturbance torques due to structural deflections.

2.4.2 Avoidance of Structural Deflection.

A good example of the emphasis on the avoidance of structural deflections is shown by Mork and Wheeler [27] who analyzed possible solutions to simulate on-orbit structural oscillations without having to induce terrestrial-based gravitational disturbance torques due to structural deflections [27]. Mork and Wheeler theorized that the reactive torques due to the structural oscillations can be emulated experimentally with an applied torque. A similar method was implemented by Liu *et al.* [24] in which the disturbance torques associated with the structural deflections were estimated and experimentally implemented to the air-bearing satellite attitude simulator by means of an applied torque. This allowed for experimental results for controls of flexible spacecraft without needing to attach flexible appendages that are intrinsically prone to gravitational disturbance torques. Although these methods are capable of simulating structural deflections without imparting structural deflections, they maintain the assumption that the spacecraft is rigid and do not address what occurs when structural deflections occur. Once one makes the assumption that the spacecraft is rigid, they typically focus on balancing the satellite attitude simulator. Balancing can often be tedious and time consuming, which typically leads to an effort focused on automating the balancing process. The following section discusses how various researchers have addressed the problem of automatic balancing.

2.4.3 Automatic Balancing of Satellite Attitude Simulators.

Hatcher and R. Young [12] developed and analyzed an automatic balancing system for air bearing satellite attitude simulators. The research was primarily focused on

the design and validation of an analog circuit to command a step-motor to move the masses into the desired position using. The system split the signal being sent to the torque inducing actuators being used by the ACS which resulted in a mass position change along with a control torque. Although the system showed much promise in the $X-Y$ plane, it did not include balancing in the $Z-$axis.

A more modern approach to automatic mass balancing comes from J. Young in the form of the Dynamic Identification and Adjustment of the Mass Center [42]. In his research Young uses a coasting maneuver and estimates the disturbance torques to calculate an estimate of the imbalance. This method implements balancing process and an iterative approach to converge to the correct balance.

Prado [29] implemented a balancing technique very similar to Young only Prado did not have an enabled control torque source and used the weights themselves as the control torque. Additionally, Prado compared his method with the method developed by Young and was able to duplicate the level of precision obtained by Young while also concluding that Prado's method was able to obtain approximately 50% better balance in the $X-Y$ plane. Up to this point, we have discussed balancing algorithms that are implemented using specific maneuvers and procedures, the following methodologies can be implemented in real-time without the need for specific pre-flight maneuvers.

This differs from more recent research efforts to estimate and correct for the imbalance real-time with an EKFs. As suggested earlier in Subsection 2.3.3 the second component of Kims [19] research consisted of designing and experimentally implementing an EKF for real-time estimation of the imbalance of the spacecraft and using the results from the EKF to command actuators to drive the imbalance to zero. Kim and Agrawal [18] continued their research by comparing two different automatic balancing methods, batch estimation and real-time estimation. The conclusion was that they were able to get comparable results with the EKF even through concerns about

closed-loop stability of active balancing process. The work by Kim and Agrawal has been continued by other researchers. Li and Gao, [23] successfully implemented the batch balancing algorithm on the air-bearing satellite attitude simulator at Shenyang University of Technology. Additionally, Chesi *et al.*, [3] advanced the EKF developed by Kim and Agrawal by showing that Lyapunov Stability existed in the closed-loop controller that consisted of using the estimated imbalance to command actuators to correct for the estimated imbalance and drive the imbalance to zero.

2.5 Recent Advancements in Alternatives to 3-DOF Satellite Attitude Simulators

In addition to 3-DOF satellite attitude simulators there has been an increased amount of interest in 6-DOF satellite attitude simulators. The translational component allows for researchers to not only analyze attitude dynamics and control, but also translational controls required for orbital rendezvous [10; 36]. Although the additional degrees of freedom are necessary for orbital rendezvous, the added complexity is not necessary for the development and validation of satellite attitude control algorithms.

In addition to 6-degree-of-freedom satellite attitude simulators, a second alternative to air-bearing satellite attitude simulators is the emerging CubeSat. The CubeSat is an orbital platform that allows for the analysis of satellite attitude control algorithms in the environment that they were designed to operate in and is therefore much more desirable as a research platform as it is not prone to the disturbances experienced by satellite attitude simulators. One drawback to CubeSats is the size constraint specifically when attempting to research more complex ACS such as a CMG array. Not only is there a volumetric geometric constraint, but this constraint is exacerbated by the increased complexity of the equations of motion as some of the assumptions that hold true for larger CMG arrays will not necessarily hold true for

miniaturized CMG arrays [21]. As a result, although there are currently competing research platforms the 3-DOF remains and will remain a crucial component to the validation and verification of satellite attitude control algorithms.

After analyzing the current MOI and POI estimation methodology, we conclude that all of the methods available for implementation on terrestrial-based satellite simulators implement assumptions that may not be valid for SimSat. Without validating and verifying these assumptions on SimSat we cannot guarantee that we will obtain the precision and accuracy desired to meet future research objectives such as the analysis of feed-forward controls. In the next chapter, we will analyze the previous assumptions on SimSat, and ultimately develop a novel method to estimate the MOI matrix of a satellite attitude simulator while accounting for time delays and gravitational disturbance torques.

III. Mass Moment of Inertia Estimation for Terrestrial-Based Satellite Simulators

The purpose of this research effort is to improve upon current maneuver-based MOI estimation methodologies in an attempt to achieve the higher precision previously reserved for direct measurement techniques. This paper will discuss the advantages and disadvantages of existing MOI estimate maneuvers before presenting a different approach that is dependent on the three key components that are the POI estimation methodology, the selection of the estimation maneuver, and the characterization and correction of the disturbance torques. Three components were chosen to specifically increase both the precision and accuracy of maneuver-based MOI matrix estimation. The POI methodology was chosen to minimize the number of assumptions, such as the pure rotation about the test axis [20], while increasing the precision of the POI estimation method. A maneuver was constructed using lessons learned from other researchers, while making inferences based on the capabilities and limitations pertaining to but not specific to the AFIT air-bearing satellite simulator known as SimSat. Additionally, because SimSat utilizes an air bearing, similar to air-bearing platforms characterized by other researchers, considerations were taken to approximate and subsequently characterize the disturbance torques which could lead to additional errors in the MOI approximation. Although it is not uncommon for terrestrial-based satellite simulators to account for zero-order disturbance torques during MOI estimation [6], this research will expand this process to account for both zero- and first-order disturbances to ensure an accurate MOI approximation. The entire process was experimentally evaluated on AFIT's second generation satellite simulator SimSat and the experimental results are discussed.

3.1 Introduction

A spacecraft's moment of inertia (MOI) is a measure of its resistance to torque. The MOI matrix is symmetric positive definite matrix composed of six components, the three major components along the diagonal are known as the moments of inertia, and the three off-diagonal components are referred to as the products of inertia. The effects of these components can be seen in Eq. (2.1). Knowledge of all six values is critical to performance associated with attitude control and estimation while reorienting a satellite. Whether it is tuning a closed-loop controller or calculating open-loop optimal controls, errors in MOI approximations will result in decreased performance. In order to accurately estimate the MOI of spacecraft, high fidelity finite element models are commonly utilized and often the MOI is measured directly before the satellite is launched. While this process allows for a high fidelity estimation early in the spacecraft's lifespan, spacecraft have a decreasing MOI as on-board propellants are expended for station-keeping maneuvers or angular momentum dumping. As a result, even though the MOI for the spacecraft might have been well known before launch, it is often advisable to re-estimate the MOI using a maneuver-based MOI estimation method. However, accurate MOI approximation isn't only necessary for actual satellites; satellite attitude simulators, such as the Air Force Institute of Technology's SimSat, also need a high-fidelity MOI approximation when conducting controls-based research.

Satellite attitude simulators are often used to test controllers that may be too aggressive for immediate on-orbit implementation [41]. It is desirable for satellite attitude simulators to behave as much like a spacecraft as possible; which results in the desire to know the MOI to within tolerances desired on-orbit. Obtaining this level of accuracy however, is difficult as disturbance torques present in a lab environment, such as torques due to an imbalance or structural flexing, result in a requirement for

smaller, shorter maneuvers than those obtainable on-orbit [6]. Although the MOI of a satellite simulator could also be measured directly through the use of a torsional pendulum, similar to a real satellite is measured before launch, this is not always a practical estimation method as the tests can be time consuming and cost-prohibitive. Additionally due to ease of access, configuration changes on satellite simulators are made frequently and quickly. These configuration changes can typically be made in a matter of days and sometimes hours. Rapid configuration changes combined with the impracticality of physical measurements make MOI approximation maneuvers highly desirable as a maneuver can be re-executed resulting in a new MOI approximation within an hour or two. Additionally, unlike direct measurements, a maneuver-based MOI estimation methodology can be easily implemented on-orbit allowing for an increased MOI precision. This is beneficial not only to performance obtained when correctly tuning controller gains, but may also allow for increased precision towards identification of remaining onboard fuel [11] or maybe even allow for future identification of parasitic satellites [6].

Although maneuver-based MOI estimate methods are desired for increased on-orbit MOI estimation capability, the degree of precision with the existing maneuver-based MOI estimation methodologies leaves much to be desired, and without consideration of first-order disturbance torques the accuracy cannot be verified when attempting to implement on satellite simulators. Current MOI estimation methods have been shown to be precise, with the standard deviations of multiple experiments of approximately 2.5% of the mean value. Direct measurement tools such as torsional pendulums can often achieve accuracies of within 0.35% of the actual value [39]. The purpose of this research effort is to improve upon current maneuver-based MOI estimation methodologies in an attempt to achieve the higher precision previously reserved for direct measurement techniques.

29

3.2 Background

Due to the importance and need for an accurately estimated MOI, various MOI estimation methods have been implemented by various researchers over the years. Most of the existing estimation techniques can be broken into two categories: direct measurement and maneuver-based. Furthermore, maneuver-based estimation techniques can be further broken down into real-time and post-process estimation. This section will briefly cover the advantages and disadvantages of the previously developed methods before explaining why a post-processing maneuver-based estimation method is the preferred choice and the one implemented in this research. However, in order to accurately analyze the alternatives, the disturbance torques that will affect the processes need to be discussed as they contribute heavily to the decision making process.

3.2.1 Disturbance Torques and Additional Error Sources.

In addition to the usual signal noise associated with measurement based estimation, there are additional error sources that contaminate the measurement data of satellite attitude simulators. The dominant disturbance torques can be considered a function of the satellite simulator's orientation, similar to how the torque on a pendulum is dependent on the current position of the pendulum. If we define a neutral position such that the satellite simulator's $Z-$axis is aligned with the gravity vector, then θ can be defined as the rotation about the $X - Y$ plane resulting in a deviation from this neutral state. The disturbance torques can then be characterized with a Taylor Series expansion about the neutral position as a function of $\delta\theta$. The order of $\delta\theta$ that the torque produces will be considered the order of the disturbance torque.

The most common error source is due to the gravitational disturbance torque associated with an imbalance of the satellite attitude simulator. Unlike rotating about

the center of mass like real satellites do on orbit, satellite simulators on air bearings are geometrically forced to rotate about the center of the air-bearing. As a result, any misalignment between the center of mass and the center of rotation when crossed with the gravity vector will generate a disturbance torque. This results in imbalance in the $X-$ and $Y-$axes producing zero-order torques as discussed later in Sec. 3.4, while imbalances in the $Z-$axis results in a first-order torque and will be discussed later in Sec. 3.5. Although great care is taken to balance satellite simulators before every experiment, errors in the balance estimation will inevitably introduce additional errors into the measurement data. In addition to the first-order torque resulting from an imbalance in the $Z-$axis, a second first-order torque associated with structural flexing is presumed to be present, and will also be discussed in Sec. 3.5. As a result, the reaction wheel (RW) angular momentum data will need to be corrected for estimated disturbance torques associated with both an imbalance as well as structural flexing. Previous researchers accomplished zero-order torque correction through symmetry by performing two similar maneuvers [6], one maneuver in both the positive and negative directions and then averaging the results of the two. This method can be successful in removing zero-order disturbance torques; however, this method cannot correct for the first-order torques which are assumed to be present. As a result, a successful MOI estimation methodology will need to allow for the identification of disturbance torques as well as allow for the correction of experimental data to remove the subsequent errors.

In addition to zero- and first-order disturbance torques, a second error source that should be considered is the error associated with the time delays of the data from the sensors. Maneuver-based MOI estimation processes depend heavily on collecting data from multiple sources simultaneously. Due to the limited bandwidth of on-board interfaces, typical data recorders cannot communicate with all of the on-board

components at all time-steps. This fact is exacerbated by the on-board filters meant to reduce the effective noise coming off of the sensors. As a result, the data from the IMU will lag the RW data even though in reality the two actions occur simultaneously. Therefore, the method must have the capability to identify and if present correct for errors associated with delays between data collection from multiple sensors. Now that we have discussed disturbance torques that satellite simulators are vulnerable to, we now analyze potential MOI estimation methods.

3.2.2 Direct Measurement.

When referring to direct measurement, we mean a methodology that does not rely on the onboard attitude control system. Such methods would include using a torsional pendulum to estimate the MOI [39], or suspending the satellite simulator on a bifilar pendulum [15]. These methods for MOI estimation have been shown to be highly accurate, but were not selected for two major reasons. The first is that satellite simulators, such as SimSat are prohibitively large (estimated mass of > 75 kg) it would be possible for direct measurement the larger mass would require the acquisition of larger test platforms and was ultimately cost and time prohibitive. The second reason that a direct estimation method was not attempted is that the research could not then be expanded for implementation for on-orbit satellites. As a result, it was concluded that the most benefit would be gained by developing a maneuver-based MOI estimation method capable of higher precision and accuracy.

3.2.3 Maneuver-Based Estimation.

Maneuver-based MOI and POI estimation methods rely on attitude kinematics and the on-board attitude control system. Controlling the attitude of a satellite attitude simulator requires three basic components: a means of measuring the orien-

tation, a means of calculating the desired torque, and means of applying the desired torque. On SimSat these are an IMU which provides angular rates to a dSPACE MicroAutoBox™ which integrates the angular rates and calculates the satellite simulator's orientation. The dSPACE MicroAutoBox™ then uses a quaternion error calculation to calculate the desired torque and then commands a three RW array in order to provide the desired torque. The current SimSat configuration is shown in Fig. 3.1(a) and the body axes which will be referenced later in the paper is shown in Fig. 3.1(b). As mentioned earlier, maneuver-based estimation methods will use the spin rates of the RWs and the angular velocity of the satellite simulator from the IMU to estimate the MOI of the satellite simulator. Maneuver-based MOI estimation methods can be separated into: real-time and post-processing estimation.

(a) AFIT Satellite Simulator SimSat   (b) Body Axes superimposed on SimSat
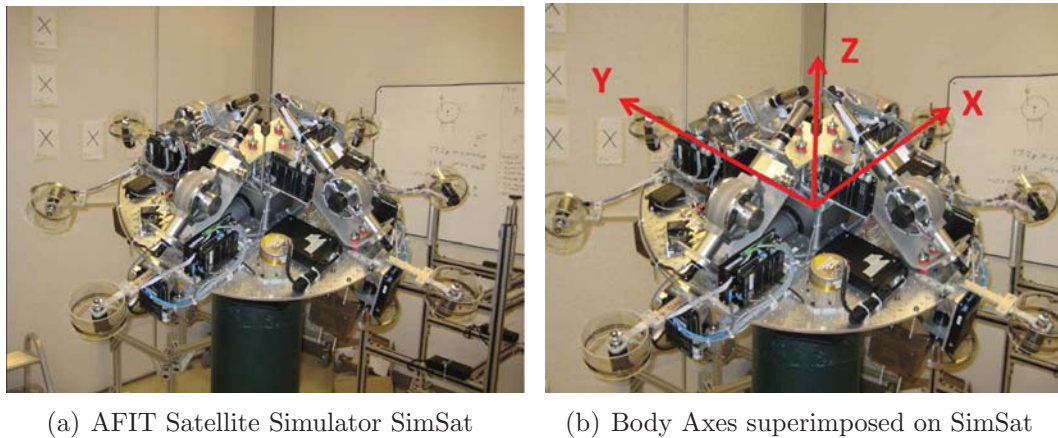
Figure 3.1. AFIT SimSat and the Defined Body Axes

3.2.4   Real-Time MOI Estimation.

As the name suggests, real-time MOI estimation methods are designed to run continuously, and estimate the MOI in real-time. Real-time estimation methodologies typically implement linear estimators to estimate the MOI and POI by using differences between estimated states and measured states to calculate a recursive,

least-squares estimate of the MOI and POI. This has previously been implemented by the Naval Postgraduate School [17]. There are many benefits to real-time estimation methodology including the most obvious that the estimator is always running and that there is no need for dedicated estimation maneuvers. Any maneuver should theoretically allow for eventual convergence of the estimator. Additionally, due to the algorithm being able to run constantly, the method is able to actively correct for any changes in the MOI due to slight mass position changes, such as slight mass movement as a result of re-balancing. Despite the benefits, there are also some disadvantages to this method of MOI estimation. The most critical is that there are two assumptions that must be made in order to implement this estimation methodology. The first is that the satellite attitude simulator is rigid and the second is that there are no errors associated with time delays. Since neither of these assumptions have been verified for SimSat, these estimation methods will be rejected in favor of a post-processing MOI estimation method.

3.2.5 Post-Processing MOI Estimation.

The second main category of maneuver-based estimation, and the one chosen for this research, is to estimate the MOI by post-processing the maneuver data. Not only has this methodology shown benefit on-orbit[20] but post-processing should allow for the removal of disturbance torques that terrestrial-based satellite attitude simulators are prone to.

The methodology that was chosen is a continuation of the work performed by Dabrowski [6] when attempting to estimate the MOI for the identification of parasitic satellites. The method was strongly based on the work performed by Wertz and Lee on the Cassini spacecraft; however, the MOI matrix was assumed diagonal and the POI estimation process was neither analyzed nor implemented. Additionally,

during Dabrowski's research effort three estimation maneuvers were performed and evaluated against each other. Dabrowski's research suggested that the precision of the MOI estimation is highly dependent on the maneuver being implemented, but stopped short of designing a maneuver specifically for the purpose of estimating the MOI. This presented research effort picks up where Dabrowski left off where MOI estimation maneuvers are designed to correct for some of the shortcomings previously identified while accounting for additional platform limitations. In addition to overhauling the maneuver, the POI are no longer assumed to be zero and the single axis MOI estimation methodology needed expanding to estimate the POI as well as the MOI. As a result, the methodology and assumptions implemented by Wertz and Lee for POI estimation is covered in detail in the subsequent section before being passed over in favor of the "MOI" method for POI estimation in which a collection of MOI estimates are used to simultaneously solve for the entire MOI ellipsoid [39]. This will be followed by the development of a new MOI estimation maneuver and an analysis of the zero- and first-order disturbance torques. All of the components will then be combined experimentally to characterize the MOI matrix of SimSat.

3.3   Product of Inertia Estimation Methodology

Before settling on a methodology for POI estimation, the previous work performed by Wertz and Lee is evaluated [20]. The methodology implemented on the Cassini spacecraft was depended on two assumptions. The first of which is that the disturbance torques are negligible. Although this is not a valid assumption for terrestrial-based satellite attitude simulators, post-processing can be implemented in order to correct for errors in the angular momentum build up in the RWs as a result of the disturbance torques. The second assumption is that pure rotations about the principal axes can be implemented, and this assumption will be analyzed in detail in

this section.

The kinematic equations implemented to estimate the MOI and POI were based on the conservation of angular momentum. First, Wertz and Lee [20] defined the angular momentum of the spacecraft $\vec{\mathbf{Q}}$ as

$$\vec{\mathbf{Q}} = \mathbf{I}\vec{w} \tag{3.1}$$

where $\vec{\mathbf{Q}}$ is an array containing the angular momentum of the spacecraft, $\vec{w}$ is the angular velocity of the spacecraft, and $\mathbf{I}$ is the MOI matrix and is defined as

$$I = \begin{bmatrix} I_{xx} & I_{xy} & I_{xz} \\ I_{xy} & I_{yy} & I_{yz} \\ I_{xz} & I_{yz} & I_{zz} \end{bmatrix}. \tag{3.2}$$

By multiplying out the vector product we obtain the following three scalar equations

$$\begin{aligned} Q_x &= I_{xx}\omega_x + I_{xy}\omega_y + I_{xz}\omega_z \\ Q_y &= I_{xy}\omega_x + I_{yy}\omega_y + I_{xz}\omega_z \\ Q_z &= I_{xz}\omega_x + I_{xy}\omega_y + I_{zz}\omega_z. \end{aligned} \tag{3.3}$$

Wertz and Lee's assumption was then made that a rotation only about the $X-$axis $(\omega_y = \omega_z = 0)$ would result in the following

$$\begin{aligned} Q_x &\approx I_{xx}\omega_x \\ Q_y &\approx I_{xy}\omega_x \\ Q_z &\approx I_{xz}\omega_x \end{aligned} \tag{3.4}$$

36

Wertz and Lee were then used these equations to solve for I_{xy} and I_{xz}. Although this assumption is highly desirable due to the fact that it greatly reduces the complexity of the problem, the validity of the assumptions need to be verified. As a result, the absolute value of the IMU data on SimSat was analyzed and is shown in Fig. 3.2. This figure shows us that the noise for our accelerometer is approximately on the order of 10^{-4} radians per second, while our maneuver is only on the order of 10^{-2} radians per second.
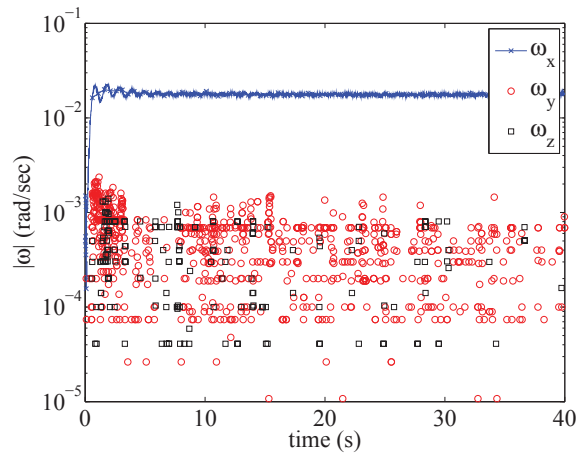
Figure 3.2. Absolute Value of Fiber-Optic Gyroscope Angular Velocity Data versus Time

Figure 3.2 shows the maneuver about ω_x and the subsequent sensor noise in the $Y-$ and $Z-$axes. The data suggests that assuming that the angular velocities in the other two axes are zero might be valid. However, if we consider Eq. (3.4) to be a collection of four assumptions instead of just two, we can better analyze the validity of the assumptions. Considering only the $X-$axis, the following four assumptions can be made

37

$$\omega_x > \omega_y$$

$$\omega_x > \omega_z$$

$$\mathtt{I}_{xx} > \mathtt{I}_{xy} \tag{3.5}$$

$$\mathtt{I}_{xx} > \mathtt{I}_{xz}.$$

As shown in Fig. 3.2, our nearly pure rotation about the $X-$axis will result in the first two equations being valid to approximately two orders of magnitude, and due to the symmetry of SimSat, visible in Fig. 3.1, the POI are estimated to be at least an order of magnitude smaller than the MOI. These four assumptions combine to result in the following assumptions

$$\mathtt{I}_{xx}\omega_x \gg \mathtt{I}_{xy}\omega_y \tag{3.6}$$

$$\mathtt{I}_{xx}\omega_x \gg \mathtt{I}_{xz}\omega_z$$

being valid to approximately three orders of magnitude. Alternatively, if the angular momenta in the $Y-$ and $Z-$axes are considered, the following equations can be concluded

$$\omega_x > \omega_y$$

$$\omega_x > \omega_z$$

$$\mathtt{I}_{xy} < \mathtt{I}_{yy} \tag{3.7}$$

$$\mathtt{I}_{xz} < \mathtt{I}_{zz}.$$

As previously stated, the angular velocity in the $X-$axis is at least two orders of

38

magnitude larger than the angular velocities in the $Y-$ and $Z-$axes, and again the POI are assumed to be at least an order of magnitude smaller than the principal moments of inertia. However, unlike the $X-$axis, these two assumptions are not compounded but instead detract. The ω_y and ω_z components are therefore only estimated to be one order of magnitude smaller than the ω_x components, not three orders of magnitude smaller as was experienced in the $X-$axis. As a result, the four Eqs. (3.7) are combined to conclude

$$
\begin{aligned}
I_{xy}\omega_x &\ggg I_{yy}\omega_y \\
I_{xz}\omega_x &\ggg I_{zz}\omega_z.
\end{aligned}
\tag{3.8}
$$

The assumptions in Eq. (3.8) are applied to Eq. (3.3) resulting in

$$
\begin{aligned}
Q_y &\approx I_{xy}\omega_x + I_{yy}\omega_y \\
Q_z &\approx I_{xz}\omega_x + I_{zz}\omega_z.
\end{aligned}
\tag{3.9}
$$

In order to reduce the risk of introducing errors into the MOI and POI estimation process, we decided not to implement the assumptions implemented by Wertz and Lee. As a result, the products of inertia will not be calculated directly. This experiment will only directly calculate the moments of inertia about the current maneuver axis, but not the products of inertia. The following section will explain in detail the implementation of the "moment of inertia" method for product of inertia estimation.

3.3.1   The "Moment of Inertia" Method.

Instead of trying to directly compute an estimate of the POI, this research will estimate the POI by estimating the MOI ellipsoid. This method is similar to the

39

two-dimensional analysis performed by Wiener and Boynton [39] that estimated the two-dimensional cross-section of the MOI ellipsoid to simultaneously estimate two MOI and the single POI. The two-dimensional method could be repeated about the other two principal planes to estimate the other MOI and the other two POI. Instead of multiple implementations of a two-dimensional method, this research will collect all of the data first and then will simultaneously estimate the entire MOI matrix [39]. First, the equation for the MOI ellipsoid is identified as [37]

$$I_{xx}\alpha^2 + I_{yy}\beta^2 + I_{zz}\gamma^2 + 2I_{xy}\alpha\beta + 2I_{xz}\alpha\gamma + 2I_{yz}\beta\gamma = I_{ta} \tag{3.10}$$

where α, β, and γ are defined by the unit vector in the direction of the test axis. Let $\hat{n}$ be a unit vector in the direction of the test axis, then

$$\hat{n} = \alpha\hat{i} + \beta\hat{j} + \gamma\hat{k} \tag{3.11}$$

and I_{ta} is the MOI about the test axis. As described in Sec. 3.3, each maneuver will result in a single MOI estimation. As a result, a minimum of six independent estimations are needed in order to solve Eq. (3.10). After a series of MOI estimations are made about various axes, the MOI ellipsoid will be estimated, and the MOI matrix can be calculated as described in Eq. (3.2). To ensure that the solution is over-determined, twelve measurements are collected. To reduce measurement dependency, a risk due to the symmetry of ellipsoids, the twelve measurements will be collected in a single hemispherical quadrant as shown in Fig. 3.3.

In order to estimate the MOI about each axis, several runs are performed. The measured MOI about the ith test axis, subsequently referred to as I_{meas_i}, is defined as the mean of the five estimations about the ith test axis. A corrected sample standard deviation σ_{meas_i} is also calculated as
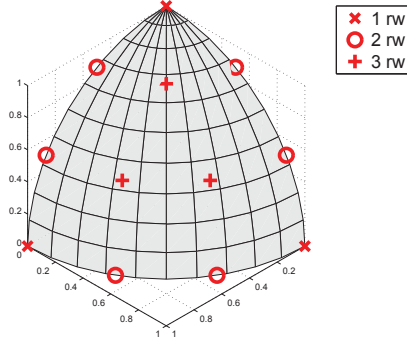
Figure 3.3. Twelve Collection Axes as Represented by Points on a Sphere

$$\bar{\sigma}_{meas_i} = \sqrt{\frac{1}{n-1} \sum_{j=1}^{n} (\bar{I}_{meas_i} - I_{meas_{ij}})^2} \qquad (3.12)$$

where $\bar{I}_{meas_i}$ is calculated from the average of the five measurements

$$\bar{I}_{meas_i} = \frac{1}{n} \sum_{j=1}^{n} I_{meas_{ij}} \qquad (3.13)$$

where n is the total number of estimates about the ith axis and for these experiments will be equal to five.

Once the twelve estimated mean values of $\bar{I}_{meas_i}$ are calculated, one may be tempted to substitute the values of $\bar{I}_{meas_i}$ immediately into a least-squares estimation; however, additional care is taken to consider the decreased precision that could result from estimates that are a result of multiple RW required to work in unison. As a result, each measurement was effectively weighed based on the precision of the collection of measurements σ_{meas_i}. First I_{xx}, I_{yy}, I_{zz}, I_{xy}, I_{xy}, and I_{yz} were initialized with values of 8, 8, 12, 0, 0, and 0 kgm^2 respectively. Then for each of the twelve estimates, the unit vector in each direction $\hat{n}_i$ was defined as

$$\hat{n}_i = \alpha_i \hat{i} + \beta_i \hat{j} + \gamma_i \hat{k}. \qquad (3.14)$$

and α_i, β_i, and γ_i were substituted into the equation

$$I_{calc_i} = I_{xx}\alpha_i^2 + I_{yy}\beta_i^2 + I_{zz}\gamma_i^2 + 2I_{xy}\alpha_i\beta_i + 2I_{xz}\alpha_i\gamma_i + 2I_{yz}\beta_i\gamma_i. \tag{3.15}$$

Once the twelve I_{calc_i} have been calculated, the twelve values of I_{calc_i} are substituted into the standard deviation weighted cost equation

$$J = \sum_{i=1}^{12} \left(\frac{I_{calc_i} - \bar{I}_{meas_i}}{\bar{\sigma}_{meas_i}} \right)^2. \tag{3.16}$$

A static optimization algorithm was then implemented to iterate on I_{xx}, I_{yy}, I_{zz}, I_{xy}, I_{xy}, and I_{yz} while minimizing the cost function J. Though this method should provide a high degree of accuracy for a provided dataset, additional steps are taken to ensure that the dataset itself is highly accurate. The following section will discuss the method for estimating each of the twelve MOI estimates.

3.3.2 Satellite Maneuver for MOI Estimation.

The previous work on MOI estimation on SimSat was conducted by Dabrowski [6]. During the research effort, a series of step maneuvers was implemented in order to estimate the MOI. An example of a maneuver implemented by Dabrowski is shown in Fig. 3.4(a). One of the conclusions of Dabrowski's work was that even slight differences in maneuvers can result in as much as 50% increase in precision of the MOI with the highest level of precision obtained of approximately 2.5%. In order to further increase the precision, a sample maneuver was duplicated and analyzed. The position data from the maneuver is shown in Fig. 3.4(a) and the angular velocity from the IMU is shown in Fig. 3.4(b).

The first observation is that the maneuver is not very efficient, with only about twenty seconds of data being collected from a fifty second maneuver. Although this was of little concern when only needing to characterize three MOI values, when the

(a) Desired Angular Rotation   (b) Angular Position
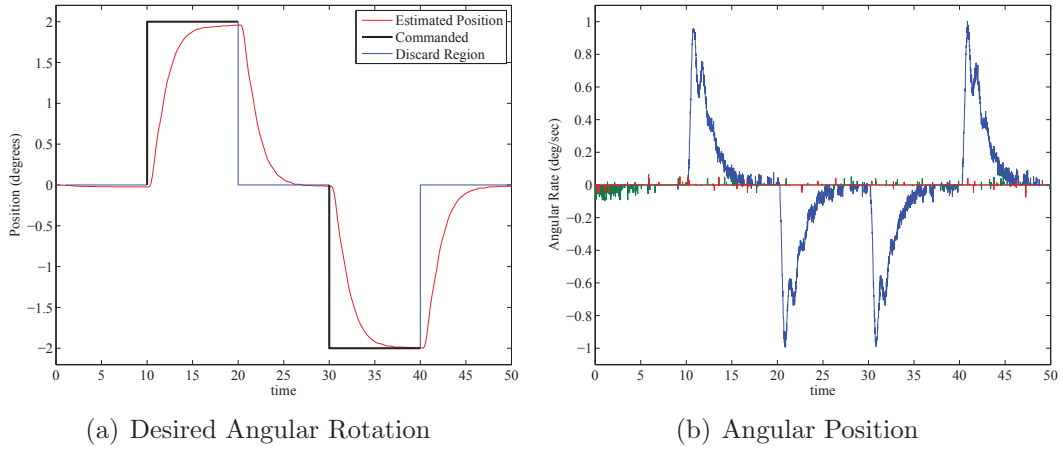
Figure 3.4. Step Maneuver Angular Position and Angular Rates

methodology is expanded to characterize six components time efficiency becomes a concern. Additionally, when considering Fig. 3.4(b) it becomes apparent that there is a significant amount of noise from the IMU. One method that can be implemented, when attempting to reduce the amount of noise in data, is to fit the data with a smooth function. Unfortunately, at around the eleven and thirteen second marks of the first step maneuver there are noticeable anomalies, a result of nonlinearities associated with torque saturation of the RW motors. These anomalies are also present in each of the three remaining maneuvers further suggesting this is not merely an isolated incident. As a result, the function that we are attempting to fit is non-differentiable, and any attempt to fit a smooth function to said non-differentiable function will introducing errors associated with the Gibb's phenomenon [9].

In addition to the shape of the function, the peak magnitude of the function must also be considered. Although we will be removing errors associated with zero- and first-order disturbance torques, there are expected to be still higher-order disturbance torques, so the magnitude of the maneuver is also of significant concern. Meanwhile, if a maneuver is too small there may not be enough information to correctly discern the MOI estimate and we find ourselves in a trade-off. Once again, Dabrowski's research

provides some insight. The step maneuver shown in Fig. 3.4(a) was implemented in three sizes, 0.5°, 1°, and 2° as shown in Fig. 3.4, with the most accurate of the three appearing to be the 2° maneuver. This suggests that the additional information gained by implementing a larger maneuver, up to at least 2°, is more beneficial than the higher-order disturbance torques associated with the larger maneuver were detrimental. Combining all of these pieces of information, a smooth function, of approximately plus or minus 2°, approximately 60 seconds duration, and able to reject errors associated with time delays was deemed desirable. As a result, a maneuver in the following form is suggested.

$$\omega = A \sin\left(2\pi f t\right) \tag{3.17}$$

where A is the amplitude of the sinusoid with units of radians per second to match the units with the angular velocity of the spacecraft and f is the frequency in cycles per second. The maneuver described in Eq. (3.17) was chosen because the measured angular velocity data can be smoothed with a Fourier approximation for better signal noise rejection. Additionally, instead of calculating the MOI directly using instantaneous comparisons of the angular momentum of the RW and the angular velocity of the spacecraft ω_{sc}, the following methodology was implemented to estimate the MOI. First it is assumed that the angular velocity of the spacecraft is in the form

$$\omega_{sc} \approx A_\omega \sin(2\pi f t) + B_\omega \cos(2\pi f t) \tag{3.18}$$

where B_ω is the result of a phase shift and is necessary to account for any time delays between the desired maneuver, a sinusoid with zero phase shift, and the actual maneuver. The amplitude of the oscillation of the spacecraft's angular velocity $A_{w_{sc}}$ can then be calculated as

$$A_{w_{sc}} = (A_\omega^2 + B_\omega^2)^{1/2}. \tag{3.19}$$

The process can then be repeated to calculate the amplitude of the oscillation of the RW angular momentum. First the raw angular momentum data is measured using the RW motor angular velocities provided by a shaft encoder attached to each of the three RW motors. The angular velocities are then multiplied by the corresponding flywheel MOI that were measured prior to installation and each RW angular momentum is multiplied by the corresponding coordinate transformation and then summed to calculate the angular momentum of the RW array in the body frame [25]. Once the angular momentum of the RW array is known, a coordinate transformation is used to isolate the RW angular momentum about the test axis and the remaining RW angular momentum data is discarded. This can be done since a torque couple for an angular momentum perpendicular to the test axis will result in a disturbance torque. The data for h_{rw} about the test axis is then used to calculate the coefficients A_{rw} and B_{rw} that best fit the equation

$$h_{rw} \approx A_{h_{rw}} \sin(2\pi ft) + B_{h_{rw}} \cos(2\pi ft) + C_{h_{rw}}. \tag{3.20}$$

The amplitude of the RW angular momentum $A_{h_{rw}}$ can then be calculated as

$$A_{h_{rw}} = (A_{h_{rw}}^2 + B_{h_{rw}}^2)^{1/2}. \tag{3.21}$$

The estimated MOI of the spacecraft can then be calculated as

$$MOI_{est} = \frac{A_{h_{rw}}}{A_{w_{sc}}}. \tag{3.22}$$

This method was implemented because it has the added benefit that any errors associated with time delays will manifest themselves in the phase information. As a result,

45

the amplitudes of the spacecraft angular velocity $A_{w_{sc}}$ and the amplitude of the RW angular momentum $A_{h_{rw}}$ are left relatively unaffected and therefore additional error is not introduced into the MOI estimate. The next section discusses how A and f are chosen for the experiments.

3.3.3 Maneuver Construction.

The values for the amplitude A and frequency f of the spacecraft maneuver are determined by first considering the following relationship, given an equation for ω

$$\omega = A \sin\left(2\pi f t\right) \tag{3.23}$$

where the time derivative $\dot{\omega}$ is

$$\dot{\omega} = 2\pi f A \cos\left(2\pi f t\right). \tag{3.24}$$

With the non-linearities associated with torque saturation producing the non-differentiable maneuver shown in Fig. 3.4, it is inevitable that torque limitations be considered when designing the new maneuver. The desire to stay within the linearity of a non-saturated torque window results in the inequality constraint

$$|I_{ta}\dot{\omega}| = |I_{ta}2\pi f A \cos\left(2\pi f t\right)| < |\dot{h}_{max_{acs}}| \tag{3.25}$$

where I_{ta} is the MOI about the test axis and $\dot{h}_{max_{acs}}$ is the maximum available torque from the ACS. Equation (3.25) can be rearranged to solve for the amplitude of the desired oscillation A from

$$A < \left(\frac{1}{2\pi f}\right)\frac{\dot{h}_{max_{acs}}}{I_{ta}}I_{ta}. \tag{3.26}$$

Due to uncertainties in the MOI and the presence of additional disturbance torques,

the available torque was reduced to produce a 50% safety margin. An additional safety margin was implemented by substituting the largest expected MOI I_{max} into Eq. (3.26). These two substitutions result in

$$A_{des} \approx \left(\frac{1}{4\pi f}\right) \frac{\dot{h}_{max_{acs}}}{I_{max}}.$$ (3.27)

From here, a limitation of the experiment duration was used to determine the frequency of the oscillation. The satellite simulator, SimSat, has repeatedly undergone 50-60 s maneuvers without risk of reaction wheel angular momentum saturation. As a result, the desire was to keep the maneuver to approximately 50-60 s. Additionally, in order to accurately estimate the linear trend in the angular momentum as a result of zero-order disturbance torques, multiple complete cycles were desired. With this in consideration, a period of 12 seconds was chosen as it would result in four complete cycles, and is enough to clearly identify a linear trend in the RW data. By defining the frequency f as

$$f \triangleq \frac{1}{12\,\mathrm{s}}$$ (3.28)

substitution into Eq. (3.27) allows for the calculation of the desired amplitude of A_{des} to be a maximum of $0.02\,\mathrm{rad}/\mathrm{sec}$. Substituting the calculated value for A_{des} into Eq. (3.17) results in the equation for the desired maneuver rotation rate

$$\omega = 0.02 \sin\left(\frac{2\pi t}{12}\right).$$ (3.29)

In order to verify that the maneuver is approximately $\pm 2°$, the size of Dabrowski's most effective maneuver while maintaining small higher order disturbance torques, simple integration of Eq. (3.29) can be performed to conclude that the maneuver will be approximately $\pm 2.18°$ which is only slightly larger than the $2°$ maneuver

implemented by Dabrowski. The maneuver was implemented on SimSat and the measured rotation rate is shown in Fig. 3.5(a) and the corresponding RW angular momentum is shown in Fig. 3.5(b). As evident in Fig. 3.5(b) there are significant disturbance torques and in the next section we will discuss the effects of disturbance torques on the data, and we will discuss the method we implemented to remove the effects of zero-order disturbance torques.

(a) Measured SimSat Angular Rates   (b) Measured SimSat RW Angular Momentum
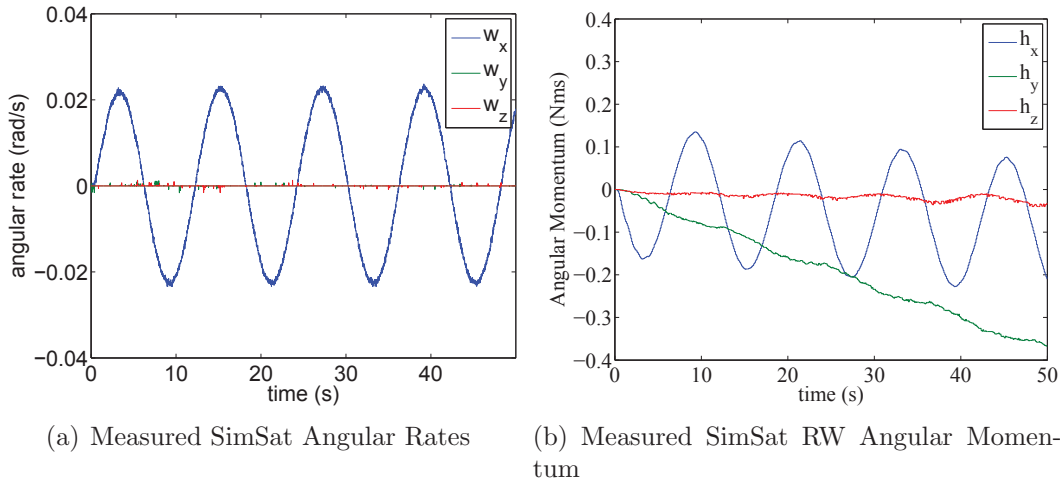
Figure 3.5. SimSat Angular Rates and RW Angular Momentum

3.4   Zero-Order Disturbance Torques

In this section, potential zero-order disturbance torques will be analyzed. One of the largest disturbance torques on satellite attitude simulators is due to imbalance. Since the satellite simulator rotates about the center of a sphere instead of the center of mass, the displacement from the center of mass and the center of rotation, crossed with the gravitational vector, generates a disturbance torque. Due to the severity of the disturbance torque associated with imbalance, most satellite simulators have balancing systems that allow for the platform to be crudely balanced. However, since all balance methodologies rely on an estimation from noisy measurements, the

platform can never be perfectly balanced and the potential for disturbance torques associated with imbalance need to be accounted for.

For a perfectly balanced satellite the disturbance torque may be negligible; however, if the satellite attitude simulator is not perfectly balanced, the resulting torque could have adverse effects on the MOI estimation. Figure 3.6(a) depicts a perfectly balanced satellite attitude simulator, and Fig. 3.6(b) shows the same satellite simulator with a defined Cartesian "inertial" coordinate system. Since the center of mass is exactly at the same location as the center of rotation, there is no torque associated with an imbalance.
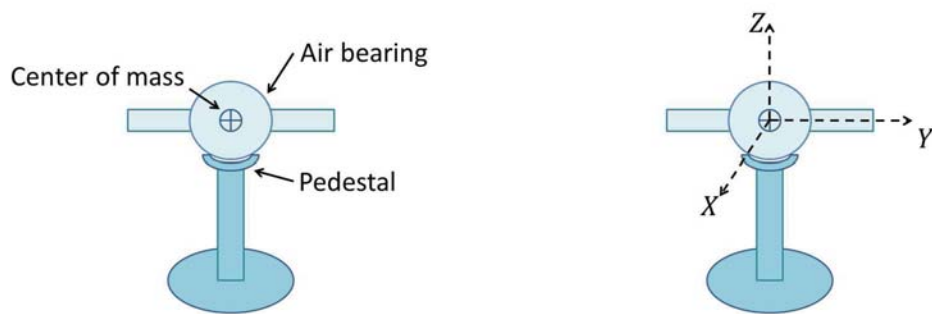
(a) Perfectly Balanced Satellite Simulator Depicting Colocation of Center of Mass and Center of Rotation

(b) Defined Inertial Frame with Origin at Center of Rotation

Figure 3.6. Satellite Attitude Simulator and Inertial Coordinate System

Figure 3.7(a) shows a representative satellite simulator with a mass of m_y added at a distance L_y in the $Y-$axis. The addition or presence of this mass in the $Y-$axis generates a negative torque τ_{x_y} about the $X-$axis as a result of the imbalance in the $Y-$axis. Subsequently, the term τ_{x_z} will later be used to denote the torque in the $X-$axis as a result of an imbalance in the $Z-$axis. The torque τ_{x_y} equal to the distance between the forces L_y times the magnitude of the forces which in this case is m_y times the gravitational acceleration.

(a) Satellite Simulator Imbalance Y-Axis   (b) Torque Due to Imbalance in Y-Axis

Figure 3.7. Imbalance in Y-Axis and Subsequent Torque

Figure 3.7(b) shows the same satellite simulator after a rotation of θ about the X-axis. In Fig. 3.7(b) it is apparent that the moment arm of the torque couple has decreased as a function of θ, resulting in a disturbance torque of

$$\tau_{xy} = -m_y g L_y \cos(\theta) \tag{3.30}$$

where θ is the angle of rotation about the $X-$axis.

For relatively small maneuvers like the one proposed in Sec. 3.3.2, the magnitude of θ is less than $2.5°$ justifying implementing a small angle approximation to reduce Eq. (3.30) to

$$\tau_{xy} \approx -m_y g L_y. \tag{3.31}$$

This disturbance torque can then be integrated over the period of 0 to t

$$h_{\tau_{xy}}(t) \approx \int_0^t -m_y g L_y \, dt \tag{3.32}$$

to calculate the change in angular momentum due to the presence of this disturbance torque

$$h_{\tau_{xy}}(t) \approx -m_y g L_y t. \tag{3.33}$$

This nearly constant torque for small angles would create a linear trend in the angular momentum. Figure 3.8(a) shows the angular momentum of the RW array as a result of the maneuver shown in Fig. 3.5(a), and Fig. 3.8(b) shows only the angular momentum stored in the test axis. Additionally, Fig. 3.8(b) shows two parallel lines to better emphasize the linear trend of the angular momentum. Since the maneuver is intended to be pure rotation about the test axis, any angular momentum stored in the non-test axis will produce a reactive torque that is also perpendicular to the test axis. As a result, the angular momentum in the other axes can be disregarded.

It is apparent from Fig. 3.8(b) that there are disturbance torques that, if not correctly accounted for, will introduce errors into the MOI approximation.

3.4.1 Removing Zero-Order Disturbance Torques.

Due to the shape of the maneuver, the angular momentum associated with the maneuver is expected to be in the form of a linear combination of a sine and cosine at a frequency of 1 cycle every twelve seconds. The zero-order disturbance torque is expected to add a linear component with respect to time, and any transient angular momentum would introduce an initial offset that is completely independent of time. As a result, an equation for the angular momentum stored in the RW is assumed to be of the form

$$h_{rw} = mt + b + D\sin(2\pi f t) + E\cos(2\pi f t) \tag{3.34}$$

where h_{rw} is the angular momentum of the RW array about the test axis; ω is the frequency of the oscillation; and m, b, D, and E are coefficients that best fit the

51
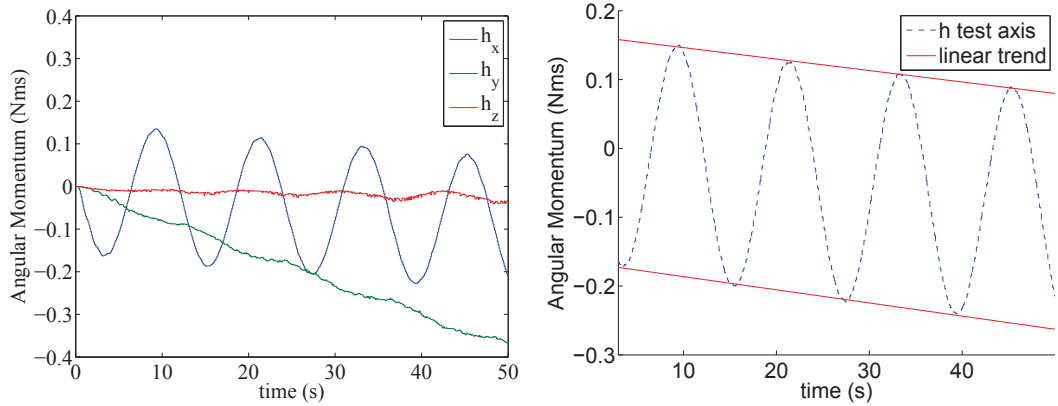
(a) Measured RW Angular Momentum in all 3 Axes in Body Frame

(b) Measured RW Angular Momentum about the Test Axis Clearly Showing Linear Trend
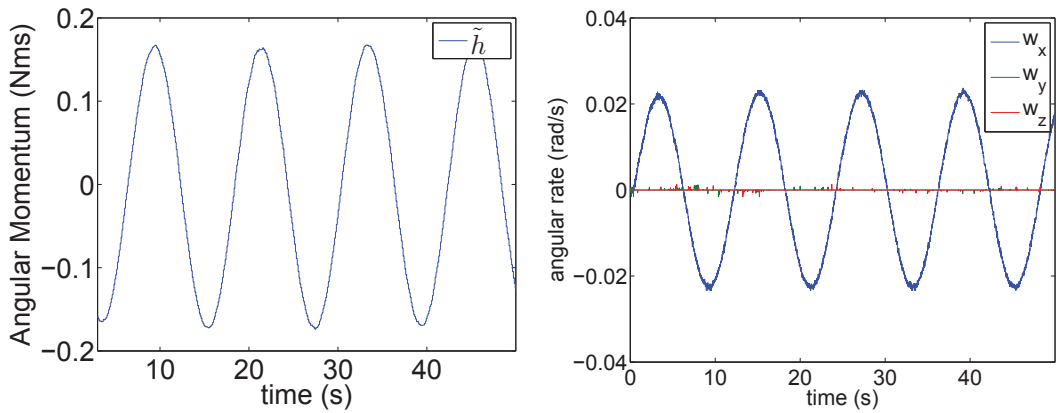
(c) Measured Reaction Wheel Angular Momentum About Test Axis Without Linear Trend from Eq. (3.35)

(d) Satellite Rotation Rates

Figure 3.8. Sinusoid Maneuver Reaction Wheel Momentum and Spacecraft Rotation Rates

measured angular momentum of the RW in the test axis. It is important that the linear trend mt be removed since we are using a low-order Fourier approximation to estimate the amplitude of the oscillation and any linear trend will result in errors in the estimated amplitude and subsequent MOI estimate. To remove the effect of the zero-order disturbance torque, the first-order term in the angular momentum data is removed by calculating a corrected angular momentum $\tilde{h}_{rw}$ as

$$\tilde{h}_{rw} = h_{rw} - mt. \tag{3.35}$$

An example of what the RW angular momentum looks like before and after the linear detrend are shown in Fig. 3.8(a) and 3.8(c) respectively.

Once the linear trend has been removed a second-order Fourier approximation is then calculated for the RW angular momentum data and the MOI is estimated as discussed in Sec. 3.3.3. In the next section, the MOI will be estimated about a single axis. After the MOI is estimated about a single axis, the sensitivity to first-order disturbance torques will be analyzed and a method to remove the first-order torques will be developed and implemented.

3.4.2 Single Axis Results.

The RW angular momentum and SimSat maneuver data from Figs. 3.8(a) to 3.8(d) were the results of a single MOI estimate maneuver about the $X-$axis. The RW momentum data shown in Fig. 3.8(c) resulted in a Fourier approximations of an amplitude of 0.1544 Nms at a phase of 171.27°. Additionally, the amplitude and phase shift of Fourier approximation of SimSat angular velocity from Fig. 3.8(d) was 0.0224 rad/sec and -7.31° respectively. After dividing the latter amplitude of 0.0224 rad/sec into the former amplitude of 0.1544 Nms the MOI estimate is calculated as 6.90 kgm^2. Using that value as the baseline, the residual angular momentum can be calculated as

$$r = h_{rw} + I\omega \tag{3.36}$$

where r is the residual, I is the calculated MOI estimate of 6.90 kgm^2, h_{rw} is the angular momentum of the RW from Fig. 3.8(c), and ω is SimSat angular velocity

from Fig. 3.8(d). The results are shown in Fig. 3.9(a).

(a) Residual without Phase Shift (b) Residual after Phase Shift Correction
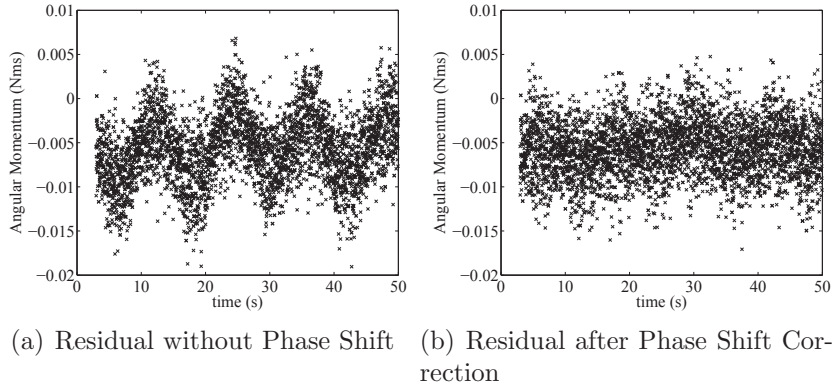
Figure 3.9. Residual Angular Momentum from MOI Approximation

The dominant oscillation in the residual is shown clearly in Fig. 3.9(a). However, it was predicted that there could be an error associated with the time delay between multiple data collection sources, and the proposed method of MOI estimation was intended to be able to correct for any time delay. With this in consideration, the phase angles of SimSat and the RW were compared. Although the data still has a 178.59° difference, Newtonian dynamics tells us that this should be 180°. Additionally, by knowing the frequency of the oscillation, a time delay associated with this angular difference can be calculated as a 0.0471 second lag in the RW data. Since the RW data is the smoother of the two samples, the RW data was advanced by 0.0471 seconds, linearly interpolated, and re-discretized at the original time steps to allow for comparison to the IMU data. The residuals were re-calculated and are shown in Fig. 3.9(b). From Fig. 3.9(b) it is concluded that the remaining residual was predominantly a result of noise in the sensor data and when compared to the RW angular momentum of approximately ± 0.15 Nms represents approximately 3% of the measured value. As a result of both of these aspects, and the MOI estimation maneuver and calculation were deemed successful.

We estimate the 0.0471 second lag in the RW data to be a combination of two

time delays. Although the on-board controller operates at 1000 Hz, it is important to note that the RW data is only collected at 10 Hz and the RW data is then stored for the on-board feedback-linearized controller. To minimize errors, the least-squares estimate will favor a time delay of half of the 10 Hz time step. Therefore, we expect the least-squares estimate to calculate a 0.05 second lag in the RW data. Additionally, the data from the IMU undergoes a ten time-step rolling average. As a result, the current IMU data is actually a better representative of the IMU data from five time steps previous to the current time step or a 0.005 second lag. The difference in these two time-delays is 0.045 seconds, very close to the measured 0.0471 seconds.

The linear trend removal, Fourier approximation, and MOI estimation process was accomplished for each of the five maneuvers. The histogram data for the five runs can be seen in Fig. 3.10(a). To better compare these results with the results of previous estimation methods, the values have been normalized and shown in Fig. 3.10(b).

(a) Histogram of X-Axis MOI Approxima-tions

(b) Normalized Histogram of X-Axis MOI Approximations
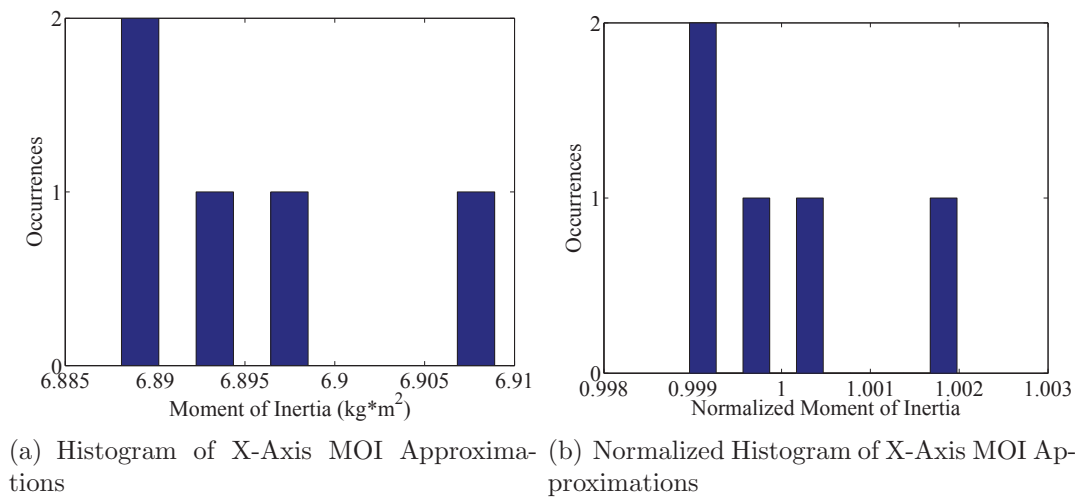
Figure 3.10. Histogram of Test Axis MOI Approximations

The results from the single axis MOI estimation process show all five measurements are within 0.21% of the mean estimate value. This suggests significant improvement over the results from previous efforts to approximate SimSat MOI with

55

average sample deviations of approximately 2.5% [6].

3.5 First-Order Disturbance Torques

In Sec. 3.4 the zero-order disturbance torques as a result of imbalance in the $Y-$axis were identified and removed from the RW data. The imbalance in the $Z-$axis results in a first-order torque with respect to θ. This higher order torque means that for small deviations from the origin, the imbalance in the $Z-$axis should generate a considerably smaller torque than an equivalent imbalance in the $X-$ or $Y-$axes. The higher order nature of the first-order disturbance torque makes it significantly harder to estimate the imbalance in the $Z-$axis meaning there is a good chance that the imbalance in the $Z-$axis can be larger than the imbalance in the $X-$ or $Y-$axes. As a result, the previously implemented assumption that the first-order disturbance torques are trivial will not be made. Instead, a realistic value for the imbalance in the $Z-$axis will be used in order to determine if a realistic imbalance in the $Z-$axis will result in negligible effects to the MOI estimation.
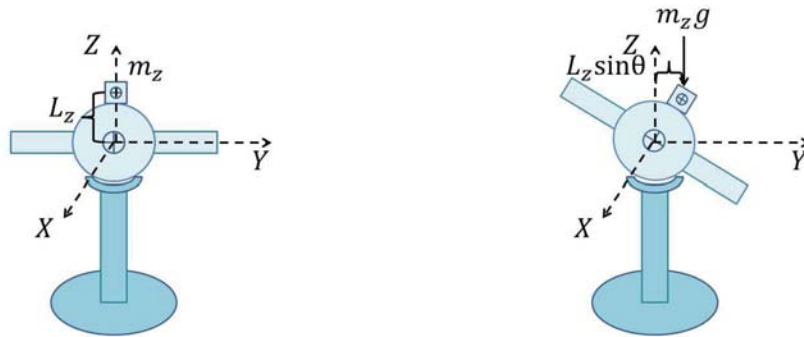
(a) Satellite Simulator Imbalance Z-Axis   (b) Torque Due to Imbalance in Z-Axis

Figure 3.11. Imbalance in Z-Axis and Subsequent Torque

Figure 3.11(a) shows an imbalance due to a weight that moves the center of mass above the $X-Y$ plane. It is apparent in Fig. 3.11(a) that the imbalance in the $Z-$axis

56

will not result in a torque, as long as the body frame $Z-$axis remains aligned with gravity vector, defined as the inertial $Z-$axis. However, when the satellite simulator begins to rotate as depicted in Fig. 3.11(b) there is a torque equal to

$$\tau_{xz} = m_z g L_z \sin(\theta). \tag{3.37}$$

In addition we define h_e as the error in the angular momentum as a result of a disturbance torque, and $\dot{h}_e$ as the instantaneous disturbance torque. If the torque due to an imbalance is undesirable, we can consider it a disturbance and if we assume it is the only disturbance torque we can define the disturbance torque as

$$\dot{h}_e = \tau_{xz}. \tag{3.38}$$

The angular rate ω of the desired maneuver is defined in Eq. (3.29) as a function of time. By integrating Eq. (3.29) with respect to time we can calculate the angle θ as

$$\theta(t) = \frac{-0.12}{\pi} \cos\left(\frac{2\pi t}{12}\right) + C. \tag{3.39}$$

where C is the constant of integration. For this maneuver, C was set to zero, so the oscillation will be centered about $0°$ in the X-axis and the maneuver actually begins with the spacecraft in a $-2.18°$ orientation. Substituting the Eq. (3.39) into Eq. (3.37) produces

$$\dot{h}_e = m_z g L_z \sin\left(\frac{-.12}{\pi} \cos\left(\frac{2\pi t}{12}\right)\right). \tag{3.40}$$

Since the magnitude of θ is never more than $2.19°$, the following small angle approximation can be made

$$\sin\left(\frac{-.12}{\pi}\cos\left(\frac{2\pi t}{12}\right)\right) \approx \frac{-.12}{\pi}\cos\left(\frac{2\pi t}{12}\right). \tag{3.41}$$

The approximation from Eq. (3.41) reduces Eq. (3.40) to

$$\dot{h}_e \approx \frac{-.12 m_z g L_z}{\pi}\cos\left(\frac{2\pi t}{12}\right). \tag{3.42}$$

Integrating Eq. (3.42) results in

$$h_e \approx \frac{-.72 m_z g L_z}{\pi^2}\sin\left(\frac{2\pi t}{12}\right) + C_2 \tag{3.43}$$

where C_2 is a constant of integration, but is accounted for in the Fourier approximation process and will not introduce an error into the amplitude estimation. Therefore, this constant of integration will be set to zero. Since Eq. (3.40) still can't be completely defined, we will normalize the equation by selecting a normalization scheme of $120\,\mathrm{g}$ and $1\,\mathrm{cm}$ for m_z and L_z, respectively. The value $120\,\mathrm{g}$ was chosen because of the balance system on SimSat which uses sliding weights of slightly over $100\,\mathrm{g}$. After substitutions, Eq. (3.40) becomes

$$h_e \approx -8.58 \times 10^{-4} \sin\left(\frac{2\pi t}{12}\right). \tag{3.44}$$

Written in vector form, the reaction wheel angular momentum $\vec{h}_{rw}$ can be considered the sum of the unperturbed angular momentum value $\vec{h}_{rw_0}$ which is required to produce the maneuver and the angular momentum as a result of the integration of a disturbance torque $\vec{h}_{rw_e}$.

$$\vec{h}_{rw} = \vec{h}_{rw_0} + \vec{h}_{rw_e}. \tag{3.45}$$

As previously stated in Sec. 3.3.3, the MOI is calculated from the amplitude of the

Fourier approximation of the RW angular momentum $\vec{h}_{rw}$ from Eq. (3.22). Since $\vec{h}_{rw_0}$ is expected to be a sinusoid at the same frequency as $\vec{h}_{rw_e}$, when a Fourier approximation of $\vec{h}_{rw}$ is calculated, the amplitude of the sinusoid $A_{h_{rw}}$ will be approximately equal to the unperturbed amplitude of the RW assembly $A_{h_{rw_0}}$ plus the amplitude of the disturbance angular momentum A_{rw_e}. When the amplitude of the RW angular momentum $A_{h_{rw}}$ is divided by the amplitude of the Fourier approximation of the spacecraft's angular velocity $A_{w_{sc}}$ an estimate of the spacecraft's MOI is calculated

$$MOI_{est} \approx \frac{A_{h_{rw_0}}}{A_{w_{sc}}} + \frac{A_{rw_e}}{A_{w_{sc}}}. \tag{3.46}$$

Adding an A_{rw_e} of 8.58×10^{-4} Nms to the example given in Sec. 3.4.2 of 0.1544 Nms RW angular momentum and a SimSat rotation rate amplitude of .0224 rad/sec results in a .0380 Kgm^2 MOI error being added to a estimated 6.90 Kgm^2. This means that a weight as small as 120 g being as little as 1 cm out of place in the Z-axis can result in a 0.5% error in MOI approximation. Figure 3.10 shows the data collection and MOI estimation method produces estimates with a standard deviation of five runs of approximately 0.0073 kgm^2. Since it appears safe to assume that the torque associated with an imbalanced satellite simulator will be relatively consistent between runs, the disturbance torque associated with a 120 gcm imbalance in the $Z-$axis would result in a bias that is five times larger than the sample deviation of the estimation method. This offset would be undetectable to researchers using only a standard deviation as a metric of validity. It is concluded that in order to ensure the accuracy of the MOI estimates the disturbance torques themselves need to be estimated before sub 1% error can be obtained with the desired estimation process. Unlike the zero-order torque, the angular momentum as a result of the first-order torque cannot easily be identified and removed from the data. However, if the first-order torques are well characterized, an estimated angular momentum error can be calculated and subtracted from the RW

angular momentum data, much like the linear trend was subtracted in Eq. (3.35). As a result, the first-order torques about the test axes will need to be analyzed and an imbalance in the $Z-$axis needs to be estimated. In order to do this, a torque characterization maneuver was implemented.

3.6   Torque Characterization Maneuver

In Sec. 3.5 the sensitivity to first-order disturbance torques of the proposed maneuver was analyzed. It was concluded that the first-order torque associated with relatively small imbalances in the $Z-$axis could introduce an undesired bias. Therefore, the disturbance torques themselves need to be accurately analyzed before expecting to accurately estimate the MOI. To estimate the first-order torques being imparted on the satellite simulator, a maneuver was performed to estimate the disturbance torques as a function of the position θ. The maneuver chosen was a 40 second rotation about the $X-$axis from approximately -20 degrees to 20 degrees at the constant rotation rate ω of $1°/\text{sec}$ ($0.017^{\text{rad}}/_{\text{sec}}$). The quaternions for the maneuver are shown in Fig. 4.4(a) and the angular rates of the maneuver are shown in Fig. 4.4(b).

(a) Torque Characterization Quaternions   (b) Torque Characterization Angular Rates
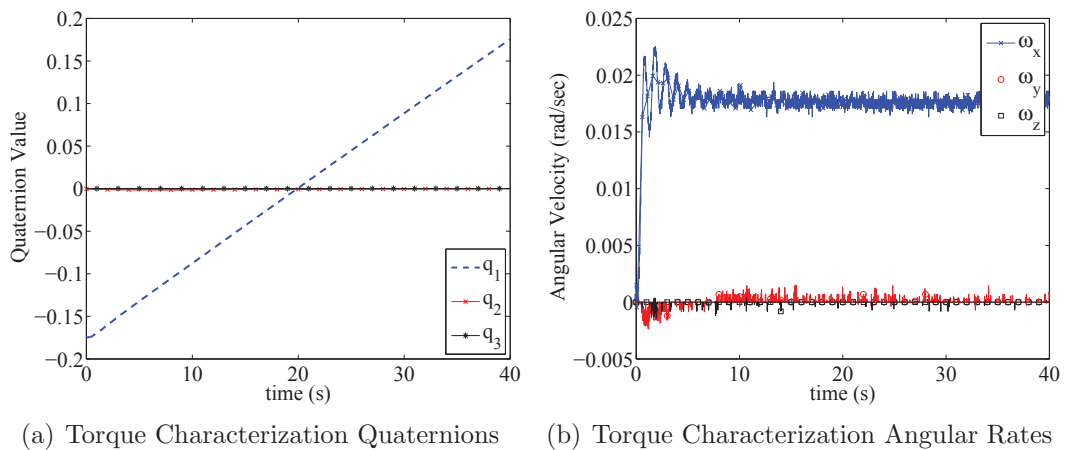
Figure 3.12. Torque Characterization Maneuver

Since the angular velocity of the spacecraft is constant the angular momentum of

60

the spacecraft would also be constant in the absence of disturbance torques. If we assume that there are disturbance torques only as a result of an imbalance in the $Y-$ and $Z-$axes, then the disturbance torque about the $X-$axis would be a function of the angle of rotation θ about the $X-$axis and can be expressed as

$$\dot{h} = A\sin(\theta) + B\cos(\theta). \tag{3.47}$$

A nonzero value for A would be indicative of an imbalance in the $Z-$axis, likewise a nonzero and B would be indicative on the imbalance in the $Y-$axis. If it is assumed that $\dot{\theta}$ is relatively constant, and the maneuver is specifically defined to accomplish this, then Eq. (3.47) can be integrated with respect to time as

$$h = \frac{-A}{\dot{\theta}}\cos(\theta) + \frac{B}{\dot{\theta}}\sin(\theta) + h_0. \tag{3.48}$$

Since the reaction wheels are being used to maintain the constant velocity maneuver, the torque that is being applied to the spacecraft will be transferred and stored in the RW assembly as a change in angular momentum. Due to assumption that there may exist higher-order disturbance torques, a symbol representing the H.O.T. is added for the sake of completeness. Taking both of these into consideration, the equation can now be written.

$$h_{rw} = \frac{-A}{\dot{\theta}}\cos(\theta) + \frac{B}{\dot{\theta}}\sin(\theta) + h_{20} + \text{H.O.T.} \tag{3.49}$$

Where h_{20} is the constant of integration. By collecting the values of h_{rw}, $\sin(\theta)$, and $\cos(\theta)$ as follows

$$[\bar{h}_{rw}] \approx \mathbf{A} \begin{bmatrix} A \\ B \\ h_{20} \end{bmatrix} \tag{3.50}$$

where the matrix a $\mathbf{A}$ is defined as

$$\mathbf{A} = \begin{bmatrix} \dfrac{-\cos(\bar{\theta})}{\dot{\theta}} & \dfrac{\sin(\bar{\theta})}{\dot{\theta}} & \bar{1} \end{bmatrix} \tag{3.51}$$

where $\bar{h}_{rw}$, $\bar{\theta}$, $\bar{1}$ are one dimensional arrays the length of the collected data set for the given experiment. A least-squares estimate of A, B, and h_{20} can be calculated as

$$\begin{bmatrix} A \\ B \\ h_{20} \end{bmatrix} = \mathbf{A}^+ \begin{bmatrix} \bar{h}_{rw} \end{bmatrix} \tag{3.52}$$

where $\mathbf{A}^+$ is the Moore-Penrose pseudo-inverse of $\mathbf{A}$.

The major assumption that is made during this process is that the disturbance torques can be characterized as zero- and first-order effects with respect to the angle θ. In order to validate this assumption, the values of A and B from Eq. (3.52) are substituted back into Eq. (3.49) along with $\sin(\theta)$ and $\cos(\theta)$ to calculate h_{est}. The angular momentum estimate h_{est} is defined as

$$h_{est} = \frac{-A}{\dot{\theta}} \cos(\theta) + \frac{B}{\dot{\theta}} \sin(\theta) + h_{20} \tag{3.53}$$

where $\dot{\theta}$ is assumed constant and is calculated from the average of the IMU data after discarding the transient data associated with initialization.

The calculated values of h_{est} are then plotted against the measured values of h_{rw} and a sixth-order polynomial approximation of h_{rw}. The three data sets are shown in Fig. 4.15(a). The order of six was chosen to be arbitrarily large to ensure that all of

the higher order disturbance torques could be accounted for. Due to the differential relationship, a sixth-order approximation for the angular momentum is equivalent to a fifth-order disturbance torque approximation. Although Fig. 4.15(a) shows slight disagreements at displacements over 10°, Fig. 4.10 zooms to ±5sec about neutral angular position and shows little difference between the first- and fifth-order estimates for small displacements in θ. The time interval shown in Fig. 4.10 corresponds to angular displacements of ±5°, as a result, a first-order approximation of the disturbance torques is deemed sufficient for the proposed ±2.18° MOI estimation maneuver.
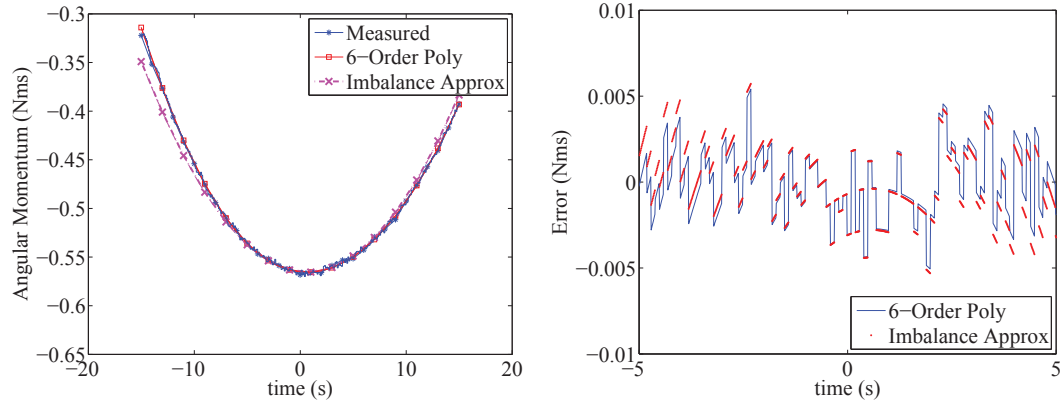
(a) Angular Momentum of Reaction Wheels vs Time

(b) Residuals for 6-Order Polynomial and Simulated Imbalance

Figure 3.13. Torque Characterization Maneuver

If we apply a rigid body assumption, we can assume that the first-order disturbance torque as a function of θ is due to an imbalance in the $Z-$axis. Subsequently, the imbalance in the $Z-$axis can be calculated as

$$A = m_z g L_z \tag{3.54}$$

and the imbalance in the $Y-$axis can be calculated as

$$B = -m_y g L_y. \tag{3.55}$$

63

As done previously, $120\,\mathrm{g}$ was substituted into m_y and m_z and the equations were then solved for the error in the position of the balancing weights, d_y and d_z

$$d_z = \frac{A}{(.120)(9.81)} \tag{3.56}$$

and

$$d_y = \frac{-B}{(.120)(9.81)} \tag{3.57}$$

It should be noted that up to this point d_x has been intentionally left out because the spacecraft is not rotating about the Y body axis. As a result, the torque applied to the spacecraft about the Y-axis should be constant. Therefore, the angular momentum built up in the inertial Y-axis should be relatively linear and the slope of which is the disturbance torque associated with the imbalance in the X direction can be expressed as

$$h^I_{rw_y} \approx C_{1_x} t + C_{2_x} \tag{3.58}$$

where $h^I_{rw_y}$ is the angular momentum of the RW in the inertial Y direction and is calculated as

$$h^I_{rw_y} = h_{rw_y} \cos(\theta) + h_{rw_z} \sin(\theta). \tag{3.59}$$

Once a linear approximation of the inertial angular momentum in the Y-axis is calculated, the imbalance in the X-axis can be solved with the following equation

$$C_{1_x} = m_x g L_x \tag{3.60}$$

and similarly to d_y and d_z, d_x is then defined as

64

$$d_x = \frac{C_{1_x}}{(.120)(9.81)}. \tag{3.61}$$

Once the imbalance was estimated, the torque characterization maneuver about the X-axis was repeated four more times, for a total of five estimates. The results from the five runs were consistent with none of the five measurements in the $X-$, $Y-$, or $Z-$axes being more than $1-$cm away from the average of the respective data samples. The process was then repeated about ten test axes $\tilde{X}$ in the $X - Y$ plane at ten degree increments of Φ as shown in Fig. 3.14.
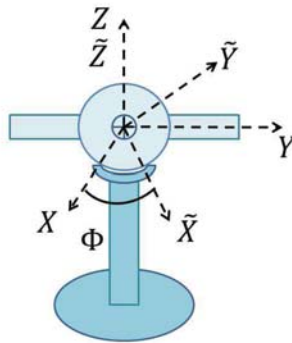
Figure 3.14. Redefined Maneuver Axis $\tilde{X}(\phi)$

For each $\tilde{X}$-axis the mean of the five runs was calculated and the five residuals were calculated. Figures 3.15(a), 3.15(c), and 3.15(e) show the mean imbalance estimation for each axis, error bars representing the standard deviations about each test axis, and a ±1(cm) dashed line for a reference to how precise the estimations are. The histograms in Figs. 3.15(b), 3.15(d), and 3.15(f) show the fifty residuals that resulted from the five runs about each of the ten axes.

Figures 3.15(a), 3.15(c), and 3.15(e) show the estimated imbalance varies as the test axis varies from the X to Y body axis. Due to the high degree of precision about each axis, it is assumed that the imbalance is not changing as a function of time. The
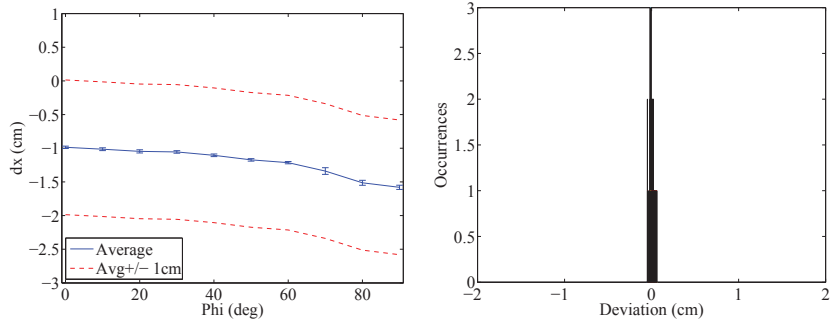
(a) X-Axis Imbalance Estimates vs Axis of Rotation

(b) Sixty Residual Histogram of Imbalance in X-Axis
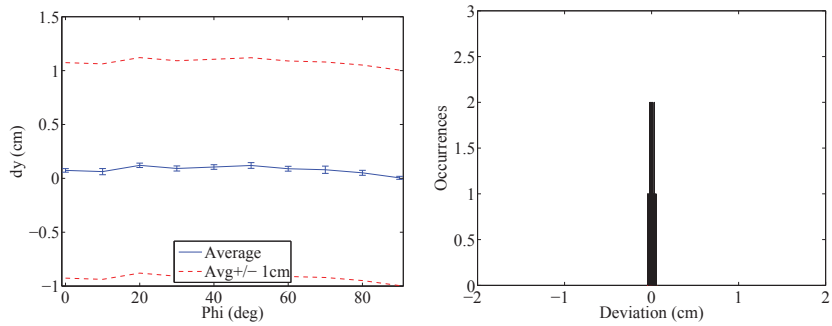
(c) Y-Axis Imbalance Estimates vs Axis of Rotation

(d) Sixty Residual Histogram of Imbalance in Y-Axis
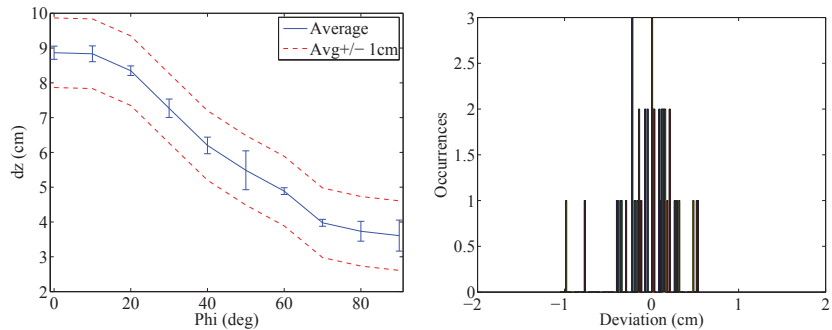
(e) Z-Axis Imbalance Estimates vs Axis of Rotation

(f) Sixty Residual Histogram of Imbalance in Z-Axis

Figure 3.15. Imbalance Estimates and Histograms

moving of the imbalance estimate instead suggests an inappropriate application of the rigid body assumption, as first-order structural flexing in the $Y-$axis which would vary as a function of the rotation axis, appears to be effecting the estimate. Even though the disturbance torque varies as a function of the rotation axis, for any given

axis this disturbance torque is relatively consistent with Fig. 3.15(f) showing that a vast majority of the fifty measurements were within $\pm 1\,\mathrm{cm}$ of the mean estimate for the respective test axes. The combination of these two assessments result in the conclusion that although the dominant first-order disturbance torque is not an imbalance in the $Z-$axis, it can be relatively well approximated as an "imbalance" in the $Z-$axis, provided that "imbalance" estimate used is calculated from a disturbance torque characterization maneuver about the desired test axis. As a result, prior to the five MOI data collection maneuvers about each axis, five "imbalance" characterization maneuvers will be performed in order to approximate first-order disturbance torques about the test axis.

Once the five torque characterization maneuvers are performed, five MOI data collection maneuvers will be performed. Afterwards, the "imbalance" will be calculated from the five torque characterization maneuvers. This imbalance will then be applied to the MOI maneuvers where the "imbalance" will be transformed into a torque in the inertial frame, integrated with respect to time, rotated into the body frame and subtracted from the RW measurements. The resulting RW measurements can then be used to estimate the MOI without inducing the $0.5\%\,\mathrm{kgm}^2$ error for every $120\,\mathrm{gcm}$ of imbalance. Instead, the first-order disturbance torque will only introduce a bias proportional to the precision of the first-order imbalance estimate which from the data shown in Fig. 3.15(f) is approximately a normal distribution with a single sigma uncertainty of $\pm 40\,\mathrm{gcm}$. From our calculations in Sec. 3.5 the error associated with the one sigma uncertainty in the precision of the first-order disturbance torque will integrate to produce one sigma bias of approximately $\pm 0.013\,\mathrm{Kgm}^2$, or an error of approximately $\pm 0.17\%$ in the MOI estimation of the $X-$axis. The data from these sixty maneuvers allows us to not only correct for the disturbance torque but estimate the accuracy of our MOI estimate based on the precision of the first-order torque

characterization. The next section will cover the experimental results first without and then with the first-order disturbance torque removal in order to analyze necessity to include the first-order analysis in future MOI estimates.

3.7   Experimental Results

In order to validate the benefit of the removal of the first-order torques, the estimation process was implemented twice, first without the first-order torque correction and then again with the first-order torque correction. As mentioned in Sec. 3.3.1 the process comprised of twelve MOI estimates about twelve axes in a hemispherical quadrant. The results from the MOI approximation maneuver are shown in Table 3.1.

The first two columns in Table 3.1 are the latitude and longitude of the test axis which were given as reference to better understand the axes locations on the hemispherical quadrant. As presented, the $X-$axis would be at $0°$ Latitude and $0°$ Longitude and the $Y-$axis is at $0°$ Latitude and $90°$ Longitude. The experimentally estimated MOI are listed in third column. The fourth column shows the calculated MOI as a result of all twelve estimations and twelve standard deviations that are shown in the sixth column. The deviation between the experimentally estimated and the calculated MOI are listed in the fifth column.

The data shown in Table 3.1 result in the following MOI matrix

$$\mathbf{I} = \begin{bmatrix} 6.886 & -0.162 & -0.124 \\ -0.162 & 9.876 & -0.126 \\ -0.124 & -0.126 & 12.856 \end{bmatrix}. \tag{3.62}$$

As previously suggested, this method has the ability to over-determine the ellipsoid, and use the relative measurements of each of the vectors to help validate the accuracy of the individual measurements. As shown by the measurement along the

Table 3.1. Single Axis MOI Estimates without First-Order Torque Correction

Latitude	Longitude	Measured MOI	Best Fit Ellipsoid MOI	Deviation	Std Dev
0	0	6.90	6.89	-0.01	0.01
0	90	9.89	9.88	-0.02	0.01
90	0	12.85	12.86	0.01	0.01
0	30	7.77	7.78	0.01	0.01
0	60	9.28	9.28	-0.00	0.01
30	0	8.48	8.49	0.00	0.01
30	30	9.19	9.19	0.00	0.01
30	60	10.32	10.31	-0.01	0.01
30	90	10.71	10.72	0.01	0.01
60	0	11.46	11.47	0.01	0.01
60	45	11.95	11.93	-0.03	0.01
60	90	12.22	12.21	-0.01	0.02

vector relatively 60 Latitude and 45 Longitude, the number of standard deviations from the measured approximation and the least squares approximation is 2.33. The probability of an individual estimate having such a large number of deviations is approximately 2%, which requires a sample size of 34 estimates for a 50% probability of a single estimate having such a large error. Although this is not conclusive, it does further suggest that the previous method of linking the precision with accuracy may be optimistic.

As previously suggested in the Section 3.4 the first-order disturbance torques associated could introduce a bias to the MOI estimates. In order to counteract these effects, a method was introduced in Section 4.4 to estimate and correct for the first-order disturbance torques. The resulting first-order torque corrected MOI estimations are shown in Table 3.2.

From this table, it is clear to see that the number of standard deviations from the measured MOI and the calculated MOI are significantly reduced. With this method, the largest number of standard deviations from the measured value is approximately 1.49. With a dataset of 12, there is approximately a 50% probability of having at least one measurement that is 1.99 standard deviations away. This suggests that

Table 3.2. Single Axis MOI Estimates with First-Order Torque Correction

Latitude	Longitude	Measured MOI	Best Fit Ellipsoid MOI	Dev	Std Dev
0	0	6.459	6.455	-0.004	0.008
0	90	9.712	9.715	0.003	0.013
90	0	12.849	12.848	-0.001	0.011
0	30	7.436	7.450	0.014	0.009
0	60	9.093	9.080	-0.012	0.009
30	0	8.210	8.204	-0.006	0.008
30	30	8.977	8.985	0.008	0.010
30	60	10.199	10.192	-0.007	0.012
30	90	10.601	10.608	0.006	0.007
60	0	11.386	11.401	0.014	0.010
60	45	11.906	11.893	-0.012	0.011
60	90	12.184	12.174	-0.010	0.017

this methodology performs better than expected when linking the precision of the estimates with an approximation of accuracy.

The data from Table 3.2 corresponds to an MOI matrix of

$$
\mathbf{I} = \begin{bmatrix} 6.454 & -0.197 & -0.175 \\ -0.197 & 9.716 & -0.142 \\ -0.175 & -0.142 & 12.848 \end{bmatrix} \tag{3.63}
$$

3.8 Conclusion

In this chapter, a method for dynamic estimation of the MOI matrix was proposed and evaluated. This procedure started with the identification of some presumed error sources, specifically first-order torques and errors associated with time delays. The previous assumptions–trivial first-order disturbance torques, well defined time delays, and the ability to perform a pure rotation about a single axis were analyzed and shown to be invalid for SimSat. It was concluded that a deviation from more traditional methods should be made so a modified version of MOI method for POI estimation created by Wiener [39] was implemented and evaluated. Previous researchers used a

step maneuver for MOI estimation which was analyzed and deemed inefficient, noisy, and possibly unable to account for time delays. A new maneuver was proposed, implemented, and analyzed in this research that kept a larger percentage of data, could be curve fit for better noise rejection, and was experimentally shown to not be subject to time delays. In addition, the first-order disturbance torques were analyzed and deemed non-trivial. A method was proposed and implemented to estimate and remove angular momentum associated with the zero-and first-order disturbance torques. The experimental result was the identification and correction of an otherwise indiscernible 6.5% erroneous bias about the $X-$axis to a single axis MOI estimation accuracy to within approximately $\pm 0.013\, \mathrm{Kgm}^2$ or $\pm 0.17\%$ of the MOI estimate about the $X-$axis. The three components of the new MOI estimation process–methodology, maneuver, and correction of disturbance torques–were combined and experimentally evaluated on SimSat. The result was an MOI matrix that was calculated from an overdetermined set of MOI estimates resulting in an average percent deviation of approximately 0.09% and a 96% improvement over the previous methodology [6].

IV. Experimental Identification and Correction of Disturbance Torques for Satellite Attitude Simulators

Because ground-based satellite attitude simulators all have gravity torques that can't be completely removed for multi-axis maneuvers, experimental results may be unknowingly corrupted. The objective of this research is to create and analyze a disturbance torque profile for a terrestrial-based satellite attitude simulator so that gravitational disturbance torques can be quantified and reduced. It is common, when conducting research using satellite simulators, to assume the simulators are rigid bodies and the dominant zero and first-order torques are due to an imbalance. The gravitational disturbance torques that result from platform imbalance are typically reduced by rigorously balancing the satellite simulator in a nominal attitude prior to experimentation. The assumption is that rigorous balancing will effectively eliminate the zero and first-order disturbance torques is analyzed and experimentally shown to be invalid for most satellite simulators. This chapter presents a maneuver which exposes the lack of validity of the rigid body assumption, a derivation to identify a first-order disturbance torque due to structural flexing, and experimental results demonstrating the importance of platform rigidity. Ultimately, active correction is added to reduce gravitational disturbance torques by counteracting the imbalance due to structural deflections through the movement of masses with an array of linear actuators.

4.1 Introduction

Satellite simulators are commonly used to test and analyze feedback control systems and controllers in place of testing on operational satellites. However, the gravitational disturbance torques that satellite attitude simulators encounter add un-

certainty to the analysis which could lead to inconclusive or erroneous results [40].
The objective of this research is to create and analyze a disturbance torque profile for
terrestrial-based satellite attitude simulators so that gravitational disturbance torques
can be quantified and potentially reduced. We start the discussions by presenting a
series of maneuvers to identify the extent of the disturbance torques. The equations
for the disturbance torque due to structural deflection are derived, identifying a dis-
turbance torque not previously identified [34]. A set of structural reinforcements or
stiffeners were added to AFIT second generation satellite attitude simulator SimSat
in an effort to verify that the disturbance torques are in fact due to structural de-
flections and the torques are re-analyzed. Finally, an array of linear actuators were
added to move masses and actively counteract the disturbance torques. After ac-
tuator calibration the active balancing system performance is analyzed. Before we
discuss these experiments, we will first discuss some previous research using satellite
attitude simulators.

4.2 Background

Air bearing satellite simulators have been used for decades to simulate the space
environment for validation and verification of potential satellite control algorithms
[32]. One problem that continues to plague air-bearing satellite simulators are gravi-
tational torques, with the dominant component being due to an imbalance. Imbalance
is defined here as the "static" imbalance, the distance between the center of mass and
the center of rotation while the spacecraft is in a neutral position [3].

The current AFIT SimSat is shown in Fig. 4.1(a) and is the result of many years of
iterative design and test, but the one item it still lacked was an active balancing system
to correct for the gravitational disturbance torques [25]. Previous AFIT researchers
have addressed the problem by rigorous balancing prior to experimentation. They also

73

(a) Air Force Institute of Technology (AFIT) Satellite Simulator SimSat
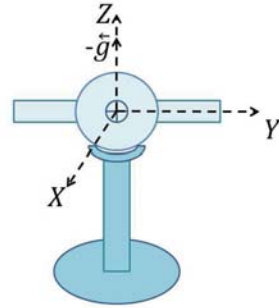
(b) Defined Body Frame and Negative Gravity Vector

Figure 4.1. Satellite Attitude Simulator and Defined Body-Frame Coordinate System

focused on the precision of the data collection and not the accuracy, the idea being that the gravitational disturbance torques will affect all of the results equally and with highly precise estimates desirable data can be collected by comparing two separate MOI estimates. Two notable instances were the works completed by Dabrowski [6] and Geitgey [11] who were using precision MOI estimates to detect parasitic satellite and remaining onboard propellant, respectively. Recently, research focuses have gone away from strictly requiring precision to requiring both precision and accuracy as discussed in Chapter III. One such example would be the analysis of non-linear controllers required for attitude control with a CMG array [41]. Unlike the linear torque generated by a RW array, the available torque from a CMG is dependent on the current orientation of each CMG in the array and any disturbance torque will likely cause a change in CMG orientation which would remove the ability to analyze certain controller characteristics such as performance at or around singularity.

Many researchers have addressed actuation systems to correct the imbalance of an air-bearing satellite simulator [17; 3; 23]. Although they differ slightly, the systems essentially use recursive estimators that use rigid body equations of motion to identify an imbalance, and then command linear actuators to correct the imbalance. We will

refer to this type of research as the dynamic correction of a static imbalance. The reason we refer to it as a "static imbalance" is due to the fact that if the rigid body assumption were true this imbalance shouldn't change as a function of time or orientation and should remain constant, or essentially static. This research effort differs from the previous researchers' efforts because we the validity of the rigid body assumption. As a result, we will be attempting to identify and actively correct for a dynamic imbalance–the imbalance as a result of structural deflections which varies depending on orientation. Before describing our approach, we will first define the torques as they will be referenced for this chapter.

4.3 Disturbance Torque Classification

For the purpose of this chapter, disturbance torques will be identified by the "order" of the torque. We define a satellite attitude simulator to be at a neutral position when the body frame $Z-$axis is aligned opposite of the gravity vector. Any deviation from this neutral position can be considered $\delta\theta$. Figure 4.1(b) shows a satellite simulator at $\delta\theta$ of 0. The gravitational disturbance torque can be expressed as a function of $\delta\theta$ by implementing a Taylor series expansion as the deviation from neutral position. An example Taylor series expansion is shown as

$$\tau = \tau_0 + \tau_1\delta\theta + \frac{\tau_2 * \delta\theta^2}{2!} + \text{H.O.T.} \tag{4.1}$$

Since the neutral position is defined as zero we can substitute the equality

$$\theta = \delta\theta \tag{4.2}$$

and express the disturbance torque as a function of θ

$$\tau = \tau_0 + \tau_1\theta + \frac{\tau_2 * \theta^2}{2!} + \text{H.O.T.} \tag{4.3}$$

It is important to note, that θ can be induced by a rotation about the body frame $X-$ or $Y-$axis or any combination thereof. For now, we will keep this generic by defining θ as any rotation that makes the $Z-$body axis and the gravity vector non-collinear. A zero-order disturbance torque is defined as the first term in the Taylor series expansion which is independent of θ. An example of a zero-order disturbance torque about the $X-$axis is an imbalance in the $Y-$axis. Figures 4.2(a) and 4.2(b) show the force and corresponding lever arms that produce the torque due to an imbalance in the $Y-$axis. Note that instead of considering an imbalance as a physical distance between the center of mass and the center of rotation, we are considering an imbalance as a mass being added to a perfectly balanced satellite simulator.
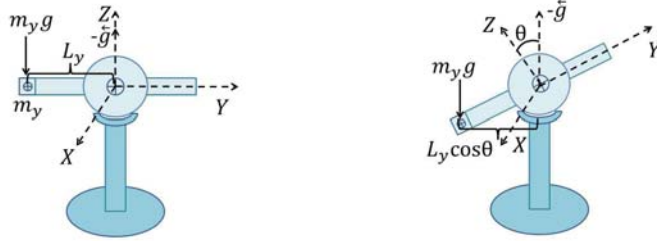
(a) Satellite Simulator Imbalance in $Y-$Axis

(b) Torque Due to Imbalance in $Y-$Axis

Figure 4.2. Imbalance in $Y-$Axis and Subsequent Torque as a function of θ

The torque corresponding to the product of the force and the lever arm is

$$\tau_{xy} = -L_y m_y g \cos\theta_x \tag{4.4}$$

where τ_{xy} is a torque about the $X-$axis as a result of an imbalance in the $Y-$axis. The other components L_y, m_y, g, and θ_x are the distance along the $Y-$axis from the

mass to the center of rotation, the mass of the weight, the acceleration due to gravity, and the rotation about the $X-$axis, respectively. If we define θ_x as a deviation from the neutral position by

$$\theta_x = 0 + \delta\theta_x, \tag{4.5}$$

a Taylor series expansion of τ_{xy} from Eq. (4.5) can be written as

$$\tau_{xy} = -L_y m_y g + \frac{L_y m_y g \theta_x^2}{2!} - \text{H.O.T.} \tag{4.6}$$

It is apparent from Eq. (4.6) that the first term of τ_{xy} would be considered a zero-order torque since the dominant component $L_y m_y g$ is independent of $\delta\theta_x$.

Subsequently, a first-order disturbance torque is a torque that if estimated by a Taylor series expansion would primarily behave linearly with respect to the deflection angle between the $Z-$axis and the gravity vector. An example of a first-order disturbance torque is an imbalance in the $Z-$axis. Figures 4.3(a) and 4.3(b) show an imbalance in the $Z-$axis and the corresponding forces and lever arms.
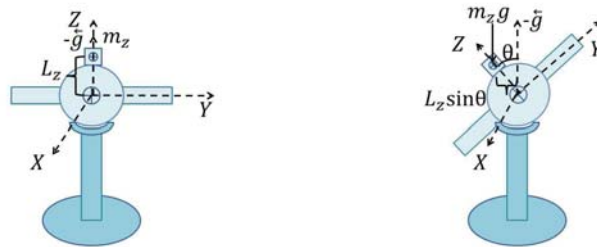
(a) Satellite Simulator Imbalance in $Z-$Axis

(b) Torque Due to Imbalance in $Z-$Axis

Figure 4.3. Imbalance in $Z-$Axis and Subsequent Torque

Equation (4.7) shows the resulting torque about the $X-$axis as a result of the imbalance in the $Z-$axis and as a function of the angle about the $X-$axis θ_x

$$\tau_{xz} = m_z g L_z \sin \theta_x \qquad (4.7)$$

where τ_{xz} is the torque in the $X-$axis as a result of an imbalance in the $Z-$axis. Similar to Eq. (4.6), m_z, g, and L_z are defined as the mass of the added weight, the acceleration due to gravity, the distance from the center of rotation to the added weight, respectively. A Taylor series expansion of Eq. (4.7) would then be

$$\tau_{xz} = m_z g L_z \theta_x - \frac{m_z g L_z}{3!} \theta_x^3 + \text{H.O.T.} \qquad (4.8)$$

As a result, the imbalance in the $Z-$axis will result in a first-order torque in the $X-$axis when rotating about the $X-$axis. Now that the disturbance torques can be described as a Taylor series approximation, we can analyze the disturbance torques about a specific axis by their order. The torque analysis begins with a torque characterization maneuver that will be discussed in the next section.

4.4   Torque Characterization

In order to estimate the disturbance torques about a given axis, we need to first explain how SimSat is controlled. There are three independent three-axis attitude control systems on SimSat: six fans, three RWs, and a four CMG array. For this first experiment, we started by using fans to hold the initial static orientation and de-spin the RW. This ensures that the initial angular momentum of the system was near zero. During the data collection, we disable the fans and only use the RW array for attitude control. Since RWs are momentum exchange devices, we know that in the absence of disturbance torques the angular momentum of the RW is equal and opposite to the angular momentum of the spacecraft. By monitoring the angular momentum of the RW and subtracting the angular momentum of the spacecraft, we can estimate the

angular momentum h_e built up as a result of the disturbance torques from

$$h_{rw}(t) = -h_{sc}(t) + h_e(t) \tag{4.9}$$

where h_{rw} is the angular momentum in the RW and h_{sc} is the angular momentum of the test platform. Since the angular momentum of the RW will be estimated using measurements that have noise, the measured data will be curve-fit using an nth-order polynomial approximation. The notation will be $h_{rw}^P(t^n)$

$$h_{rw}(t) \approx h_{rw}^P(t^n). \tag{4.10}$$

Equation (4.9) can now be approximated as

$$h_{rw}^P(t^n) \approx -h_{sc}^P(t^n) + h_e^P(t^n). \tag{4.11}$$

From Eq. (4.9), we estimate the disturbance torques by computing the time rate of change of the angular momentum $\dot{h}_e$. We simplify the calculation for the disturbance torques by implementing a maneuver consisting of a constant angular rate resulting in

$$\dot{h}_{sc}^P(t^n) \approx 0. \tag{4.12}$$

Equation (4.11) can now be differentiated with respect to time resulting in

$$\dot{h}_e^P(t^{(n-1)}) \approx \dot{h}_{rw}^P(t^{(n-1)}). \tag{4.13}$$

In addition to simplifying Eq. (4.13), the constant angular velocity ω of the spacecraft results in a simple transformation from time to θ

$$\theta = \omega t + C$$
$$\dot{\theta} = \omega$$
(4.14)

where C is a constant of integration and is $-20°$ for this experiment. Substituting the values from Eq. (4.14) into the polynomials represented in Eq. (4.13) results in

$$\dot{h}_e^P(\theta^{(n-1)}) \approx \dot{h}_{rw}^P(\theta^{(n-1)}).$$
(4.15)

The angular rate chosen for the maneuver was 0.0174 radians per second, approximately $1°$ per second. Figure 4.4(a) shows the angles θ_x, θ_y, and θ_z versus time, and Fig. 4.4(b) shows the nearly constant angular velocity for this maneuver versus time.

(a) Torque Characterization Orientation vs Time

(b) Torque Characterization Angular Rates
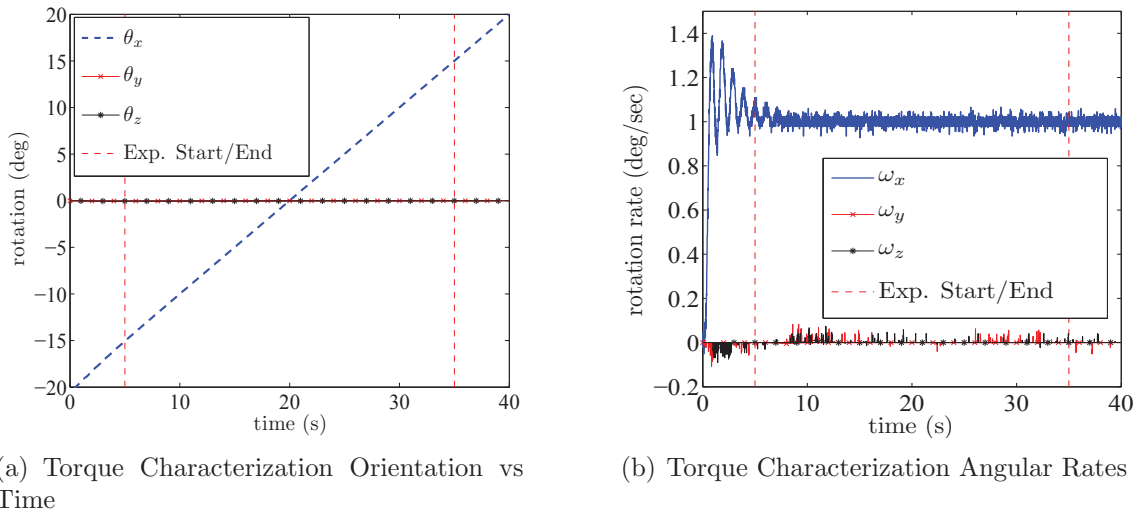
Figure 4.4. Torque Characterization Maneuver

In order to decrease the errors associated with transients, the first and last five seconds of data are discarded and the remaining ± 0.262 rad (or $\pm 15°$) of data is analyzed. The previous section presents a notation for polynomial approximations because most of the functions used in the analyses of the torque characterization maneuver are polynomial estimations of varying orders. Specifically, we reference $h^P(\theta^6)$ which differentiates to $\tau^P(\theta^5)$ which will be used as "truth" due to the inability to

differentiate the noisy RW angular momentum measurements. We use $h^P(\theta^4)$ which differentiates to $\tau^P(\theta^3)$ as the polynomial estimation of the disturbance torque. The order of $h^P(\theta^6)$ was chosen to be arbitrarily large to account for all of the disturbance torques, but we found that $h^P(\theta^8)$ started to become poorly conditioned and appeared to be picking up the transients that still exist around the 5 to 8 second mark. Additionally, $h^P(\theta^4)$ was chosen because it differentiates to $\tau^P(\theta^3)$ which is a polynomial order higher than the hypothesized significant torques which are on the order of $\tau^P(\theta^2)$. In the next section, we will discuss a second set of torque and angular momentum estimation curves, the torque and resulting angular momentum that could be generated by an imbalance.

4.4.1 Single Axis Maneuver and Local Balance.

Now we will discuss the angular momentum that would build up during a maneuver due to an imbalance which we will call h_{bal}. Due to sometimes small and varied nature of gravitational disturbance torques due to imbalance, it is often difficult to analyze the disturbance torques experienced by satellite simulators. This is because contaminated results could be due to improper balance, and a valid counterargument is that the results could be better if the spacecraft was better balanced. To avoid these criticisms and allow for better analysis of higher-order disturbance torques, a least-squares estimate of an imbalance is calculated that minimizes the error between the angular momentum resulting from the estimated imbalance h_{bal} and the angular momentum of the RW h_{rw}. The benefit of doing so is that the satellite simulator no longer needs to be perfectly balanced in order to analyze the higher-order disturbance torques, we only need to know what the imbalance is and then correct for it. Once the imbalance is known, we calculate the residual between the torque due to the imbalance τ_{bal} and the $\tau^P(\theta^5)$, a derivative of the sixth-order polynomial approximation

$h^P(\theta^6)$ of the RW angular momentum h_{rw}. The resulting residual is the disturbance torque that would be present even if the satellite simulator was perfectly balanced.

4.4.2 Local Imbalance.

In order to estimate the imbalance, we combine the zero- and first-order disturbance torques due to imbalances in the $Y-$ and $Z-$axes from Eq. (4.4) and (4.7) as

$$\tau_{bal} = -L_y m_y g \cos\theta_x + m_z g L_z \sin\theta_x \qquad (4.16)$$

where τ_{bal} is the resulting torque due to an imbalance. For now we will simplify Eq. (4.16) by defining

$$
\begin{aligned}
A &= -L_y m_y g \\
B &= m_z g L_z
\end{aligned}
\qquad (4.17)
$$

to produce

$$\tau_{bal} = A\cos\theta + B\sin\theta. \qquad (4.18)$$

The coefficients A and B are the torque magnitudes that correspond to the imbalances in the $Y-$ and $Z-$axes, respectively. Due to the linearity of the torque characterization maneuver described in Eq. (4.14) with respect to θ, the angular acceleration $\ddot{\theta}$ is assumed to be approximately zero. Subsequently, Equation (4.18) can be integrated to approximately

$$h_{bal} \approx \frac{A}{\dot{\theta}}\sin\theta - \frac{B}{\dot{\theta}}\cos\theta + h_0 \qquad (4.19)$$

where h_{bal} is the angular momentum in the test axis as a result of an imbalance, and

h_0 is needed since the θ of zero does not correspond to t equal zero. The coefficients A, B, and h_0 can be solved for from the following equation

$$\mathbf{A} \begin{bmatrix} A & B & h_0 \end{bmatrix}^{\mathrm{T}} = h_{rw} \tag{4.20}$$

where h_{rw} is a $(m \times 1)$ matrix consisting of the angular momentum of the RW about each time-step of 0.01 seconds. The terms A, B, and h_0 are coefficients that were concatenated to form a (3×1) matrix, and $\mathbf{A}$ is a $(m \times 3)$ defined as

$$\mathbf{A} = \begin{bmatrix} \frac{\sin\theta}{\dot{\theta}} & \frac{-\cos\theta}{\dot{\theta}} & 1 \end{bmatrix}. \tag{4.21}$$

The terms $\sin\theta$, $\cos\theta$, and 1 are all $(m \times 1)$ arrays, and as previously explained in Eq (4.14), $\dot{\theta}$ is treated as a constant. Because the matrices are non-square, a pseudo-inverse is used to calculate the coefficients

$$\begin{bmatrix} A & B & h_0 \end{bmatrix}^{\mathrm{T}} = (\mathbf{A}^{\mathrm{T}}\mathbf{A})^{-1}\mathbf{A}^{\mathrm{T}}h_{rw}. \tag{4.22}$$

Once the magnitudes A and B have been calculated, we can substitute them into Eq.(4.17) to produce

$$A = m_y g L_y \tag{4.23}$$

and

$$B = m_z g L_z. \tag{4.24}$$

Equations (4.23) and (4.24) have four unknowns: m_y, L_y, m_z, and L_z. If we choose a normalization mass of 120 g, the approximate mass of our balancing system, we can normalize the solution that represents the current error in the balancing system.

Similarly, expressing the angular momentum in the inertial $Y-$axis h_y^I as

$$h_y^I = C_1 t + C_0 \qquad (4.25)$$

the torque associated with imbalance in the body $X-$axis would be equal to the time derivative of Eq. (4.25)

$$C_1 = m_x g L_x \qquad (4.26)$$

where the function resulting from Eq. (4.18) will subsequently be referred to as the torque resulting from a "simple imbalance." The residual torque τ_{res} calculated as

$$\tau_{res} = \tau^P(\theta^n) - \tau_{bal}(\theta) \qquad (4.27)$$

is the torque that cannot be eliminated by balancing efforts or estimated due to zero and first-order torques.

It is important to note that this balance estimation method is formed on the assumption that the single significant zero and first-order torques are due to imbalance. As a result, the balance estimation about a single axis may be unique to said axis and therefore a single axis imbalance estimate is referred to as the "local imbalance." This is a balance that theoretically could be obtained if we specifically tuned the spacecraft for a maneuver about a single specific axis. Conversely, the "global balance" is an adjustment of the center of mass that was chosen to reduce disturbance torques about all axes and as a result will not be as effective in eliminating disturbance torques about any given axis and will be discussed in the upcoming Subsection 4.4.4.

4.4.3 Polynomial Approximation and Angular Momentum Correction.

Due to the presence of noise, the disturbance torque is estimated as the derivative of a polynomial approximation of the angular momentum data. The polynomial approximations can then be differentiated to produce the disturbance torque estimation. A third-order torque estimation can be expressed as

$$\tau_{sc} \approx \tau^P(\theta^3) = A_3 + B_3\theta + C_3\theta^2 + D_3\theta^3. \tag{4.28}$$

Since one of the objectives is to identify the disturbance torques that cannot be corrected by balancing, we will need to correct $\tau^P(\theta^3)$ for the disturbance torque caused by an imbalance by representing $\tau^P(\theta^3)$ as the sum of the disturbance torques due to imbalance and the disturbance torques that are not caused by an imbalance from

$$\tau^P(\theta^3) = A_3 + B_3\theta + C_3\theta^2 + D_3\theta^3 = A_{bal}\cos\theta + B_{bal}\sin\theta + \tilde{A} + \tilde{B}\theta + \tilde{C}\theta^2 + \tilde{D}\theta^3. \tag{4.29}$$

Then a Taylor series expansions of the disturbance torques due to an imbalance can be formed to produce

$$\tau^P(\theta^3) = A_3 + B_3\theta + C_3\theta^2 + D_3\theta^3 \approx A_{bal} + \tilde{A} + B_{bal}\theta + \tilde{B}\theta + \tilde{C}\theta^2 - \frac{A_{bal}}{2!}\theta^2 + \tilde{D}\theta^3 - \frac{B_{bal}}{2!}\theta^3. \tag{4.30}$$

Once in this form, the coefficients of the various powers of θ can be isolated and set equal resulting in

85

$$\begin{aligned}
\tilde{A} &= A_3 - A_{bal} \\
\tilde{B} &= B_3 - B_{bal} \\
\tilde{C} &= C_3 + \tfrac{A_{bal}}{2!} \\
\tilde{D} &= D_3 + \tfrac{B_{bal}}{2!}
\end{aligned} \tag{4.31}$$

and a new simple imbalance corrected torque estimate $\tilde{\tau}(\theta^3)$

$$\tilde{\tau}^P(\theta^3) = \tilde{A} + \tilde{B}\theta + \tilde{C}\theta^2 + \tilde{D}\theta^3. \tag{4.32}$$

Once corrected, the coefficients for the estimated disturbance torque can be individually analyzed and evaluated at various deflection angles allowing for a better understanding of the tradeoff between larger maneuvers with more disturbance torques and smaller maneuvers with less disturbance torques.

4.4.4 Balance Continuum and Global Balancing.

In the previous section, we estimate the imbalance of the spacecraft by implementing a torque characterization maneuver about the $X-$axis. Since the choice of test axis is arbitrary, this process can be repeated about any axis in the $X - Y$ plane. With this in mind, the process was repeated about ten more axes $\tilde{X}$ in the $X - Y$ plane at ten degree increments of Φ, as shown in Fig. 4.5(b).

For each new test axis $\tilde{X}$, the torque characterization maneuver is repeated five times resulting in five imbalance estimations. Figures 4.6(a), 4.6(c), and 4.6(e) show the mean normalized moment arm estimations for each axis along with the maximum and minimum estimations and a ± 1 (cm) dashed line for a reference to the precision of the estimates. The histograms in Figs. 4.6(b), 4.6(d), 4.6(f) show the fifty residuals calculated by comparing the five imbalance estimates with the mean of the five imbalance estimates for the ten test axes.
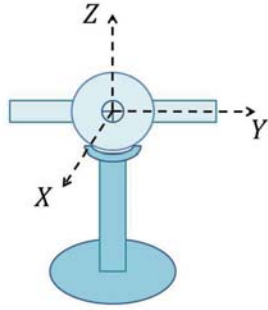
(a) Representation of Satellite Attitude Simulator
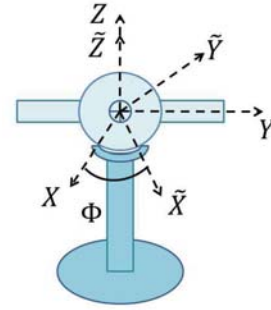
(b) Definition of Φ

Figure 4.5. Definition of Alternate Test Axes

Although Fig. 4.6(e) shows the imbalance estimate in the $Z-$axis varies significantly between test axes, Fig. 4.6(f) suggests that for a given test axis the imbalance estimate in the $Z-$axis is relatively consistent. These two observations combine to help generate the conclusion that there is an additional first-order disturbance torque that is a function of Φ and is currently not accounted for with the rigid body assumption that was used to estimate the simple imbalance. In addition, the fact that the "local imbalance" varies as a function of the test axis gave rise for the identification of the "global imbalance" the average of the fifty "local imbalances." Since one objective of this research is to reduce the disturbance torques, it is first beneficial to determine the source of the disturbance torques. In the next section, we will derive the equations for the torques associated with structural deflections to determine if they could be responsible for the additional first-order disturbance torque.

4.5 Derivation of Disturbance Torques Due to Structural Deflections

In order to model the disturbance torque associated with structural deflections, we create a depiction of SimSat as an air bearing with two masses attached by two

(a) X Imbalance Estimate vs Φ (b) Fifty X Imbalance Residuals

(c) Y Imbalance Estimate vs Φ (d) Fifty Y Imbalance Residuals

(e) Z Imbalance Estimate vs Φ (f) Fifty Z Imbalance Residuals
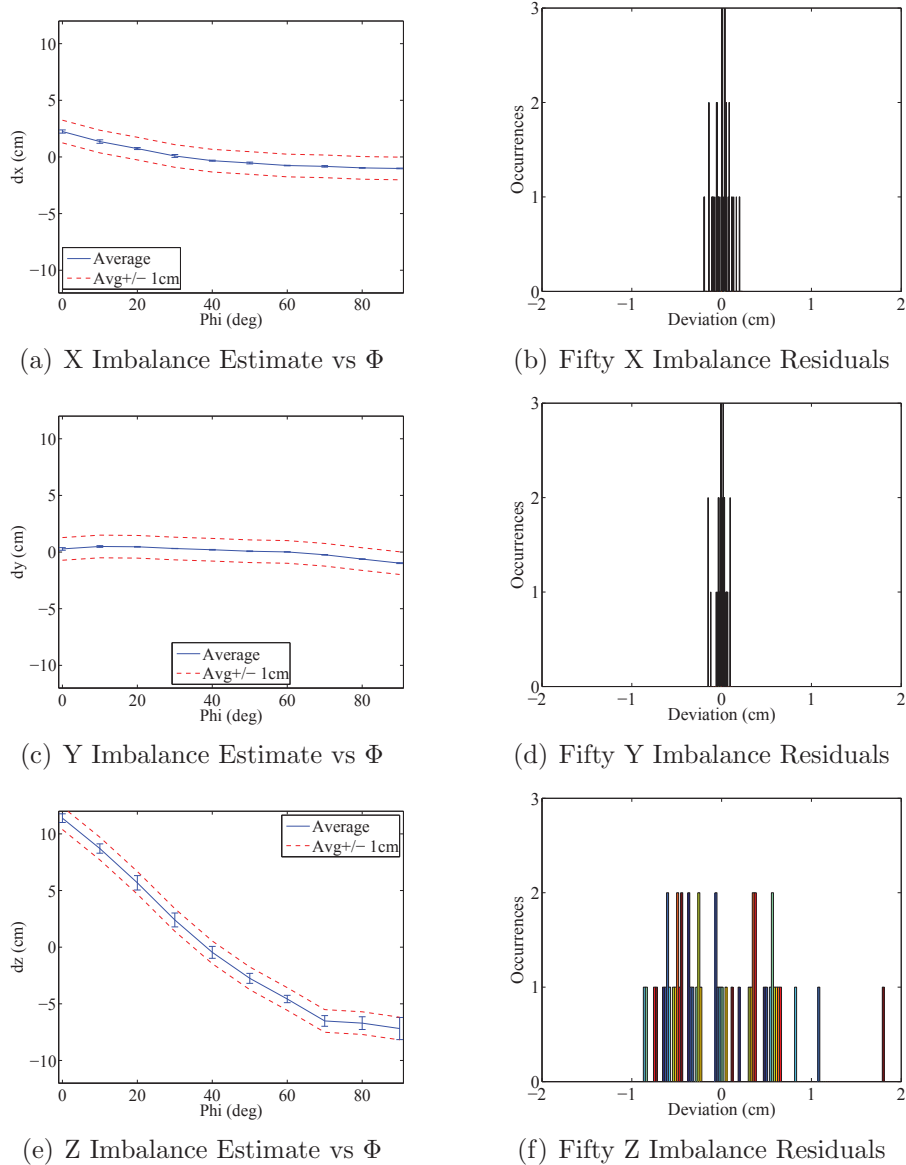
Figure 4.6. Initial Imbalance Estimates

springs as shown in Figure 4.7(a).

If the location of the masses m_1 and m_2 are such that SimSat is statically balanced, then any displacement of m_1 or m_2 in the $Y-$or $Z-$axis will result in an imbalance and the imbalance will produce a gravity torque. The magnitude of the forces from each mass in the body frame $X-$axis can be written as

$$\begin{aligned}
F_{m_1 z_f} &= -m_1 g \cos\theta \\
F_{m_2 z_f} &= -m_2 g \cos\theta \\
F_{m_1 y_f} &= -m_1 g \sin\theta \\
F_{m_2 y_f} &= -m_2 g \sin\theta.
\end{aligned} \tag{4.33}$$
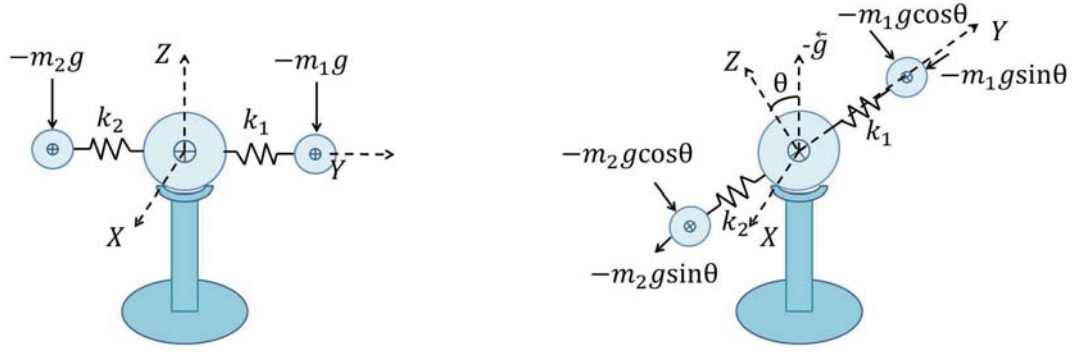
(a) Gravitational Force at Neutral Position   (b) Forces as a Function of θ

Figure 4.7. Gravitational Forces on a Flexible SimSat

Due to masses being attached by springs, a change in force will result in a change in displacement. Recall, using Hooke's law the displacement of a spring can be written as

$$x_k = \frac{f}{k}. \tag{4.34}$$

As the force changes, the displacement will change as well

$$\delta x_k = \frac{\delta f}{k} \tag{4.35}$$

where δx_k is the change in displacement of the spring and δf is the change in force. Since the springs have a mass attached to them, any change in the displacement of the spring in the body frame will result in a movement in the center of the attached

89

masses

$$
\begin{aligned}
\delta_{z1} &= \frac{-m_1 g}{k_{1z}} \cos\theta - \frac{-m_1 g}{k_{1z}} \\
\delta_{z2} &= \frac{m_2 g}{k_{2z}} \cos\theta - \frac{-m_2 g}{k_{2z}} \\
\delta_{y1} &= \frac{-m_1 g}{k_{1y}} \sin\theta - 0 \\
\delta_{y2} &= \frac{-m_2 g}{k_{2y}} \sin\theta - 0
\end{aligned}
\tag{4.36}
$$

which can be rearranged as

$$
\begin{aligned}
\delta_{z1} &= \frac{m_1 g}{k_{1z}} (1 - \cos\theta) \\
\delta_{z2} &= \frac{m_2 g}{k_{2z}} (1 - \cos\theta) \\
\delta_{y1} &= \frac{-m_1 g}{k_{1y}} \sin\theta \\
\delta_{y2} &= \frac{-m_2 g}{k_{2y}} \sin\theta.
\end{aligned}
\tag{4.37}
$$

The movement of the two masses, both in the body frame $Y-$ and $Z-$axes will create an imbalance resulting in a torque about the $X-$axis as a function of the rotation angle

$$
\begin{aligned}
\tau_{\delta_z} &= \delta_{z_1} m_1 g \sin\theta + \delta_{z_2} m_2 g \sin\theta \\
\tau_{\delta_y} &= -\delta_{y_1} m_1 g \cos\theta - \delta_{y_2} m_2 g \cos\theta.
\end{aligned}
\tag{4.38}
$$

Substituting Eqs. (4.37) into Eqs. (4.38) results in

$$
\begin{aligned}
\tau_{\delta_z} &= \left(\frac{m_1^2 g^2}{k_{1z}} + \frac{m_2^2 g^2}{k_{2z}} \right) (1 - \cos\theta) \sin\theta \\
\tau_{\delta_y} &= \left(\frac{m_1^2 g^2}{k_{1y}} + \frac{m_2^2 g^2}{k_{2y}} \right) \sin\theta \cos\theta.
\end{aligned}
\tag{4.39}
$$

By defining coefficients of structural deflections in the $Y-$ and $Z-$axes, C_V and C_H are defined as follows

$$C_V = \left(\frac{m_1^2 g^2}{k_{1z}} + \frac{m_2^2 g^2}{k_{2z}} \right)$$
$$C_H = \left(\frac{m_1^2 g^2}{k_{1y}} + \frac{m_2^2 g^2}{k_{2y}} \right) \tag{4.40}$$

then the equations reduce to the following

$$\tau_{\delta_z} = C_V (1 - \cos\theta) \sin\theta$$
$$\tau_{\delta_y} = C_H \sin\theta \cos\theta. \tag{4.41}$$

It is important to note, that similar to the torque characterization maneuver where the choice of $\tilde{X}$ could be arbitrarily chosen, the choice of deriving the previous equations about the $X-$axis was also arbitrary. Were we to repeat the process about the $Y-$axis, or any of the axes in-between, we would expect to have different masses and different spring constants. As a result, it is safe to assume that C_V and C_H, as derived, are functions of the test axis and are therefore a function of Φ. As a result, we express them as such $C_V(\Phi)$ and $C_H(\Phi)$. Substituting $C_V(\Phi)$ and $C_H(\Phi)$ into Eq. (4.39) and Taylor series expanding out to terms of θ^3 produces

$$\tau_{\delta_z} \approx \frac{C_V(\Phi)}{2!} \theta^3$$
$$\tau_{\delta_y} \approx C_H(\Phi)\theta - \frac{C_H(\Phi)}{2!} \theta^3. \tag{4.42}$$

The disturbance torques from Eq. (4.41) due to structural deflections can then be added to the summation of torques due to imbalance to generate

91

$$\dot{h} = -L_y m_y g \cos\theta + L_z m_z g \sin\theta + C_V(\Phi)(1 - \cos\theta)\sin\theta + C_H(\Phi)\sin\theta\cos\theta. \quad (4.43)$$

After taking a Taylor series expansion about θ set to zero, we get an expression of $\dot{h}$ as

$$\dot{h} = -L_y m_y g + (L_z m_z g + C_H(\Phi))\delta\theta + \frac{L_y m_y g \delta\theta^2}{2!} + \frac{(C_V(\Phi) - C_H(\Phi))\delta\theta^3}{2!} + \text{H.O.T.}$$

$$(4.44)$$

In this form, it is clear to see that there are now two first-order terms with respect to $\delta\theta$ and that assuming $C_H(\Phi)$ is zero could result in the erroneous conclusion that the simple imbalance $L_z m_z$ changed as a function of the rotation axis Φ. Although the dominant term in the Taylor series expansion for $L_z m_z$ and $C_H(\Phi)$ is a first-order torque, continuing the Taylor series expansion to a higher-order would result in a third-order torque which would result in a fourth-order component in the angular momentum while introducing another unknown $C_H(\Phi)$. Even if we assumed that $C_H(\Phi)$ was zero, recall Fig. 4.8(c) that showed the residual between the fourth-order polynomial estimation of h_{rw} and the measured values of h_{rw}. From Fig. 4.8(b) it would appear as if the residual for the fourth-order polynomial estimation was already on the order of the sensor noise. The residual in Fig. 4.8(c) would suggest that any attempt to use fourth-order angular momentum data to differentiate between two first-order torques would result in estimates that are highly susceptible to errors associated with sensor noise. Although this methodology was attempted, the suspicions were confirmed when deviations in estimates of $L_z m_z$ increased by over an order of magnitude. As a result, instead of solving for the amount of structural flexing, we decided to decrease the amount of structural flexing by adding structural reinforcements to key components of SimSat.

4.5.1 Original Torque Characterization Results.

From the fifty torque characterization maneuvers implemented in Sec. 4.4.4 to identify the change in first-order torque and estimate the "global imbalance", a single maneuver about the $X-$axis was selected for additional analysis. The results from the additional analysis are shown in Fig. 4.8.
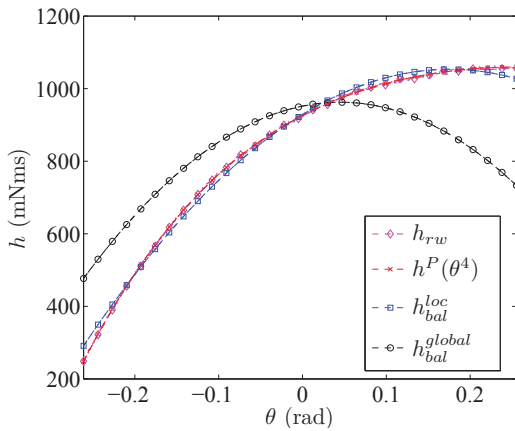
(a) Angular Momentum of Reaction Wheels, 4th-Order Momentum Estimates, and Balance Estimates vs θ
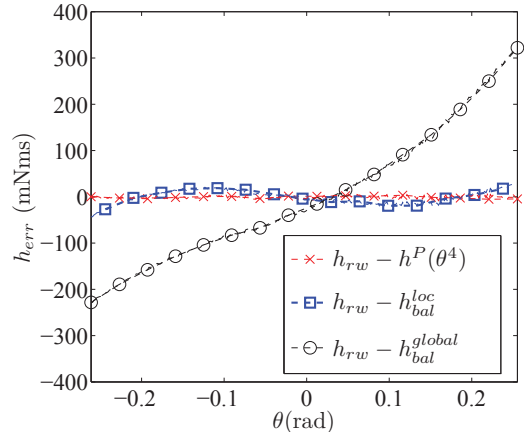
(b) Difference between h_{rw} and 4-Order Polynomial and Simulated Imbalance
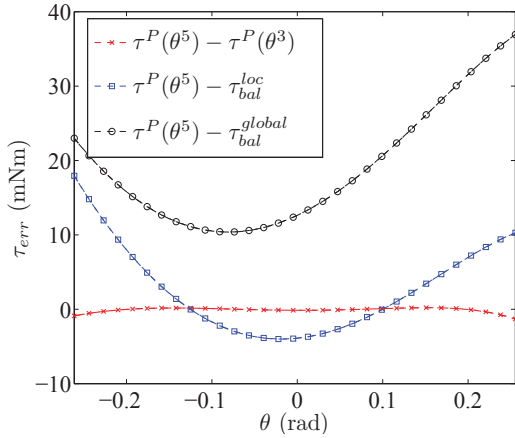
(c) Residual Torques Between $\tau^P(\theta^5)$ and $\tau^P(\theta^3)$ and Simulated Imbalance
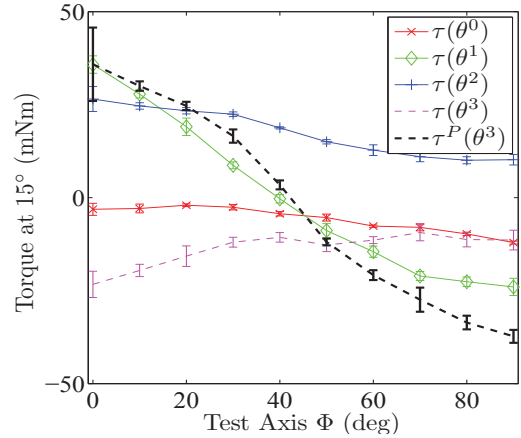
(d) Magnitudes of Various Order Torques Evaluated at 15° Rotation about Various Test Axes Φ

Figure 4.8. Initial Results from Torque Characterization Maneuver

Figure 4.8(a) shows the angular momentum of the RW in the test axis h_{rw} which

is not constant clearly showing the presence of a disturbance torque. A fourth-order polynomial approximation $h^P(\theta^4)$ which will be differentiated to $\tau^P(\theta^3)$ and used to analyze the disturbance torques. Additionally, Fig. 4.8(a) shows the angular momentum curve associated with the local balance h_{bal}^{loc} as well as the angular momentum curve that would result from the global imbalance h_{bal}^{global}. It is important to note that there is a significant disagreement between the angular momentum resulting from the global imbalance h_{bal}^{global} and the angular momentum of the spacecraft h_{rw}, this further suggests that there are significant disturbance torques other than the disturbance torques due to an imbalance. Figure 4.8(b) shows the residuals between the h_{rw} and a fourth-order polynomial approximation of $h_{rw}^P(\theta^4)$ as well as the angular momentum resulting from a local imbalance simple imbalance h_{bal}^{loc} and a global imbalance h_{bal}^{global}. Once again the curve is dominated by the residual error between the angular momentum of the spacecraft h_{rw} and the angular momentum that would result from the global imbalance. Figure 4.8(c) shows the residual between "truth" $\tau^P(\theta^5)$ and $\tau^P(\theta^3)$ and the torques resulting from a local imbalance τ_{bal}^{loc} and a global imbalance. Although the previous figures shows the globally balanced results greatly overshadowing the disturbance torques due to a local balance, Fig. 4.8(c) shows that a lot of that is due to the least-squares estimate selecting a local imbalance that integrates out to almost zero. The instantaneous torque at θ of 15° is approximately 20 mNm, when compared to the available torque from a single reaction wheel of 250 mNm we conclude that even if we balanced to a specific axis the disturbance torques at 15° would account for almost 8% of our available torque. In Figure 4.8(d) we have taken a slightly different approach and instead of showing the torque over a single maneuver, we have reduced each maneuver into a single torque about 15° deflection. This single torque is then separated into a sum of the first four components of the Taylor series expansion evaluated at 15°, resulting in a single torque value for each

of the evaluated terms $\tau(\theta^0)$ to $\tau(\theta^3)$. These four torque components were calculated for all five maneuvers about a given test axis and the average value of each of the four torque components was calculated. The process was repeated about all ten test axes and the results of the individual torque components are plotted against the test axis Φ. Table 4.1 shows the largest respective torque components of all ten test axes so the "Total" torque value will not necessarily be a summation of the four torque components.

The data in Table 4.1 shows that the dominant torque is indeed the first-order disturbance torque. As derived in Sec. 4.5, this could be due to structural flexing. As a result, structural reinforcements were added to key components and the experiment was repeated.

4.6   Structural Reinforcements

In 2008, SimSat was reconfigured from a dumbbell to a tabletop configuration with the desire to increase the rigidity and decrease the structural flexing [30]. In 2011, McChesney designed, built, and installed a four CMG array on the surface [25]. To counteract the movement of the center of gravity in the body $Z-$axis, large steel ballasts were added to the bottom of SimSat as shown in Fig. 4.9. After the reinforcements were added, the torque characterization experiment described in Sec. 4.4 was repeated and the results are shown in Fig. 4.10.

Figures 4.10(a) and 4.10(b) shows the angular momentum and residuals of the RW

Table 4.1. Original Disturbance Torques

Order of Torque $\delta\theta$	15°	10°	5°	Std Dev at 15°
Zeroth	12.08	12.08	12.08	0.76
First	35.79	23.86	11.93	1.61
Second	26.52	11.79	2.95	1.17
Third	23.31	6.91	0.86	2.01
Total	37.29	26.93	19.37	2.43
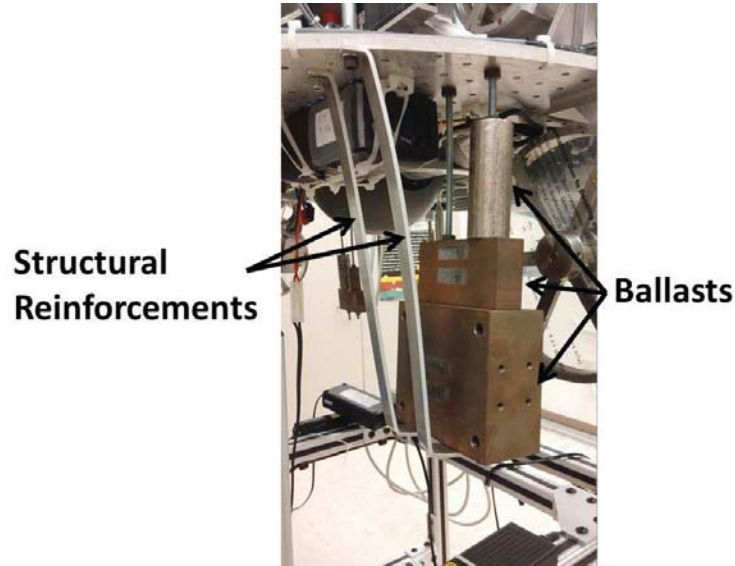
Figure 4.9. Braces Added to Increase Rigidity of Ballasts

for a single maneuver about the $X-$axis along with a fourth-order polynomial approximation $h^P(\theta^4)$, angular momentum that would result from balancing locally, and the angular momentum that would result from balancing globally. Similar to the results from prior to the structural reinforcements, the angular momentum that would result from balancing globally still clearly disagrees with the experimental data confirming the presence of disturbance torques that cannot be accounted for by balancing the spacecraft as a whole. Figure 4.10(c) still shows the disturbance torque associated with the local imbalance associated with balancing globally as the dominant disturbance torque, but unlike before the structural reinforcements were added the torque that could result from balancing specifically for the test axis has been significantly reduced from approximately 15 mNm shown in Fig. 4.8(c) to approximately 3 mNm as shown in Fig. 4.10(c).

Figure 4.10(d) shows the corrected coefficients of the third-order torque approximation and once again even though the coefficients vary widely as a function of the test axis Φ, they are consistent which suggests that they can be characterized and
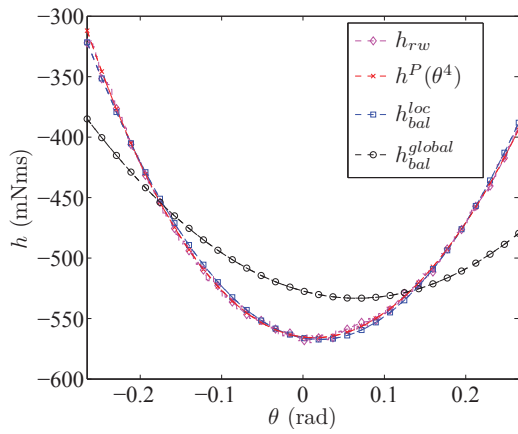
(a) Angular Momentum of Reaction Wheels, 4th-Order Momentum Estimates, and Balance Estimates vs θ
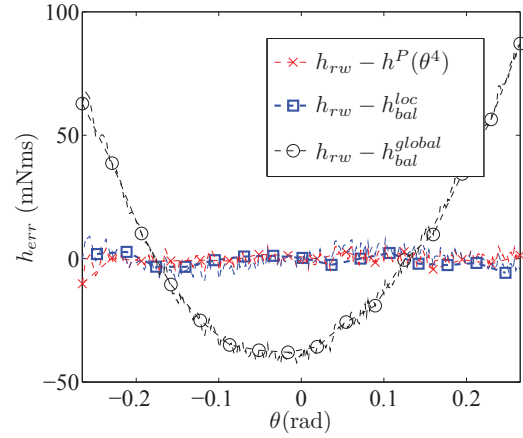
(b) Difference between h_{rw} and 4-Order Polynomial and Simulated Imbalance
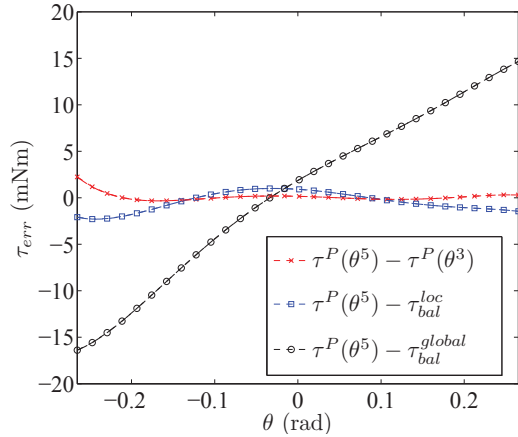
(c) Residual Torques Between $\tau^P(\theta^5)$ and $\tau^P(\theta^3)$ and Simulated Imbalance
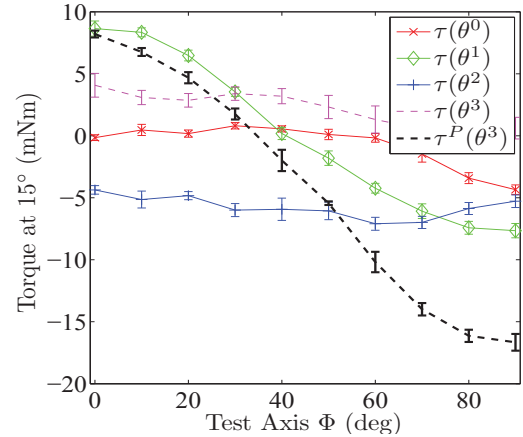
(d) Magnitudes of Various Order Torques Evaluated at 15° Rotation about Various Test Axes Φ

Figure 4.10. Torque Characterization Maneuver after Structural Reinforcements

actively corrected.

Table 4.2 shows the disturbance torques of the varying orders evaluated at three angles. Once again the first-order disturbance torque at 15° but the structural reinforcements seem to have greatly reduced the impact of the disturbance torques. Table 4.3 shows a side-by-side comparison of the disturbance torques before and after the addition of the structural reinforcements.

Table 4.2. Disturbance Torques After Structural Reinforcement

Order of Torque $\delta\theta$	15°	10°	5°	Std Dev at 15°
Zeroth	4.35	4.35	4.35	0.37
First	8.65	5.77	2.88	0.49
Second	7.10	3.15	0.79	0.55
Third	4.08	1.21	0.15	0.80
Total	16.66	11.61	7.46	0.50

Table 4.3. Comparison of Structural Deflections Before and After Structural Reinforcement

Order of Torque $\delta\theta$	Pre Reinforcement Torque Evaluated at 15° (mNm)	Post Reinforcement Torque Evaluated at 15° (mNm)	Percent Reduction %
Zeroth	12.08	4.35	64.0%
First	35.79	8.65	75.8%
Second	26.52	7.10	73.2%
Third	23.31	4.08	82.5%
Total	37.29	16.66	55.3%

From Table 4.3 we see that the structural reinforcements have decreased the first and third-order torques by over 75% and 82% respectively. Interestingly, even though the structural deflection as derived generated a first- and third-order disturbance torque, the zeroth- and second-order torques also saw significant reductions. We suspect that this is due to non-collinear deflections. The disturbance torques as derived in Section 4.5 were based on the principal structural axes being collinear with the body frame axes. This assumption meant that a force in the $Y-$axis would only produce a collinear deflection in the $Y-$axis. In actuality, it is possible that the principal structural axes are not aligned with the body axes, which could result in non-collinear deflections in the $X-$ and $Z-$axes. The second-order torque could be explained by a first-order deflection in the $Z-$axis as a result of the first-order force in the $Y-$axis.

Due to the desire to further reduce the disturbance torques, linear actuators with tip masses were added to actively counteract the imbalance associated with structural flexing, which will we discuss next.

4.7 Addition of Linear Actuators for Disturbance Torque Correction

The first step to further reduce the disturbance torque due to structural deflection, is to size the linear actuators to be added to SimSat. From Sec. 4.6, there is a 8.65 mNm torque at 15°. To counteract this torque with a linearly actuated mass, we would need 176.35 gcm of actuation in the plane perpendicular to the gravity vector. We chose an array of three Firgelli L12-100-100-12 actuators which will be commanded with three of the 0-4.5 V analog signal outputs from the dSPACE MicroAutoBox™. The L12-100-100-12 uses an on-board potentiometer and closed-loop controller to track the desired position. Due to the on-board noise filter, the linear actuators will reject small changes in position and will implement the corresponding ramp as a series of approximately 0.5 cm steps. With a 0-4.5 V signal, the actuators have a range of motion of ±4.5 cm. Correcting for 176.35 gcm imbalance at 30° deflection would require masses of approximately 40 g. We added a margin of 1.5, and constructed the actuators to have a mass of approximately 60 g. The $X-$ and $Y-$axes actuators are shown in Fig. 4.11. Due to the success of the addition of the structural reinforcements, we decided decrease the deflection by minimizing the ballast weight. The ballast mass was reduced by approximately 30% which from Eq. 4.39 should result in approximately 50% decrease in structural deflection. As a result, we decided that the disturbance torque profile would be re-characterized while the actuators were disabled to ensure that any benefits from enabling the actuators are correctly attributed to the actuation and not the configuration change. The results from the torque characterization experiment are shown in Fig. 4.12.

Figures 4.12(a) and 4.12(b) show a significant reduction in the error due to balancing globally as opposed to balancing specifically for the test axis or "locally". Additionally, Fig. 4.12(c) shows all three torques to be within 2 mNm of the estimated torque that the spacecraft experiences; results that are almost too good to be
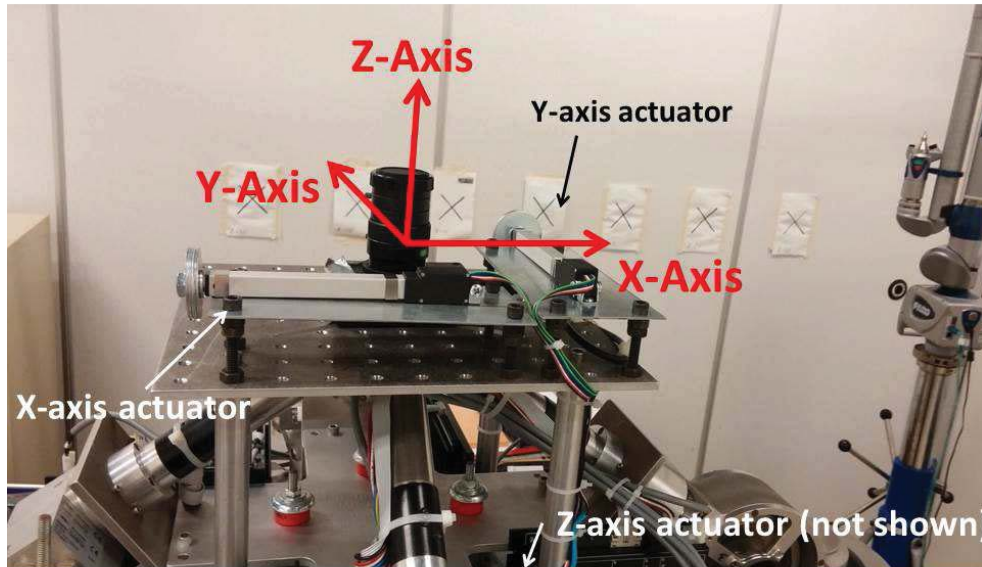
Figure 4.11. Actuators Added to Actively Compensate for Structural Flexture

true; however, Fig. 4.12(d) confirms the results but shows that the torque error about the $X-$axis is somewhat of an anomaly and suggests that if the process was repeated about the $Y-$axis we would expect considerably more torque error.

Table 4.4. Torque Analysis with Actuators Installed but Disabled

Order of Torque $\delta\theta$	15°	10°	5°	Std Dev at 15°
Zeroth	0.65	0.65	0.65	0.22
First	3.43	2.29	1.14	0.63
Second	2.03	0.90	0.23	0.40
Third	3.74	1.11	0.14	1.01
Total	5.02	2.92	1.68	0.65

Now that the disturbance torques have been characterized, the experiment will be repeated with the actuators enabled but first the actuators need to be calibrated and the structural deflection needs to be estimated.
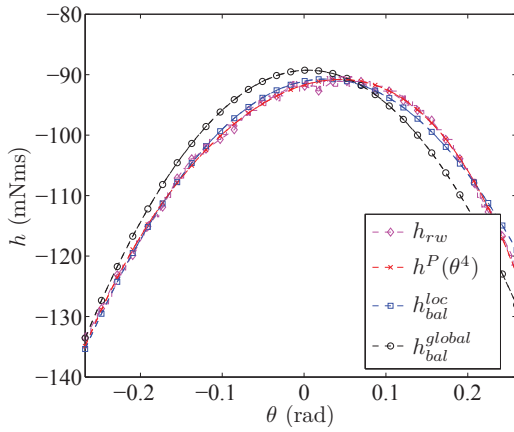
(a) Angular Momentum of Reaction Wheels, 4$^{\text{th}}$-Order Momentum Estimates, and Balance Estimates vs θ
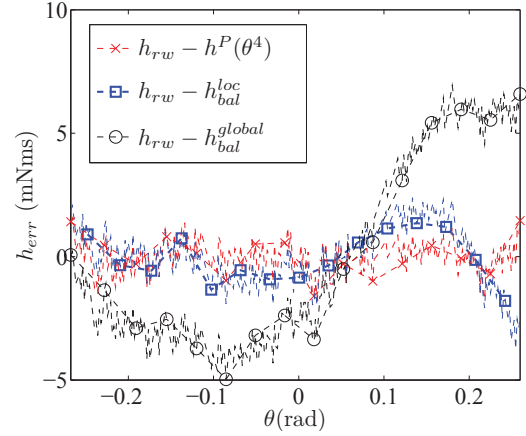
(b) Difference between h_{rw} and 4-Order Polynomial and Simulated Imbalance
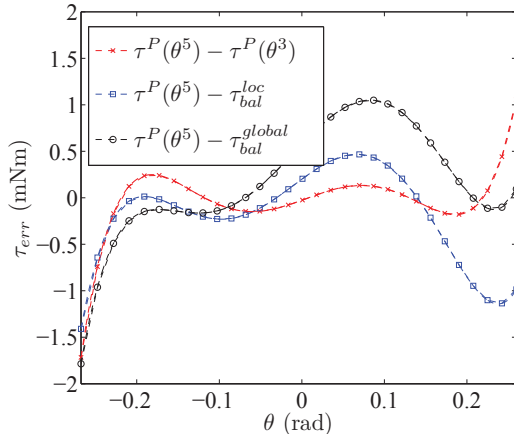
(c) Residual Torques Between $\tau^P(\theta^5)$ and $\tau^P(\theta^3)$ and Simulated Imbalance
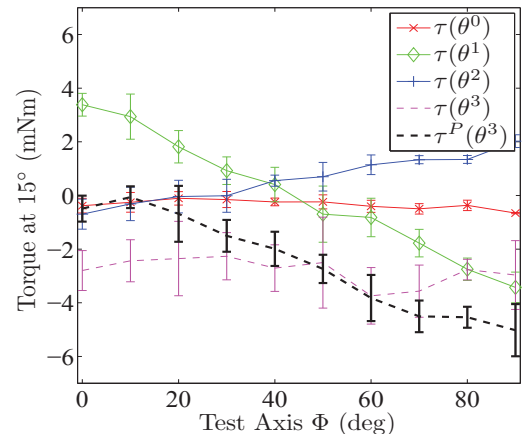
(d) Magnitudes of Various Order Torques Evaluated at 15° Rotation about Various Test Axes Φ

Figure 4.12. Torque Characterization Maneuver after Installation of Actuators

4.8 Development of an Active Balancing System

In Fig. 4.12(d), it is shown that the first-order torque estimates are changing as a result of the rotation axis Φ.

In order to negate the effects of the structural flexing that are generating a first-order disturbance torque, an active balancing system is proposed to actively move weights to correct for the dynamic imbalance as a result of structural deflections

101

by re-balancing the satellite attitude simulator as it rotates about different axes. Before implementing an active dynamic balancing system, we need to know how the spacecraft is flexing.

4.8.1 Active Imbalance Estimation.

We desire a control equation in the form of

$$\delta m = k^{-1} \begin{bmatrix} \theta_x \\ \theta_y \\ \theta_x^3 \\ \theta_y^3 \end{bmatrix}$$
(4.45)

In this form, k^{-1} is a (3x4) matrix that should be able to account for first-, second-, and third-order disturbance torques. The following equation shows k^{-1} matrix with the components of the matrix replaced with the order of the torque they are able to correct for

$$k^{-1} = \begin{bmatrix} \tau(\theta) & \tau(\theta) & 0 & \tau(\theta^3) \\ \tau(\theta) & \tau(\theta) & \tau(\theta^3) & 0 \\ \tau(\theta^2) & \tau(\theta^2) & 0 & 0 \end{bmatrix}.$$
(4.46)

Although the third-order torques could also be induced by implementing a second-order actuation in the $Z-$axis as opposed to a third-order actuation in the $X - Y$-plane, we chose the latter method over the former as it would require less actuation.

From the data shown in Fig. 4.12(d) the values of $k^{-1}(2, 1)$ and $k^{-1}(2, 2)$ can be solved with the first-order disturbance torque. We will start by identifying the components if the graph that will be used to identify the inverse stiffness matrix

$$\tau_{12} = \tau(\theta, \Phi)|_{\theta=\frac{\pi}{12}}|_{\Phi=0}$$
$$\tau_{21} = \tau(\theta, \Phi)|_{\theta=\frac{\pi}{12}}|_{\Phi=\frac{\pi}{2}}$$

(4.47)

$\tau(\theta, \Phi)|_{\theta=\frac{\pi}{12}}|_{\Phi=0}$ are the values of the first-order torque curve $\tau(\theta^2)$ shown in Fig. 4.12(d)

at Φ equal to 0. Alternatively, $\tau(\theta, \Phi)|_{\theta=\frac{\pi}{12}}|_{\Phi=0}$ is the first-order torque at Φ of 90°.

The values τ_{12} and τ_{21} are torques that will be used to calculate $k^{-1}(1, 2)$ and $k^{-1}(2, 1)$,

respectively

$$k^{-1}(1, 2) = \frac{\tau_{12}}{\sin\left(\frac{\pi}{12}\right)g}$$
$$k^{-1}(2, 1) = \frac{-\tau_{21}}{\sin\left(\frac{\pi}{12}\right)g}.$$

(4.48)

Similarly, $k^{-1}(3, 1)$ and $k^{-1}(3, 2)$ can also be calculated from the test results shown

in Fig. 4.12(d)

$$\tau_{31} = \tau(\theta^2, \Phi)|_{\theta=\frac{\pi}{12}}|_{\Phi=0}$$
$$\tau_{32} = \tau(\theta^2, \Phi)|_{\theta=\frac{\pi}{12}}|_{\Phi=\frac{\pi}{2}}$$

(4.49)

where this time $\tau(\theta^2, \Phi)|_{\theta=\frac{\pi}{12}}|_{\Phi=0}$ and $\tau(\theta^2, \Phi)|_{\theta=\frac{\pi}{12}}|_{\Phi=\frac{\pi}{2}}$ are the torque values of the

second-order torque curve $\tau(\theta^2)$

$$k^{-1}(3, 1) = \frac{\tau_{31}}{\sin^2\left(\frac{\pi}{12}\right)g}$$
$$k^{-1}(3, 2) = \frac{\tau_{32}}{\sin^2\left(\frac{\pi}{12}\right)g}$$

(4.50)

Finally $k^{-1}(2, 3)$ and $k^{-1}(1, 4)$ can be calculated from the third-order torque curve

$\tau(\theta^3)$

$$\tau_{14} = \tau(\theta^3, \Phi)|_{\theta=\frac{\pi}{12}}|_{\Phi=0}$$
$$\tau_{23} = \tau(\theta^3, \Phi)|_{\theta=\frac{\pi}{12}}|_{\Phi=\frac{\pi}{2}}$$

(4.51)

substituting τ_{14} and τ_{23} into the equation for $k^{-1}(1, 4)$ and $k^{-1}(2, 3)$

$$k^{-1}(1,4) = \frac{\tau_{14}}{\sin^3\left(\frac{\pi}{12}\right)\mathrm{g}}$$
$$k^{-1}(2,3) = \frac{-\tau_{23}}{\sin^3\left(\frac{\pi}{12}\right)\mathrm{g}} \tag{4.52}$$

Now the only terms remaining to estimate are $k^{-1}(1,1)$ and $k^{-1}(2,2)$ and they cannot be estimated from the data provided in Fig. 4.12(d). As a result, we implemented five static balance estimates at five displacements in the $X-$ and $Y-$axes and estimated the imbalance in the rotation axis. We plotted the results of the imbalance estimates against the rotation θ in Fig. 4.13, the two linear best fits were calculated and set equal to $k^{-1}(1,1)$ and $k^{-1}(2,2)$.
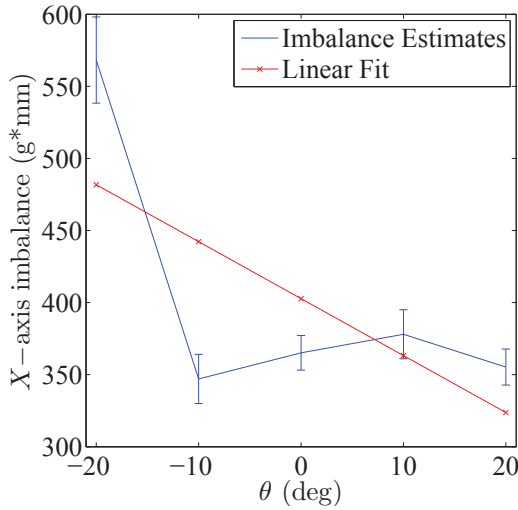
(a) Angular Momentum of Reaction Wheels vs Time
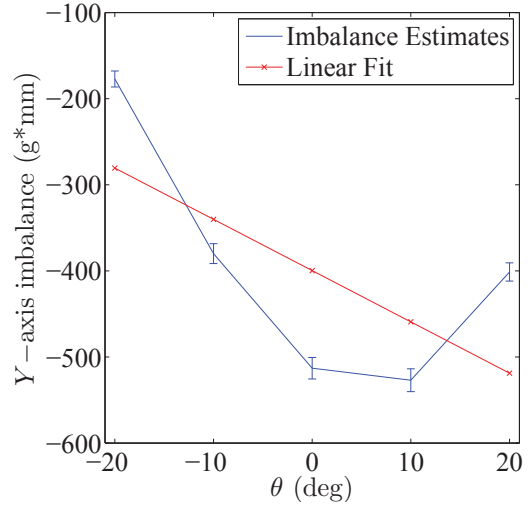
(b) Difference Between h_{rw} for 6-Order Polynomial and Simulated Imbalance

Figure 4.13. Estimation of $k^{-1}(1,1)$ and $k^{-1}(2,2)$

Now that we have solved for all of the desired components we can define k^{-1} as

$$k^{-1} = \begin{bmatrix} -226 & -1335 & 0 & -16848 \\ -1317 & -341 & 15891 & 0 \\ -1634 & 3253 & 0 & 0 \end{bmatrix} \frac{\mathrm{g\,mm}}{\mathrm{rad}}. \tag{4.53}$$

Furthermore, the standard deviation from the original components that were used

104

to estimate k^{-1} can also be substituted into the previous equations to give us an understanding of the uncertainty in the k^{-1} matrix

$$\sigma_{k^{-1}} = \begin{bmatrix} 151 & 222 & 0 & 7288 \\ 165 & 118 & 4228 & 0 \\ 832 & 351 & 0 & 0 \end{bmatrix} \frac{\text{g mm}}{\text{rad}} \tag{4.54}$$

Now that we know how our mass is moving with respect to the rotation axis, we needed to calibrate the linear actuators so we can counteract the estimated imbalance.

4.9 Calibration of the linear actuators

In order to calibrate the linear actuators, the actuators were set to 20 mm increments between ± 40 mm. Once the actuators were in position, five torque characterization maneuvers were executed about both the $X-$ and $Y-$axes and the estimated local imbalances were calculated for all of the maneuvers. It is important to note that the $X-$actuator was installed in the negative $X-$direction which means that a command signal of -45 mm is fully extended and a signal of 45 mm is fully retracted.

The results from the fifty runs per actuator were linearly interpolated and resulted in the following control Jacobian

$$M = \begin{bmatrix} 62.33 & -1.84 & 1.39 \\ 0.44 & 63.59 & -0.46 \\ -16.28 & -2.91 & 60.03 \end{bmatrix} \frac{\text{g mm}}{\text{mm}}. \tag{4.55}$$

Once the control Jacobian was defined we can calculate the movement of the masses as a result of a given command signal

(a) X imbalance from X Actuator

(b) Y imbalance from X Actuator

(c) Z imbalance from X Actuator

(d) X imbalance from Y Actuator

(e) Y imbalance from Y Actuator

(f) Z imbalance from Y Actuator

(g) X imbalance from Z Actuator

(h) Y imbalance from Z Actuator

(i) Z imbalance from Z Actuator
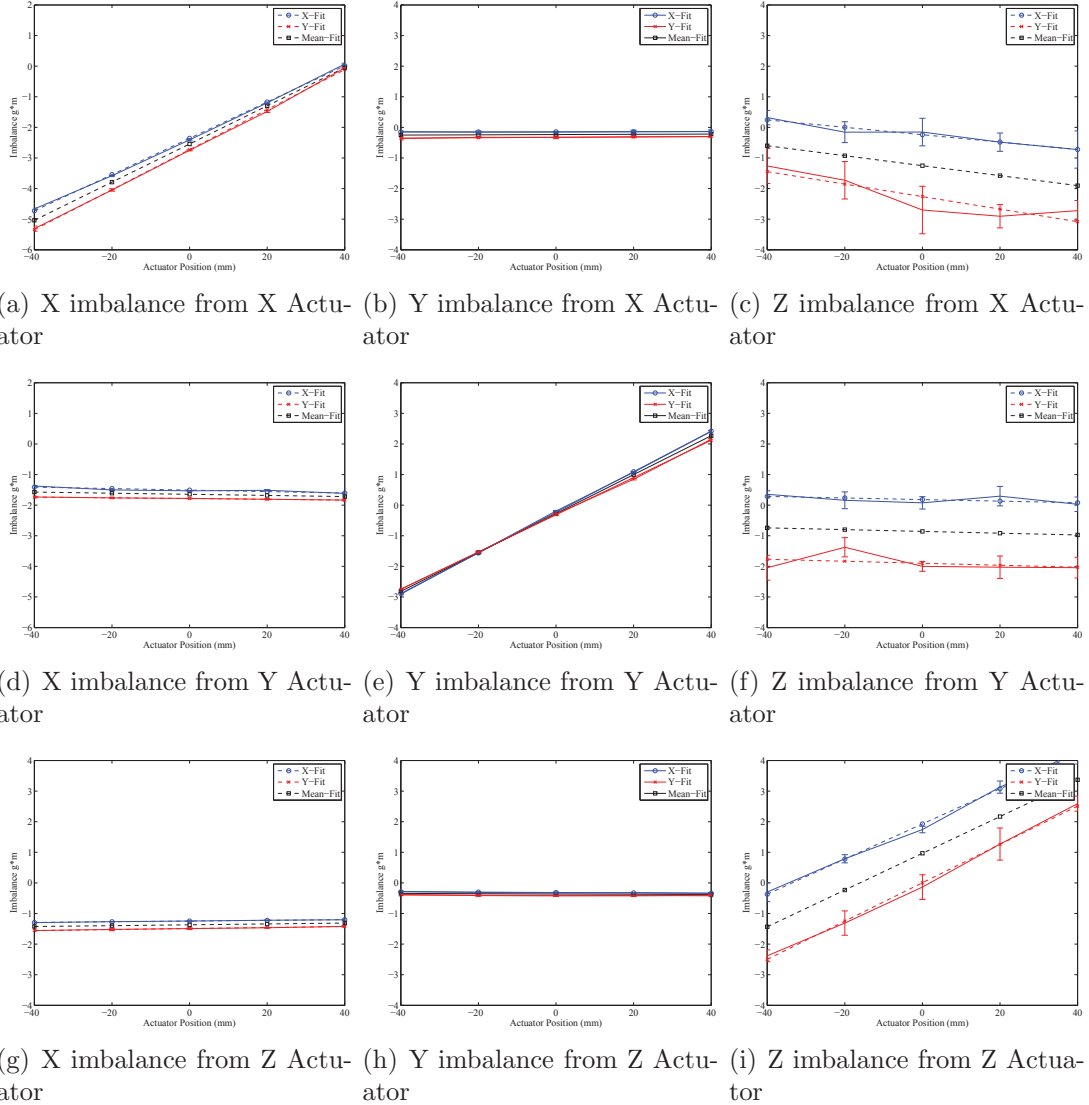
Figure 4.14. Imbalance Estimates as a Function of Commanded Actuator Positions

$$\delta m_{act} = M \begin{bmatrix} dm_x \\ dm_y \\ dm_z \end{bmatrix} \tag{4.56}$$

and the command signal can be calculated by inverting the control Jacobian and multiplying it by the desired change in mass.

$$\delta m_{act} = -k^{-1} \begin{bmatrix} \theta_x \\ \theta_y \\ \theta_x^3 \\ \theta_y^3 \end{bmatrix} \tag{4.57}$$

and then we set

$$M \begin{bmatrix} dm_x \\ dm_y \\ dm_z \end{bmatrix} = -k^{-1} \begin{bmatrix} \theta_x \\ \theta_y \\ \theta_x^3 \\ \theta_y^3 \end{bmatrix} \tag{4.58}$$

so that a simple inversion of the M matrix results in the desired actuator command signal

$$\begin{bmatrix} dm_x \\ dm_y \\ dm_z \end{bmatrix} = -M^{-1}k^{-1} \begin{bmatrix} \theta_x \\ \theta_y \\ \theta_x^3 \\ \theta_y^3 \end{bmatrix} \tag{4.59}$$

Now that the actuators have been installed, calibrated, and enabled, the torque characterization process was repeated and the results are shown in Fig. 4.15. It is clear from Figs. 4.15(a), 4.15(b), and 4.15(c) that there is still a slight disagreement between the local balance and the global balance resulting in approximately 2 mNm torque. Figure 4.15(d) shows that the torque curves have become more constant with respect to Φ and the maximum torque evaluated at 15° has now been reduced to approximately 3 mNm. The results from Fig. 4.15(d) have been evaluated at multiple deflections and the resulting torques are shown in Tab. 4.5.

Table 4.6 shows a side by side comparison of the disturbance torques evaluated
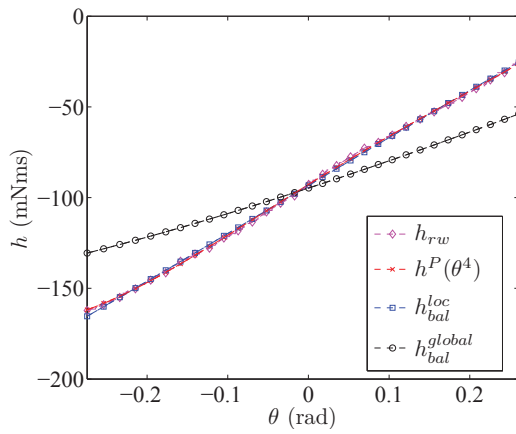
(a) Angular Momentum of Reaction Wheels, 4th-Order Momentum Estimates, and Balance Estimates vs θ
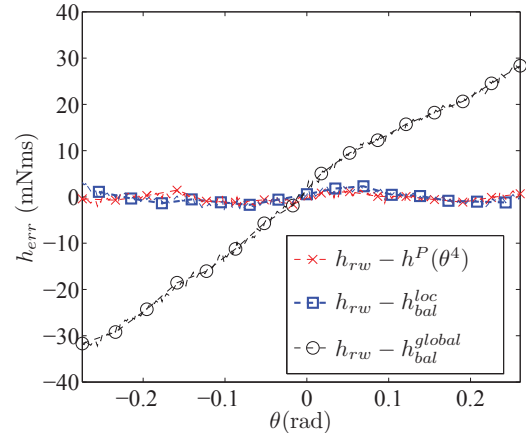
(b) Difference between h_{rw} and 4-Order Polynomial and Simulated Imbalance
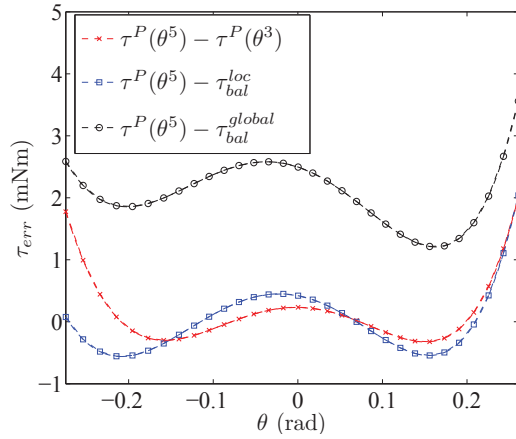
(c) Residual Torques Between $\tau^P(\theta^5)$ and $\tau^P(\theta^3)$ and Simulated Imbalance
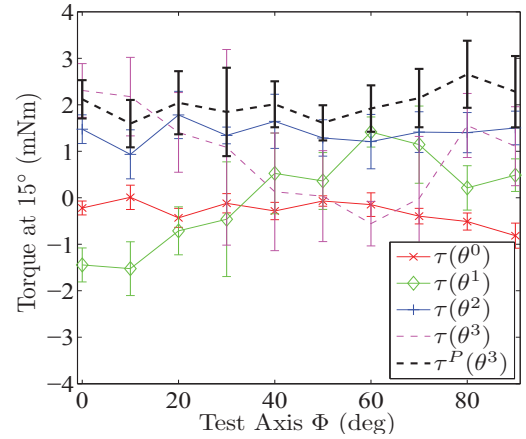
(d) Magnitudes of Various Order Torques Evaluated at 15° Rotation about Various Test Axes Φ

Figure 4.15. Torque Characterization Maneuver with Actuators Enabled

Table 4.5. Torque Analysis with Actuators Enabled

Order of Torque $\delta\theta$	15°	10°	5°	Std Dev at 15°
Zeroth	0.82	0.82	0.82	0.20
First	1.52	1.10	0.51	0.62
Second	1.78	0.79	0.20	0.43
Third	2.31	0.68	0.09	1.00
Total	2.66	1.17	0.45	0.60

at 15° both before and after the linear actuators were installed. This data shows a slight increase in the zero-order torque, but a significant decrease in the first-order torque, for an overall torque decrease of 47%.

Table 4.7 also compares the disturbance torques with and without the actuators enabled, but this time it evaluates the torques at θ of 5°. Once again there is a slight increase in the zeroth-order component, and a 55% decrease in the second-order torque but with the actuators enabled the disturbance torque varies less as a function of Φ so when we compare the maximum torques from both cases, the actuators were able to reduce the maximum expected disturbance torque by 73.2%.

4.10   Conclusion

In this chapter we experimentally identified and then developed and analyzed a method to actively correct for gravitational disturbance torques. This chapter started by presenting a torque characterization maneuver that confirmed the invalidity of the rigid body assumption on AFIT's satellite simulator called SimSat. We identified a second significant first-order disturbance torque which accounted for 14% of the available torque at a rotation of 15° about an axis in the $X - Y$ plane. Upon evaluating the potential sources of disturbance torques, we hypothesized that the disturbance torque was due to structural deflection and added structural reinforcements and reduced the ballast mass to decrease structural deflection. The torque characterization

Table 4.6. Comparison of Torques evaluated at at 15° **with Actuators Disabled and Actuators Enabled**

Order of Torque $\delta\theta$	Actuators Disabled	Actuators Enabled	Percent Difference %
Zeroth	0.65	0.82	-26.2%
First	3.43	1.52	55.7%
Second	2.03	1.78	12.3%
Third	3.74	2.31	38.2%
Total	5.02	2.66	47.0%

Table 4.7. **Comparison of Torques evaluated at at** $5°$ **with Actuators Disabled and Actuators Enabled**

Order of Torque $\delta\theta$	Actuators Disabled	Actuators Enabled	Percent Difference %
Zeroth	0.65	0.82	-26.2
First	1.14	0.51	55.3
Second	0.23	0.20	13.0
Third	0.14	0.09	35.7
Total	1.68	0.45	73.2

process was repeated, with a 91% decrease in first-order disturbance torques and a 87% decrease in all torques when evaluated at 15° rotation about a test axis in the $X - Y$ plane. In order to further decrease the disturbance torques, we added three linear torque actuators to actively counteract the disturbance torques which resulted in an additional 55.7% decrease in first-order torques and 47% decrease in all disturbance torques when evaluated at a 15° rotation about the $X - Y$ plane. The total gravitational disturbance torque was decreased from approximately 14.92% to approximately 1.08% of SimSat's available torque when rotated 15° about an axis in the $X - Y$ plane. Additionally, enabling the linear actuators resulted in a 73% decrease in total disturbance torques when evaluated at 5°, dropping the gravitational disturbance torque to approximately 0.18% of the available torque. The result of this research suggests that the rigid body assumption should always be verified on satellite simulators and provides a methodology to do so. In the event that the platform fails the rigid body assumption, the equations of the dynamic imbalance can be calculated from the proposed torque characterization maneuver. A set of linear actuators can then be programmed to counteract not just the zero- and first-order component of the dynamic imbalance but higher-order torques as well.

V. Hardware Testing of Hybrid Steering Logic for Single-Gimbal Control Moment Gyroscopes

In this chapter, a series of experiments were conducted to evaluate the performance of the Hybrid Steering Logic (HSL) for a SGCMG array. HSL is called a "hybrid" because it combines two methods of singularity avoidance, torque error and null motion. Previous publications have shown HSL to be more effective in simulation than Local Gradient (LG) and Singular Direction Avoidance (SDA), the two methods that HSL is comprised of. Therefore, this chapter will primarily focus on duplicating the increase in effectivity when implementing HSL on the AFIT second generation satellite attitude simulator (SimSat). Although this has been attempted previously [41] as we will discuss later in Sec. 5.2, there were some anomalies in the experiment and the researchers felt that with an increased MOI characterization and a reduction and identifications of the disturbance torques that the experiment can be repeated and provide more conclusive results.

5.1 Introduction

Single gimbal control moment gyroscope (SGCMG) arrays have been used in spacecraft that require large amounts of torque, whether it be for very large spacecraft, like the International Space Station, under standard operating conditions or smaller spacecraft, like the Worldview spacecraft, that are required to perform rapid-slew maneuvers. Control moment gyroscope (CMG) arrays are chosen for these types of applications because they capitalize on a phenomenon known as torque amplification. By using an electric gimbal motor to re-orient a spinning flywheel, the induced counter-torque is equal to the product of the gimbal rate and the flywheel angular momentum h_0. This design allows a relatively low-torque gimbal motor, re-orienting a

flywheel, to effectively impart a counter-torque on the spacecraft orders of magnitude larger than its torque rating [25].

Aside from the torque advantage of CMG arrays, they are also inherently prone to singularities [21]. The previously discussed singularities are due to the fact that a SGCMG can only produce torque normal to both its body-fixed single gimbal axis and its flywheel momentum vector. Therefore, a SGCMG can only instantaneously produce torque about one axis. As a result, a CMG array often employs multiple SGCMGs in an array to produce an available torque that spans the standard three dimensional Euclidean space. Though dual gimbal control moment gyroscopes behave similarly with the addition of another gimbal axis, only the dynamics associated with SGCMGs will be analyzed in this chapter, as they are commonly used in spacecraft applications.

Each SGCMG in the array has a flywheel momentum vector that is typically changing direction, with respect to the spacecraft body frame, which makes the available torque a function of the gimbal angle. Therefore, the available torque for a CMG array is a function of the n fixed gimbal axes and the time varying gimbal angles, where n is the number of SGCMG in the array. As these gimbal angles change, the available torque vector from each gimbal changes and affords the opportunity for the available torque vector of two gimbals to align, instantaneously reducing a degree of freedom for the array. One singularity avoidance method, which is commonly used to avoid this, is to only operate in a narrow band of gimbal angles. This limits the CMG array to operate in a small portion of its momentum envelope. One type of CMG array that implements this singularity avoidance technique is the $^3/_4$ box configuration [21]. Unfortunately, operating within a small portion of the CMG array's angular momentum envelope requires the flywheels to store larger amounts of angular momentum to achieve the same amount of available torque and momentum storage.

This increased angular momentum requirement results in higher spin rates or larger flywheels.

Since increasing the operational spin rate of a motor is not always possible, increasing the angular momentum of a CMG often results in larger flywheels that are typically heavy and bulky. Since weight and volume are strong considerations for launch cost, using larger, heavier flywheels is not always desirable. An additional option for singularity avoidance is to couple two SGCMGs specifically to produce a torque in one direction as done with the scissor pair configuration [43]. A disadvantage of the scissor pair configuration is that it requires six SGCMGs to produce a torque that spans three-space [21]. The pyramid configuration has four SGCMGs where the torque plane from each SGCMG forms the side of a pyramid. These four unique torque planes make it impossible for all four torque vectors to become colinear, guaranteeing a Jacobian with a minimum rank of two. This means that at singularity the CMG array can still create torque in two directions, as opposed to a rank one singularity where torque can only be produced in one direction [22].

5.2 Background

The research conducted in this chapter is a re-evaluation of research that was previously conducted on SimSat. This research was re-evaluated since the previous results were somewhat inconclusive [41]. The experiment consisted of repeating a single attitude control maneuver being repeated to test three steering laws with each steering law being tested at three different gimbal starting positions–away from singularity, near an elliptic singularity, and near a hyperbolic singularity. The reason that the research is considered somewhat inconclusive is that for the third set of initial conditions, where the CMG array began near hyperbolic singularity, all three singularity avoidance steering laws came within a close enough proximity to a singularity

that the gimbal rates became highly erratic and ultimately exceeded the gimbal rate limit of 1.5 radians per second. It was hypothesized that a potential cause for the irregularity that lead to a disagreement between the simulated results and the experimental results was that excessive gravitational disturbance torques might have driven the CMG array closer to the singularity than the original simulation. One way to estimate the magnitude of the disturbance torques is to evaluate the conservation of total spacecraft angular momentum by summing the estimated angular momentum of SimSat with the estimated angular momentum of the CMG array. In other words, if we knew the angular momentum of both SimSat and the CMG array, then any non-zero angular momentum would be a result of the time integration of the gravitational disturbance torques or the disturbance torque angular momentum. Unfortunately, it was impossible to implement this additional analysis on the original data due to the lack of accuracy and precision in the MOI estimate. After the MOI characterization work implemented in Chapter III and disturbance torque characterization and correction from Chapter IV it was decided that the HSL experiment should be repeated, not only in hopes of generating more conclusive results due to the reduction in gravitational disturbance torques, but to allow us to evaluate the conservation of total angular momentum to verify that the CMG array is well characterized and verify that we have effectively reduced the gravitational disturbance torques. Before we discuss the CMG steering laws and the experiment, we will first discuss the experimental platform SimSat with an emphasis on the changes that have been made since the original experiment.

5.3   SimSat II

The platform used for the presented experiment is AFIT's simulator satellite, (SimSat). For the original experiment, SimSat had the following estimated MOI

$$\begin{bmatrix} 7.58 & 0 & 0 \\ a\, 0 & 8.12 & 0 \\ 0 & 0 & 13.15 \end{bmatrix} \qquad (5.1)$$

The non-diagonal components of the MOI matrix were not estimated and were approximated as zero. The diagonal components of the MOI estimates were calculated without the inclusion of first-order torque correction and were estimated with a relatively low precision of $\pm 8\%$ [25]; therefore, the diagonal components are estimated to be within $\pm 10\%$. The previous test configuration is shown in Fig. 5.1(a).

(a) Original SimSat Test Configuration   (b) CMG Configuration
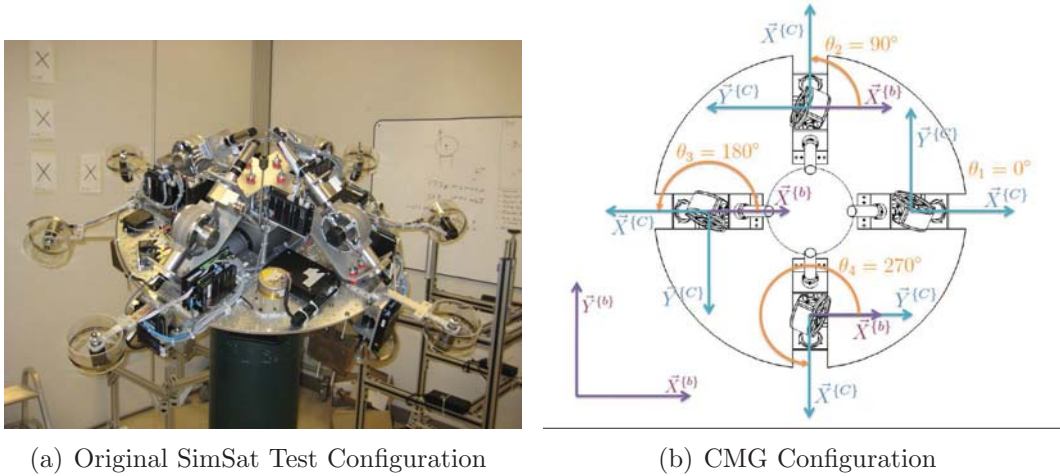
Figure 5.1. SimSat Pyramid CMG Array

SimSat is controlled by a dSPACE® MicroAutoBox® that determines the attitude by integrating the angular rates that are provided by a Northrop Grumman LN−200 fiber optic gyroscope. The LN-200 samples the angular rates at 400 Hz; the signal is then down-sampled via a SkEyes Unlimited LN-200 interpreter board to 200 Hz, making the signal compatible with the dSpace real-time-workshop sample frequency of 1000 Hz. Once the MicroAutoBox® has the current orientation, it compares the current orientation to the desired orientation through a feedback linearized, quaternion error Proportional-Integral-Derivative (PID) controller to cal-

culate the desired torque. Next, a steering law, like HSL, calculates the desired $\dot{\boldsymbol{\delta}}$, an array consisting of the gimbal rates of the CMG array, to best produce the desired torque. The $\dot{\boldsymbol{\delta}}$ command is then sent through a hard 1.5 radian per second limiter and then split to the four gimbal motors. The individual spin rates are sent over a CAN interface at a rate of 10 Hz to the four Maxon EPOS 70/10 controllers that are used to command the motors. Each EPOS 70/10 will respond to one of the four gimbal rate commands. To reduce the data traffic on the CAN bus, the EPOS uses a shaft encoder on its respective gimbal motor to measure the current motor spin rate. It then uses a separate, on-board closed-loop PID controller to calculate the desired motor command signal required to bring the gimbal motor to the desired gimbal motor spin rate.

The gimbal motor is an EC-MAX-30 brushless motor with a GP-32 159:1 reduction gearbox. The gimbal assembly has an MOI about the gimbal axis of 0.00352 kgm^2; and as previously mentioned, the gimbal rotation rate has a hard saturation rate limit of 1.5 radians per second. The higher the value of the gimbal rate saturation, the more torque the CMG can produce, resulting in larger stresses on the structure and bearings. SimSat was structurally over-designed as weight was not much of a concern, but for on orbit spacecraft this is typically not the case and gimbal rates are a larger concern. As a result, we implement a gimbal rate limit of 1.5 radians per second to better duplicate on orbit platform restrictions.

The presence of a gearbox introduces 1° of gear lash. Therefore, a shaft encoder was added directly to the gimbal assembly to measure the actual angle of the gimbal. A Baumer Electric G0AMH absolute 13 bit optical encoder with a resolution of 8192 steps per turn was chosen.

The SimSat platform has a four SGCMG pyramid configuration with a desired skew angle Θ of 54.74°. This pyramid configuration was chosen due to its size,

simplicity, and its minimum Jacobian rank of two, meaning that there will only be a maximum of one singular direction. Furthermore, a pyramid skew angle Θ of 54.74° was chosen, to produce a near symmetric momentum envelope in all three axis. The current SimSat CMG configuration is shown in Fig. 5.1 [25].

Each CMG flywheel has a moment of inertia of approximately 0.00165 kgm^2 and are spun at a nominal 2600 rpm using a Maxon EC-45 flat motor. This results in each flywheel storing approximately 0.45 Nms of angular momentum.

5.3.1 Modifications to SimSat Since Previous Experiment.

After the configuration changes in Chapter IV, the MOI estimation method presented in Chapter III was repeated. The MOI estimate after the configuration changes is now

$$
\begin{bmatrix}
6.81 & -0.16 & 0.04 \\
-0.16 & 10.04 & -0.14 \\
0.04 & -0.14 & 12.88
\end{bmatrix} .
\tag{5.2}
$$

The MOI estimate shown in Eq. (5.2) has an estimated accuracy of approximately ± 0.013 kgm^2 or approximately $\pm 0.17\%$ of the MOI estimate about the $X-$axis. After the configuration change and corresponding reduction in the MOI about the $X-$axis, the previous controller gains were driving SimSat unstable. Since the MOI was known with a much higher precision that was achievable previously, we decided to implement PID controller gains based on a desired natural frequency of the system response and a desired dampening coefficient. This methodology differs from the previous gains which were

$$P = 5$$

$$I = 0.1 \tag{5.3}$$

$$D = 11$$

for all three axes. To calculate the desired controller gains, we first consider the following second order differential equation that represents the feedback linearized system response

$$I\ddot{\omega} + D\dot{x} + Px = 0. \tag{5.4}$$

In this form the controller gains are P and D and I is the moment of inertia. Instead, we desired a system response in the following format

$$\ddot{x} + 2\zeta\omega_0\dot{x} + \omega_0^2 x = 0. \tag{5.5}$$

When a second-order differential equation is written in this form, ω_0 is the natural frequency and ζ is the damping coefficient. These two values are selected based on the desired system response. The desired gains P and D can be calculated from ω_0, ζ, and the MOI estimate I as

$$\begin{aligned} P &= \omega_0^2 I \\ D &= 2\zeta\omega_0 I \end{aligned} \tag{5.6}$$

For SimSat we chose the following controller specifications

$$\begin{aligned} \omega_0 &= 0.3 \\ \zeta &= 0.5 \end{aligned} \tag{5.7}$$

which stabilized the system but resulted in smaller commanded torques and longer

maneuver times. When we substitute into Eqs. (5.6) we calculated the following gains

$$P_x = 0.61$$

$$P_y = 0.90$$

$$P_z = 1.16$$

$$D_x = 2.04$$

$$D_y = 3.01$$

$$D_z = 3.86$$

(5.8)

which are less aggressive than the original gains and can be easily seen when in Sec. 5.7 we compare the platform response from the previous controller gains to the platform response with the new controller gains. The gain for the integration of the error I was kept at 0.1.

In addition to implementing new gains, a linear actuation system was implemented to correct for the gravitational disturbance torques due to structural deflection. First, an equation for the structural deflection was assumed to be in the form

$$\delta m = k^{-1} \begin{bmatrix} \theta_x \\ \theta_y \\ \theta_x^3 \\ \theta_y^3 \end{bmatrix}$$

(5.9)

where δm is a mass-normalized representation of the change in the center of mass and represented with the units of gmm. When using quaternions, the current orientation can be considered a vector that represents a rotation from a nominal position. If you took the vector that represents the current position and projected the vector onto the $X - Y$ plane, θ_x and θ_y are the angles represented by the vector components in the $X-$ and $Y-$axes respectively whose vector sum represents the projection of the

current rotation vector onto the $X - Y$ plane.

The matrix k^{-1} is the inverse stiffness matrix and was experimentally estimated to be

$$
k^{-1} = \begin{bmatrix} -226\frac{\text{g\,mm}}{\text{rad}} & -1335\frac{\text{g\,mm}}{\text{rad}} & 0 & -16848\frac{\text{g\,mm}}{\text{rad}^3} \\ -1317\frac{\text{g\,mm}}{\text{rad}} & -341\frac{\text{g\,mm}}{\text{rad}} & 15891\frac{\text{g\,mm}}{\text{rad}^3} & 0 \\ -1634\frac{\text{g\,mm}}{\text{rad}} & 3253\frac{\text{g\,mm}}{\text{rad}} & 0 & 0 \end{bmatrix}. \tag{5.10}
$$

The linear actuation system is used to counteract the change in the center of the mass. The linear actuation system consists of three linear actuators that are nominally at 50% deflection or 50 mm. The control system calculates desired deviations from the nominal position

$$
\begin{bmatrix} dm_x \\ dm_y \\ dm_z \end{bmatrix} \tag{5.11}
$$

where dm_x, dm_y, and dm_z are the commanded distances from the neutral position for the linear actuators in the $X-$, $Y-$, and $Z-$axes respectively. The linear actuators have masses of approximately 60 g attached to them and the changes in the position result in the following experimentally estimated normalized movement in the center of mass

$$
M = \begin{bmatrix} 62.33 & -1.84 & 1.39 \\ 0.44 & 63.59 & -0.46 \\ -16.28 & -2.91 & 60.03 \end{bmatrix} \frac{\text{g\,mm}}{\text{mm}}. \tag{5.12}
$$

The desired commanded position of the linear actuation system is calculated as a function of the current position as

$$
\begin{bmatrix} dm_x \\ dm_y \\ dm_z \end{bmatrix} = -M^{-1}k^{-1} \begin{bmatrix} \theta_x \\ \theta_y \\ \theta_x^3 \\ \theta_y^3 \end{bmatrix} \tag{5.13}
$$

The linear actuation system was implementation in Chapter IV and experimental results suggest an estimated ± 3 mNm disturbance torque for rotations about the $X - Y$ plane of less than $15°$.

5.3.2   Attitude Control System.

CMG arrays are angular momentum storage devices similar to RW. Unlike a RW that has a fixed angular momentum direction and a varying angular magnitude, a CMG has a nearly constant angular momentum magnitude and induces a torque on the spacecraft by changing the direction of the angular momentum vector. As a result, the governing equations for CMG array are significantly different than the equations that govern an RW array. In this section we will derive the equations of motion for the CMG array.

5.3.3   Rigid Body Dynamics.

Angular momentum is defined as

$$
\vec{h} = \mathbf{I}\,\vec{\omega} \tag{5.14}
$$

where $\mathbf{I}$ is the object's mass MOI tensor, and $\vec{\omega}$ is the object's angular velocity [33]. The time rate of change of centroidal angular momentum is

$$
\vec{M} = \dot{\vec{h}} = \frac{d^{\{i\}}}{dt}\vec{h} \tag{5.15}
$$

121

where $\vec{M}$ represents the applied moments and $\dot{\vec{H}}$ represents time rate of change of centroidal angular momentum with respect to an inertial reference frame $\{i\}$.

The derivative of Eq. (5.15) can be taken in the body frame $\{b\}$, where the MOI is assumed to be constant, and can be written as.

$$\vec{M} = \frac{d}{dt}^{\{i\}}\vec{h} = \mathbf{I}\,\frac{d}{dt}^{\{b\}}\vec{\omega} + \vec{\omega} \times \mathbf{I}\,\vec{\omega} \tag{5.16}$$

where $\mathbf{I}$ is the MOI expressed in the body frame about the center of mass and $\vec{\omega}$ is the angular rate of both the body and body frame relative to an inertial frame.

$$\vec{M} = \mathbf{I}\,\frac{d}{dt}^{\{b\}}\vec{\omega} + \vec{\omega} \times \mathbf{I}\,\vec{\omega}, \tag{5.17}$$

Eq. (5.17) is commonly known as Euler's rotation equations of motion for rigid bodies. Converting Eq. (5.17) to Newtonian notation results in

$$\vec{M} = \mathbf{I}\,\dot{\vec{\omega}} + \vec{\omega} \times \mathbf{I}\,\vec{\omega} \tag{5.18}$$

where all vectors are expressed in the body frame. Euler's equation allows for analysis of the spacecraft dynamics while operating in the body frame. Except where explicitly stated, all equations for the remainder of Section 5.3 are expressed in the body frame.

5.3.4 Angular Momentum Exchange.

Euler's equations assume the spacecraft is a single rigid body, but a spacecraft containing movable actuators clearly is not. In order to apply the equations developed in Section 5.3.3, it is necessary to break the spacecraft's angular momentum up as

$$\vec{h}_{\text{net}} = \vec{h}_{\text{body}} + \vec{h}_{\text{acs}}. \tag{5.19}$$

Substituting Eq. (5.15) in Eq. (5.19)

$$\vec{M} = \mathbf{I} \, \dot{\vec{\omega}} + \dot{\vec{h}}_{\text{acs}} + \vec{\omega} \times \left(\mathbf{I} \, \vec{\omega} + \vec{h}_{\text{acs}} \right). \tag{5.20}$$

Now, if the applied external moments are assumed to be negligible, a valid assumption for most spacecraft over short time spans, Eq. (5.20) can be re-arranged, such that

$$\mathbf{I}\dot{\vec{\omega}} = -\dot{\vec{h}}_{acs} - \vec{\omega} \times \left(\mathbf{I} \, \vec{\omega} + \vec{h}_{\text{acs}} \right). \tag{5.21}$$

From Eq. (5.21), it is clear that changing $\dot{\vec{h}}_{\text{acs}}$ in magnitude or direction will create an equal and opposite change in $\dot{\vec{\omega}}$. As these rates are integrated over time they show the angular momentum that is exchanged between the actuator and the body, hence their description as 'Momentum Exchange Devices.' The reaction wheels on SimSat were disabled during the experiment; therefore, future references to Euler's equation will have $\vec{h}_{\text{acs}}$ and $\dot{\vec{h}}_{\text{acs}}$ replaced with $\vec{h}_{\text{cmg}}$ and $\dot{\vec{h}}_{\text{cmg}}$.

5.3.5 Control Moment Gyroscopes.

In this section we will present a concise overview of the governing equations; however, an in depth derivation of the equations of motion for the CMG configuration on SimSat was performed by McChesney [25].

The angular momentum of the CMG array is the sum of the four individual SGCMG, expressed as

$$\vec{h}_{\text{cmg}} = \sum_{i=1}^{4} \left(\mathbf{R}_3(\theta_i)^T \begin{bmatrix} I_G\cos(\Theta)\dot{\delta}_i + I_R\Omega\sin(\Theta)\cos(\delta_i) \\ -I_R\Omega\sin(\delta_i) \\ -I_G\sin(\Theta)\dot{\delta}_i + I_R\Omega\cos(\Theta)\cos(\delta_i) \end{bmatrix} \right). \tag{5.22}$$

where I_G is the MOI of the rotating CMG assembly about the gimbal axis. Addi-

tionally, I_R is the MOI about the CMG flywheel's rotation axis and Ω is the angular velocity of the CMG flywheel about the rotation axis. The $\mathbf{R}_3(\theta_i)$ term represents a the rotation matrix that rotates the angular momentum from the CMG reference frame into the spacecraft body frame. Differentiating with respect to an inertial frame results in

$$
\dot{\vec{h}}_{\mathtt{net}} = \mathbf{I}\,\dot{\vec{\omega}} + \sum_{i=1}^{4}\left(\mathbf{R}_3(\theta_i)^T \begin{bmatrix} I_G\cos(\Theta)\ddot{\delta}_i - I_R\Omega\sin(\Theta)\sin(\delta_i)\dot{\delta}_i \\ -I_R\Omega\cos(\delta_i)\dot{\delta}_i \\ -I_G\sin(\Theta)\ddot{\delta}_i - I_R\Omega\cos(\Theta)\sin(\delta_i)\dot{\delta}_i \end{bmatrix}\right) +
$$
$$
\vec{\omega}\times\mathbf{I}\,\vec{\omega} + \vec{\omega}\times\sum_{i=1}^{4}\left(\mathbf{R}_3(\theta_i)^T \begin{bmatrix} I_G\cos(\Theta)\dot{\delta}_i + I_R\Omega\sin(\Theta)\cos(\delta_i) \\ -I_R\Omega\sin(\delta_i) \\ -I_G\sin(\Theta)\dot{\delta}_i + I_R\Omega\cos(\Theta)\cos(\delta_i) \end{bmatrix}\right).
$$

$$(5.23)$$

Equation (5.23) can be simplified if certain assumptions are made, specifically

$$
\dot{\delta}_i \ll \Omega
$$
$$
\ddot{\delta}_i \ll \Omega\dot{\delta}_i
$$

$$(5.24)$$

which were shown to be valid for SimSat by McChesney [25]. Applying the assumptions in Eqn. (5.24) reduces Eq. (5.22) to

$$
\vec{h}_{\mathrm{cmg}} \approx I_R\Omega \begin{bmatrix} -\sin(\Theta)\sin(\delta_1) & -\cos(\delta_2) & +\sin(\Theta)\sin(\delta_3) & +\cos(\delta_4) \\ -\cos(\delta_1) & +\sin(\Theta)\sin(\delta_2) & +\cos(\delta_3) & -\sin(\Theta)\sin(\delta_4) \\ \cos(\Theta)\sin(\delta_1) & +\cos(\Theta)\sin(\delta_2) & +\cos(\Theta)\sin(\delta_3) & +\cos(\Theta)\sin(\delta_4) \end{bmatrix}.
$$

$$(5.25)$$

Furthermore, by defining a matrix $\mathbf{A}$ as

$$
\mathbf{A} = \frac{\partial\boldsymbol{\delta}}{\partial\mathbf{h}_{\mathrm{cmg}}}
$$

$$(5.26)$$

124

the matrix $\mathbf{A}$ can be evaluated for the current CMG array as

$$\mathbf{A} = \begin{bmatrix} -\sin(\Theta)\cos(\delta_1) & \sin(\delta_2) & \sin(\Theta)\cos(\delta_3) & -\sin(\delta_4) \\ \sin(\delta_1) & \sin(\Theta)\cos(\delta_2) & -\sin(\delta_3) & -\sin(\Theta)\cos(\delta_4) \\ \cos(\Theta)\cos(\delta_1) & \cos(\Theta)\cos(\delta_2) & \cos(\Theta)\cos(\delta_3) & \cos(\Theta)\cos(\delta_4) \end{bmatrix} . \quad (5.27)$$

After defining $\mathbf{A}$, $\dot{\vec{h}}_{\mathrm{cmg}}$ can be approximated as

$$\dot{\vec{h}}_{\mathrm{cmg}} \approx I_R \Omega \mathbf{A} \dot{\boldsymbol{\delta}} \quad (5.28)$$

where $\dot{\boldsymbol{\delta}}$ is defined as

$$\dot{\boldsymbol{\delta}} = \begin{bmatrix} \dot{\delta}_1 & \dot{\delta}_2 & \dot{\delta}_3 & \dot{\delta}_4 \end{bmatrix}^{\mathrm{T}} \quad (5.29)$$

Eq. (5.23) then reduces to

$$\dot{\vec{h}}_{\mathbf{net}} = \mathbf{I}\,\dot{\vec{\omega}} + I_R \Omega \mathbf{A} \dot{\boldsymbol{\delta}} + \vec{\omega} \times \mathbf{I}\,\vec{\omega} + \vec{\omega} \times \vec{h}_{\mathbf{cmg}}. \quad (5.30)$$

In this form, $I_R \Omega \mathbf{A} \dot{\boldsymbol{\delta}}$ is the controller solution and the control command $\dot{\boldsymbol{\delta}}$ must be solved for. However the Jacobian $\mathbf{A}$ is not square and is therefore not directly invertible. Solutions to this equation, when applied to CMG arrays, are known as steering laws.

5.4   Singularities

In mathematics, a singularity is defined as something that is undefined or not well behaved. In controls, it is often used to describe a scenario where the set of possible outputs is a subset of the desired outputs. This results in desired outputs that cannot be produced and therefore the controls required to obtain the output

125

cannot be defined. When controlling a satellite's attitude with a CMG array, gimbal rates $\dot{\boldsymbol{\delta}}$ are commanded to produce torques in a Euclidean three-space. As a result, a CMG array is considered at singularity when the Jacobian has a rank less than 3. This means there is at least one axis in the desired three dimensional output about which the CMG array cannot produce a torque.

5.4.1 Elliptical Singularities.

There are two primary types of singularities: elliptical and hyperbolic [21]. At an elliptic singularity, the angular momentum of the ACS has only one solution that results in a singular Jacobian and a unique set of gimbal angles $\boldsymbol{\delta}$ that produce the desired angular momentum. This single solution results in no possibility of having a different set of gimbal angles $\boldsymbol{\delta}_2$ that produce the same angular momentum with a full rank Jacobian.

Elliptic singularities have two subsection types: internal and external. As the name suggests, external elliptic singularities exist on the exterior of the momentum envelope. An example would be a pyramid configuration at

$$\boldsymbol{\delta} = \left[\begin{array}{cccc} \pi/2 & \pi/2 & \pi/2 & \pi/2 \end{array} \right]^{\mathrm{T}}. \tag{5.31}$$

Since this is the only configuration that will produce maximum momentum in the Z-axis, this is an example of an external elliptical singularity.

5.4.2 Hyperbolic Singularities.

A hyperbolic singularity is one in which the gimbal angles required to achieve the desired angular momentum are not unique. These solutions exist on continuous solution sets that can be traversed using null motion–gimbal rates that have a net zero effect on the angular momentum. Hyperbolic singularities have two subsection

types: non-degenerate and degenerate [21].

For non-degenerate hyperbolic singularities, there exists a set of gimbal angles that produce the same angular momentum but have a full ranked Jacobian. An example of a non-degenerate hyperbolic singularity for the CMG array with angular momentum provided in Eq. (5.25) at the gimbal angles

$$\boldsymbol{\delta} = \begin{bmatrix} \pi/2 & -\pi/2 & \pi/2 & -\pi/2 \end{bmatrix}^{\mathrm{T}}. \tag{5.32}$$

This is a zero momentum configuration like

$$\boldsymbol{\delta} = \begin{bmatrix} 0 & 0 & 0 & 0 \end{bmatrix}^{\mathrm{T}} \tag{5.33}$$

however, the Jacobian is singular in Eq. (5.32) and not in Eq. (5.33); therefore, Eq. (5.32) represents a non-degenerative hyperbolic singularity, respectively.

5.4.3 Mathematical Characteristics of Singularities.

In order for null motion to exist, there are first- and second-order necessary conditions that must be satisfied. The first-order condition for any potential null vector is that it exists in the null space of the Jacobian; this requirement ensures the first-order torque contributions are zero. The second-order necessary condition is the requirement that the second-order effects must also be zero [1; 21]. At singularity, $\mathbf{A}$ has a rank of two. For a four CMG configuration this ensures two candidate null vectors: $\mathbf{N}_1$ and $\mathbf{N}_2$. Let matrix $\mathbf{Q}$ represent the second-order change in momentum along a singular axis due to $\mathbf{N}_1$ and $\mathbf{N}_2$. In order for there to be a net zero change in angular momentum, there has to exist a vector $\boldsymbol{\lambda}$ comprised of a linear combination of $\mathbf{N}_1$ and $\mathbf{N}_2$ that produces a net zero effect on the momentum. This linear combination $\boldsymbol{\lambda}$ would have to satisfy the following equation

127

$$\boldsymbol{\lambda}^{\mathrm{T}}\mathbf{Q}\boldsymbol{\lambda} = 0. \tag{5.34}$$

For a four CMG arrangement, a simple way to determine if this equation has a solution is to calculate the determinate of $\mathbf{Q}$. If $\mathbf{Q}$ is definite, then no real vector $\boldsymbol{\lambda}$ can satisfy the zero momentum change requirement. Therefore, a positive determinate indicates an elliptical singularity while a negative or zero value of $\det[\mathbf{Q}]$ indicates a hyperbolic singularity.

5.5 Steering Laws

Once the desired controller solution $\dot{h}_{\mathrm{cmg}}$ is obtained, the gimbal rates $\dot{\boldsymbol{\delta}}$ must be computed from

$$\dot{h}_{\mathrm{acs}} = \dot{h}_{\mathrm{cmg}} = \mathbf{A}(\boldsymbol{\delta})\dot{\boldsymbol{\delta}} \ . \tag{5.35}$$

Difficulties arise in trying to compute the corresponding $\dot{\boldsymbol{\delta}}$. The primary difficulty is due to the fact that the matrix $\mathbf{A}$ defined in Eq. (5.27) is an 3xN matrix where N is the number of gimbals in the CMG configuration. For a configuration of three full range SGCMGs it is possible for the available torque vector of all SGCMGs to become coplanar such that a column of the Jacobian can be represented as a linear combination of the other two. This would be considered a rank two singularity since the control matrix $\mathbf{A}$ has only two linearly independent columns, and the available torque spans only a plane instead of all three dimensions. As a result, any desired torque outside of the plane is unobtainable. One method used to counter this is to employ four SGCMG in the array. This requires multiple gimbal alignments to occur for $\mathbf{A}$ to have a rank less than three. Since this generally produces a matrix $\mathbf{A}$ that is wider than it is tall, the easiest way to solve for $\dot{\boldsymbol{\delta}}$ is to take the Moore-Penrose

Pseudoinverse (MPPI)

$$\dot{\boldsymbol{\delta}} = \mathbf{A}^{\mathrm{T}}(\mathbf{A}\mathbf{A}^{\mathrm{T}})^{-1}\dot{\mathbf{h}}_{\mathtt{acs}} \tag{5.36}$$

where the pseudo-inverse operation is defined as

$$\mathbf{A}^{\mathrm{T}}(\mathbf{A}\mathbf{A}^{\mathrm{T}})^{-1} \overset{\mathrm{def}}{=} \mathbf{A}^{+}. \tag{5.37}$$

For $(\mathbf{A}\mathbf{A}^{\mathrm{T}})^{-1}$ to be well defined, $\mathbf{A}$ must be at least rank three. Even though the pyramid configuration has a minimum rank of two, that still causes a poorly scaled $\mathbf{A}^{+}$ and the numerical methods used to compute the MPPI begin to break down. It should be noted that none of the steering laws used in this chapter can escape gimbal lock, as a result this work will concentrate on combining two singularity avoidance methods called SDA [8] and LG [5], which are discussed next.

5.5.1 Singular Direction Avoidance.

The singular direction avoidance (SDA) method is an alternative approach to compute the pseudo-inverse that induces a torque error in the most singular direction. In the Singular Value Decomposition (SVD) approach, the matrix being inverted is decomposed into a left unitary matrix $\mathbf{U}$, a right unitary matrix $\mathbf{V}^{\mathrm{T}}$, and a diagonal matrix $\boldsymbol{\Sigma}$ whose components are

$$\boldsymbol{\Sigma} = \begin{bmatrix} \sigma_1 & 0 & 0 & 0 \\ 0 & \sigma_2 & 0 & 0 \\ 0 & 0 & \sigma_3 & 0 \end{bmatrix} \tag{5.38}$$

where each σ_i is a singular value of the Jacobian. After decomposition, $\mathbf{A}$ can be written as

$$\mathbf{A} = \mathbf{U}\boldsymbol{\Sigma}\mathbf{V}^{\mathrm{T}} \tag{5.39}$$

and the pseudo-inverse of $\mathbf{A}$ is simply

$$\mathbf{A}^+ = \mathbf{V}\mathbf{\Sigma}^+\mathbf{U}^{\mathrm{T}} \tag{5.40}$$

where the pseudo-inverse of $\mathbf{\Sigma}$ is simply

$$\mathbf{\Sigma}^+ = \begin{bmatrix} \frac{1}{\sigma_1} & 0 & 0 \\ 0 & \frac{1}{\sigma_2} & 0 \\ 0 & 0 & \frac{1}{\sigma_3} \\ 0 & 0 & 0 \end{bmatrix} \tag{5.41}$$

for all $\sigma_i \neq 0$. As the CMG array approaches a singular configuration, the CMG array us unable to produce torque about one axis, therefore the singular value representing the available torque in that direction approaches zero, and the $\mathbf{\Sigma}^+$ matrix becomes poorly defined. One way to avoid this is with the singularity robust steering logic [38]. By defining a small singularity parameter

$$0 < \gamma_0 << 1 \tag{5.42}$$

a singularity robust Jacobian can be computed from

$$\mathbf{A}^{\mathrm{SR}} = \mathbf{V} \begin{bmatrix} \frac{\sigma_1}{\sigma_1^2+\gamma_0} & 0 & 0 \\ 0 & \frac{\sigma_2}{\sigma_2^2+\gamma_0} & 0 \\ 0 & 0 & \frac{\sigma_3}{\sigma_3^2+\gamma_0} \\ 0 & 0 & 0 \end{bmatrix} \mathbf{U}^{\mathrm{T}} . \tag{5.43}$$

Now the gimbal rates $\dot{\boldsymbol{\delta}}$ can be computed from

$$\dot{\boldsymbol{\delta}} = \mathbf{A}^{\mathrm{SR}}\dot{h}_{\mathrm{acs}} . \tag{5.44}$$

130

By adding the singularity parameter γ_0 to all three principal axes, this method is robust enough to stabilize the pseudo-inverse of any rank singularity. However, in doing so, torque error is introduced to all three output directions. This error is not desirable on spacecraft with highly accurate tracking requirements, so it should be reduced whenever possible. One way to reduce the torque error is to use a method introduced by Ford and Hall commonly referred to as SDA [8]. In SDA, a common SVD form is used such that the diagonal singular value matrix $\mathbf{\Sigma}$ is rotated such that the diagonal values σ_i are non-increasing. In this form, the smallest singular value is σ_3 [14]. Furthermore, the distance from singularity is defined as

$$ m = \sqrt{\det(\mathbf{A}\mathbf{A}^{\mathrm{T}})} \ . \tag{5.45} $$

This distance from singularity can then be used in a decaying singularity measure γ from

$$ \gamma(m) = \gamma_0 e^{(-\mu m)} \tag{5.46} $$

which is then included in the inverse of the most singular direction

$$ \mathbf{A}^{\mathbf{SDA}} = \mathbf{V} \begin{bmatrix} \frac{1}{\sigma_1} & 0 & 0 \\ 0 & \frac{1}{\sigma_2} & 0 \\ 0 & 0 & \frac{\sigma_3}{\sigma_3^2 + \gamma} \\ 0 & 0 & 0 \end{bmatrix} \mathbf{U}^{\mathrm{T}} \tag{5.47} $$

and

$$ \dot{\boldsymbol{\delta}} = \mathbf{A}^{\mathbf{SDA}} \dot{h}_{\mathrm{acs}} \ . \tag{5.48} $$

Though this eliminates the torque error about the two least singular directions, the SDA method still introduces torque error when approaching all singularities, including those that can be avoided by using null motion. Next, we will discuss a method that

does avoid those avoidable singularities and later we will combine these methods as originally done by Leve [21].

5.5.2 Local Gradient.

Another method to avoid singularities is the local gradient (LG) method [5], which employs null motion in an attempt to avoid singularities. By using the distance from singularity m, as defined by Eq. (5.45), an objective function is created from

$$f = \frac{1}{m} \tag{5.49}$$

the direction away from singularity can be defined as

$$\mathbf{d} = \nabla f = \frac{\partial m}{\partial f}\left(\frac{\partial \boldsymbol{\delta}}{\partial m}\right)^T = \frac{-1}{m^2}\left(\frac{\partial \boldsymbol{\delta}}{\partial m}\right)^T \tag{5.50}$$

the gradient of the objective function $\mathbf{d}$ is then projected onto the null space

$$\mathbf{n} = [\mathbf{1} - \mathbf{A}^+\mathbf{A}]\mathbf{d} \tag{5.51}$$

where $\mathbf{A}^+$ is computer from the SVD method, which can be expanded as

$$n = [\mathbf{VIV}^{\mathrm{T}} - \mathbf{V\Sigma U}^{\mathrm{T}}\mathbf{U\Sigma}^+\mathbf{V}^{\mathrm{T}}]\mathbf{d} \tag{5.52}$$

to better identify the projection operator [22]. The projection operation can now be expressed as

$$n = \mathbf{V}\mathrm{diag}(0, 0, 0, 1)\mathbf{V}^{\mathrm{T}}\mathbf{d} \ . \tag{5.53}$$

132

Once the null motion n is calculated, it is then added to the least squares projection

$$\dot{\boldsymbol{\delta}} = \mathbf{A}^+ \dot{h}_{\text{acs}} + \mathbf{n} \tag{5.54}$$

where $\dot{\boldsymbol{\delta}}$ is the required gimbal rates command to produce the desired torque.

5.5.3 Hybrid Steering Logic.

Hybrid Steering Logic (HSL) created by Leve [22] combines the null motion of LG and the torque error of the SDA method by first calculating two coefficients from

$$\alpha = \alpha_0 \exp^{-a\bar{\alpha}} \exp^{-\mu_1 m} \tag{5.55}$$

$$\beta = \beta_0 \exp^{-b\bar{\beta}} \exp^{-\mu_2 m} \tag{5.56}$$

where α and β are ultimately used to control the amount of torque error and null motion, respectively. The variables μ_1, μ_2, a, b, α_0, and β_0 are tuning parameters that are typically chosen to meet desired performance requirements. The values of $\bar{\alpha}$, and $\bar{\beta}$ are calculated in real-time, based on the type of singularity being approached. If the nearest singularity is elliptical, then $\bar{\alpha}$ will be chosen to be small and $\bar{\beta}$ will be chosen to be large, this produces a large α and a small β; effectively increasing the amount of torque error while decreasing the amount of null motion. However, if the nearest singularity is hyperbolic, then the opposite is chosen.

5.5.4 Determining the Type of Singularity.

In order to differentiate between hyperbolic and elliptic singularities, a calculation was developed by Leve [21] to determine if there is a proper null space. At first glance, the available torque from the CMG may appear linear since we have approximated the available torque and represented it as the Jacobian $\mathbf{A}$, a 4×3 matrix that by

133

definition will always have a null space. However, the available torque from the CMG array is non-linear and the matrix $\mathbf{A}$ is merely a first order representation of the available torque. In order for a null solution to exist for the available torque of the CMG array, the first order requirement that the gimbal angles exist in the null space of the Jacobian $\mathbf{A}$ must be satisfied. In addition, the gimbal angles must also produce zero second order effects; satisfying a second order requirement for zero torque effects in the singular direction. To verify that the candidate vectors, those that exist in the null space of the Jacobian, are truly null vectors, the singular direction is defined as

$$\mathbf{A}^T\mathbf{s} = 0 \ . \tag{5.57}$$

Once the singular direction is calculated, the momentum vectors of the gimbals are projected into the singular direction.

$$\mathbf{P} = \mathrm{diag}(\mathbf{h}_i^T\mathbf{s}) \ . \tag{5.58}$$

This projection matrix is then pre- and post-multiplied by $\mathbf{N}$ the candidate control vectors that exist in the null space of the Jacobian $\mathbf{A}$

$$\mathbf{Q} = \mathbf{N}^T\mathbf{P}\mathbf{N} \tag{5.59}$$

where $\mathbf{Q}$ is a matrix that represents the second order effects of the candidate vectors on the momentum in the singular direction. In order for a null space to exist, there has to exist a real vector $\boldsymbol{\lambda}$ such that

$$\boldsymbol{\lambda}^T\mathbf{Q}\boldsymbol{\lambda} = 0 \tag{5.60}$$

where $\boldsymbol{\lambda}$ represents a linear combination of the candidate vectors that produce zero

second order effects required to produce null motion. As a result, the eigenvalues of $\mathbf{Q}$ can determine whether or not a null space exists. In instances where $\mathbf{Q}$ is definite, then Eq. (5.60) cannot be satisfied and therefore a null space does not exist. In these instances, null motion is not possible and an increased torque error is desired. In cases where $\mathbf{Q}$ is semi-definite or indefinite a null space does exist and therefore less torque error and more null motion is desired. As a result $\bar{\alpha}$ and $\bar{\beta}$ are defined as

$$\bar{\alpha} = |\mathbf{Q}_0 - \det\mathbf{Q}| \tag{5.61}$$

and

$$\bar{\beta} = \frac{1}{\bar{\alpha}} \tag{5.62}$$

where $\mathbf{Q}_0$ is another tuning parameter chosen slightly larger than the maximum value of $\det\mathbf{Q}$ to avoid difficulties in calculating $\bar{\beta}$. The modified Jacobian is then defined as

$$\mathbf{A}^{HSL,\alpha} = V \begin{bmatrix} \frac{1}{\sigma_1} & 0 & 0 \\ 0 & \frac{1}{\sigma_2} & 0 \\ 0 & 0 & \frac{\sigma_3}{\sigma_3^2+\alpha} \\ 0 & 0 & 0 \end{bmatrix} U^T \ . \tag{5.63}$$

The desired gimbal rate commands $\dot{\boldsymbol{\delta}}$ can then be calculated as

$$\dot{\delta} = \mathbf{A}^{HSL,\alpha}\dot{h} + \beta n. \tag{5.64}$$

It is apparent that at an infinitesimal distance from singularity the rank$(\mathbf{A}^T)$ is three. Therefore, the singular direction $\mathbf{s}$ is identically zero, which also leads to an identically zero $\mathbf{Q}$, for all singularities. Therefore, the approach used by Leve [21] will be implemented that defines a singularity threshold m_0, and when the singularity measure m is below that threshold the configuration will be considered singular. The

singular direction **s** will be defined as the rightmost column of **U** and the null space **N** will be defined as the rightmost two columns of **V**. This allows for singularity identification, before the configuration actually becomes singular.

5.6 Results

The platform parameters were chosen to closely mimic the simulated results presented by Leve [21], as seen in Table 5.1. The three algorithms compared in the experiment were LG, SDA, and HSL. Since HSL has the tuning parameters α_0, β_0, a, b, μ_1, and μ_2 which determine how much of each of the SDA and LG algorithms to use, the HSL algorithm was used for all three runs. The tuning parameters were changed as needed to achieve only null motion, only torque error, and a combination of torque error and null motion. The parameters chosen are shown in Table 5.2. The tuning parameters chosen were the same used by Leve [21; 22] and again by Wright [41]. For each control algorithm, three experiments were conducted. One case was away from singularity, with the initial conditions $\delta = [0\ 0\ 0\ 0]$ deg, the second was near an external elliptic singularity $\delta = [105\ 105\ 105\ 105]$ deg, and the third was near a hyperbolic singularity $\delta = [15\ 105\ 195\ -75]$ deg. The last two being $15°$ away from the elliptic singularity at $\delta = [90\ 90\ 90\ 90]$ deg and the hyperbolic singularity at $\delta =$

Table 5.1. Experimental Parameters

Variable	Value	Units
I	$\begin{bmatrix} 6.81 & -0.16 & 0.04 \\ -0.16 & 10.04 & -0.14 \\ 0.04 & -0.14 & 12.88 \end{bmatrix}$	kgm^2
Θ	54.74	deg
e_0	$[0.04355\ -0.087105\ -0.043555\ 0.99430]^T$	—
w_0	$[0\ 0\ 0]^T$	deg /s
h_0	0.4492	Nms
Δt	0.001	s

136

[0 90 180 -90] deg, respectively. The tuning parameters used for the three controllers are shown in Table 5.2.

The results from the three controllers are compared with each other based off of Root Mean Square (RMS) null motion of the gimbal rates $\dot{\boldsymbol{\delta}}$ in $^{\text{deg}}/_{\text{sec}}$ as well as torque error in mNm. As a controller approaches singularity, the gimbal rates spike proportionally to the inverse of the most singular value. In order to keep from over-tasking the hardware, saturation limits are put in place. The process is shown in block format in Fig. 5.2.
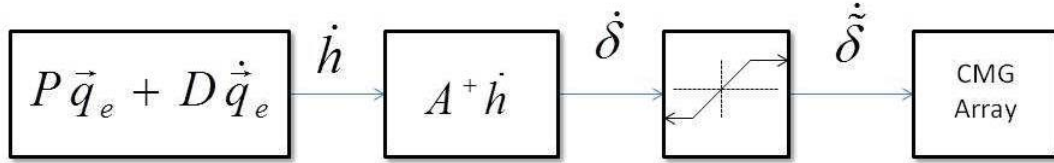

Figure 5.2. Control Sequence

When the desired gimbal rates $\dot{\boldsymbol{\delta}}$ exceed the saturation limits, the commanded gimbal rates $\dot{\tilde{\boldsymbol{\delta}}}$ differ from the desired gimbal rates, possibly introducing an additional torque on the spacecraft that is hardware dependent. Therefore, the torque errors will first be analyzed as pure controller torque error

$$\tau_{err} = \dot{h}_{des} - \mathbf{A}\dot{\boldsymbol{\delta}} \tag{5.65}$$

where $\dot{\boldsymbol{\delta}}$ is the gimbal rates as they exit the steering law. Afterwards the total torque

Table 5.2. HSL Tuning Parameters Used

Steering Law	α_0	β_0	a	b	μ_1	μ_2
LG	0	1	0	0	0	1
SDA	0.01	0	0	0	1	0
HSL	0.01	2	1	3	1	1

error will be analyzed as

$$\tau_{err} = \dot{h}_{des} - \mathbf{A}\dot{\tilde{\boldsymbol{\delta}}} \tag{5.66}$$

where $\dot{\tilde{\boldsymbol{\delta}}}$ is the gimbal rates as they exit the saturation limits.

5.6.1 Results Excluding Gimbal Rate Saturation.

The nine experimental runs were completed and a comparison of the torque error RMS are shown in Table. 5.3. The results show that for the case where the CMG array was away from singularity HSL resulted in 86% less torque error than SDA. If we consider that the singularity measure m stayed greater than 0.5, then we can conclude that $\det[Q]$ was defined as identically zero for the entire maneuver and $\bar{\alpha}$ was identically two. This means that α for the HSL case was a factor of $\exp^{-2}$ or 0.13 times the size of α for the SDA case. As a result, we would expect there to be approximately an 87% difference between the two values and that is experimentally confirmed. We also see that the case near elliptic singularity results in approximately six times the amount of torque error but even though α varied throughout the maneuver HSL still incurred approximately 84% less torque error than the SDA maneuver.

Table 5.4 shows the difference in the RMS null motion between LG and HSL.

Table 5.3. Comparison of Torque Errors between SDA and HSL

Algorithm	Type of Singularity	τ_{err} rms mNm	Percent Difference
SDA	None	5.96×10^{-4}	-
HSL	None	8.08×10^{-5}	-86%
SDA	Elliptic	3.19×10^{-3}	-
HSL	Elliptic	5.08×10^{-4}	-84%
SDA	Hyperbolic	2.2273	-
HSL	Hyperbolic	1.4777	-34%

Comparing the size of β between LG and HSL for the case where the CMG are away from singularity results in an estimate that the null motion of HSL should be multiplied by a factor of $2\exp^{-1.5}$ or approximately 65% less null motion than LG. From Table. 5.4 shows approximately 91% reduction in null motion for the case where the CMG are away from singularity, so we are experiencing an additional 40% larger reduction in null motion than expected by simply by changing the coefficient.

Figure 5.3 shows the torque error from the three SDA maneuvers next to the torque error from the three HSL maneuvers. Figure 5.4 shows the torque error from the three LG maneuvers next to the three HSL maneuvers.

### 5.6.2 Results with Gimbal Rate Saturation.

The values shown in Sec. 5.6.1 represent the best case scenario – the gimbal rate limits never reach saturation. During the maneuver near a hyperbolic singularity, the commanded gimbal rates exceeded the gimbal rate saturation limits of approximately 86° or 1.5 rad per second. Once the gimbal rates exceeded the defined limit the gimbal rates were reduced to 86° inducing an additional torque error not accounted for in the control algorithm. After accounting for gimbal saturation, the torque error applied to the test platform as a result of this saturation, the combined torque error was recalculated and is shown in Table 5.5. The commanded gimbal rates and

Table 5.4. Comparison of Null Motion between LG and HSL

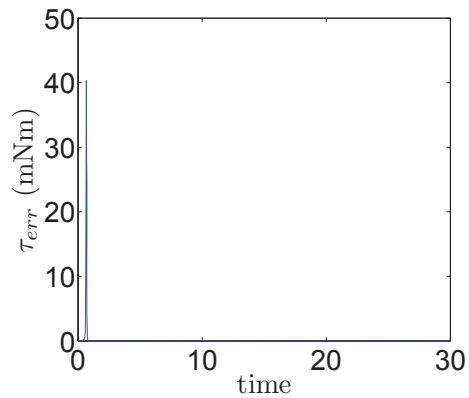| Algorithm	Type of Singularity	τ_{err} rms mNm	Percent Difference
LG	None	8.96	-
HSL	None	0.78	-91%
LG	Elliptic	3.62	-
HSL	Elliptic	0.35	-90%
LG	Hyperbolic	9.83	-
HSL	Hyperbolic	1.02	-90%
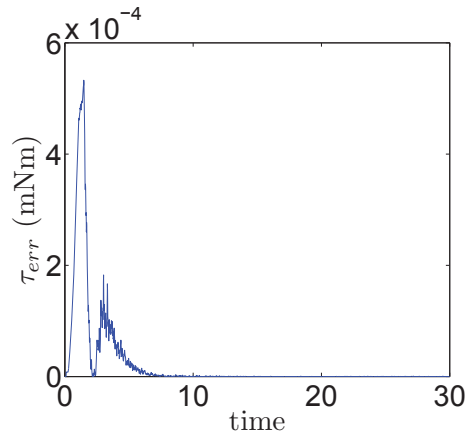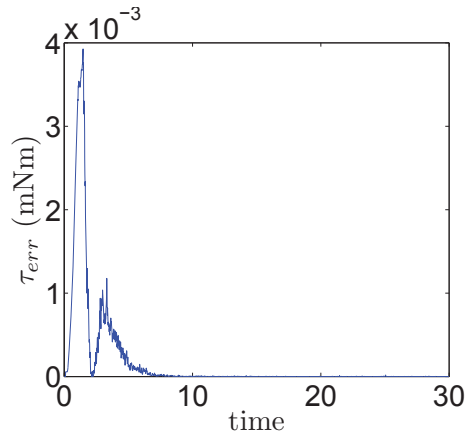
(a) SDA Torque Error Away from Singu-
larity

(b) HSL Torque Error Away from Singu-
larity
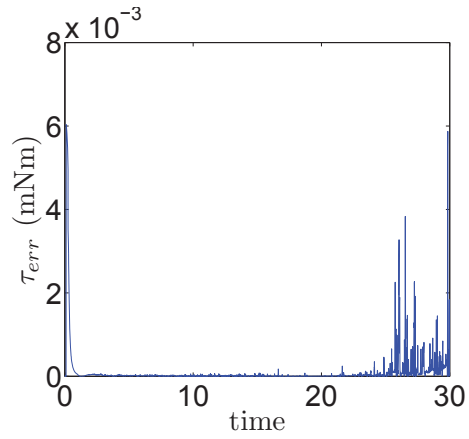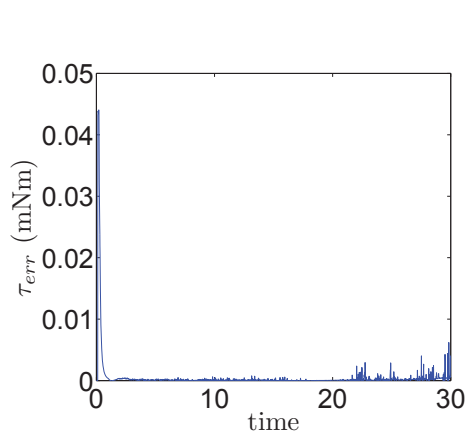
(c) SDA Torque Error Near Elliptic Sin-
gularity

(d) HSL Torque Error Near Elliptic Sin-
gularity
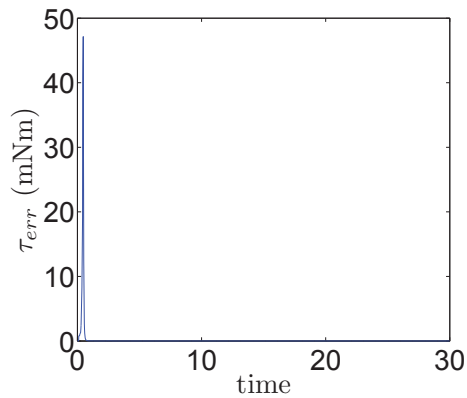
(e) SDA Torque Error Near Hyperbolic
Singularity

(f) HSL Torque Error Near Hyperbolic
Singularity

Figure 5.3. Comparison of Torque Error Between SDA and HSL

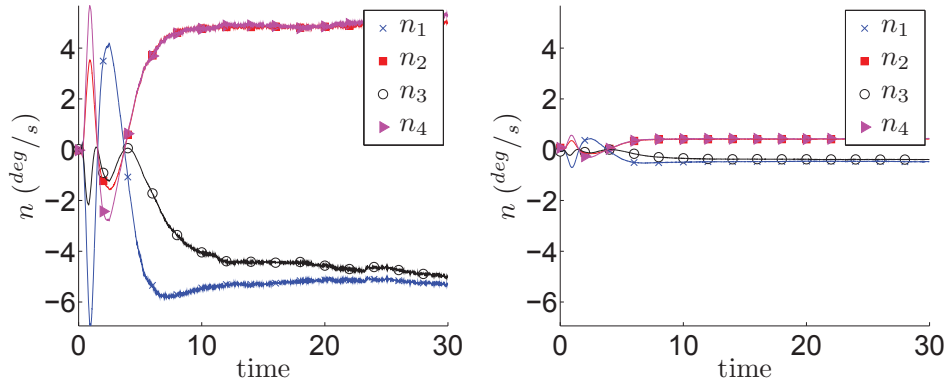(a) LG Null Motion Away from Singular-(b) HSL Null Motion Away from Singu-
ity   larity
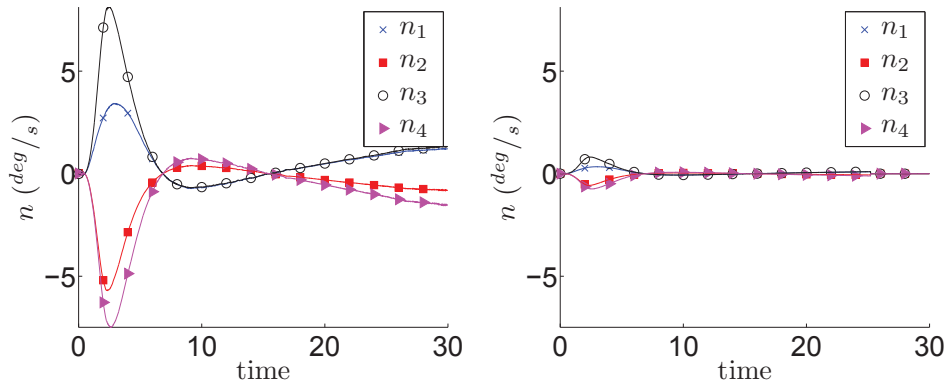
(c) LG Null Motion Near Elliptic Singu-(d) HSL Null Motion Near Elliptic Singu-
larity   larity
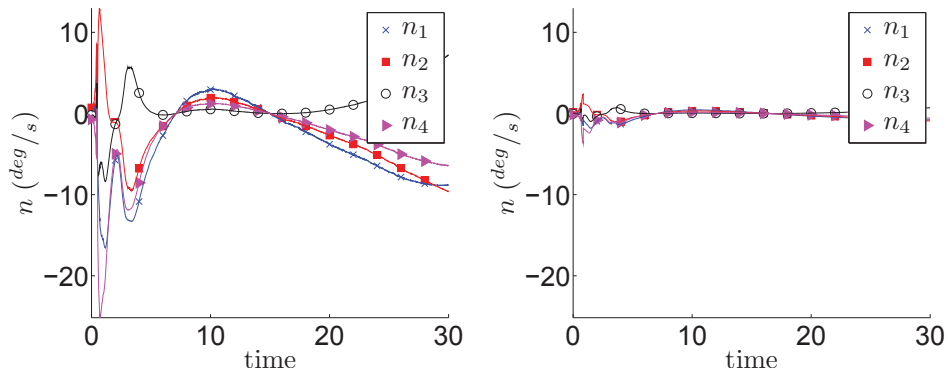
(e) LG Null Motion Near Hyperbolic Sin-(f) HSL Null Motion Near Hyperbolic
gularity   Singularity

Figure 5.4. Comparison of Null Motion Between LG and HSL

corresponding torque errors are shown in Fig. 5.5.

Table 5.5 shows that all three controllers got close enough to a singularity to reach the gimbal rate saturation limits. When the gimbal rate limits were exceeded, SDA outperformed HSL and LG. There are two possible reasons for the inability to avoid the singularity. The first is that the gimbals are only being commanded at a rate of 10 Hz and the second possible reason is that the singularity avoidance coefficients were not aggressive enough for the controller that is implemented on SimSat. An analysis of these two potential causes will be analyzed in Sec. 5.7.1, but first we will compare the current experimental results to the previous experimental results.

<div align="center">

Table 5.5. Experimental results

Algorithm	Type of Singularity	τ_{err} rms mN-m	Percent Difference
SDA	Hyperbolic	22.6	-
LG	Hyperbolic	62.2	+275%
HSL	Hyperbolic	47.2	+209%

</div>

5.7 Comparison to Previous Results

Previously when conducting this experiment, the commanded gimbal rates also exceeded the maximum allowable gimbal rates during the maneuver where the initial gimbal angles were near a hyperbolic singularity. Table 5.6 show the torque error for the three steering laws during the previous experiment and Table 5.5 shows the torque error from the new experiment. After the configuration changes and the reduction in the gravitational disturbance torques, we hoped to have more control over the experiment and hopefully better duplicate the simulated results and have experimental results where the singularity avoidance algorithms better avoid the singularities; however, it is apparent that the torque error has increased from the old experiment

(a) Case 3: LG Gimbal Rates

(b) Case 3: LG Torque Error

(c) Case 3: SDA Gimbal Rates

(d) Case 3: SDA Torque Error

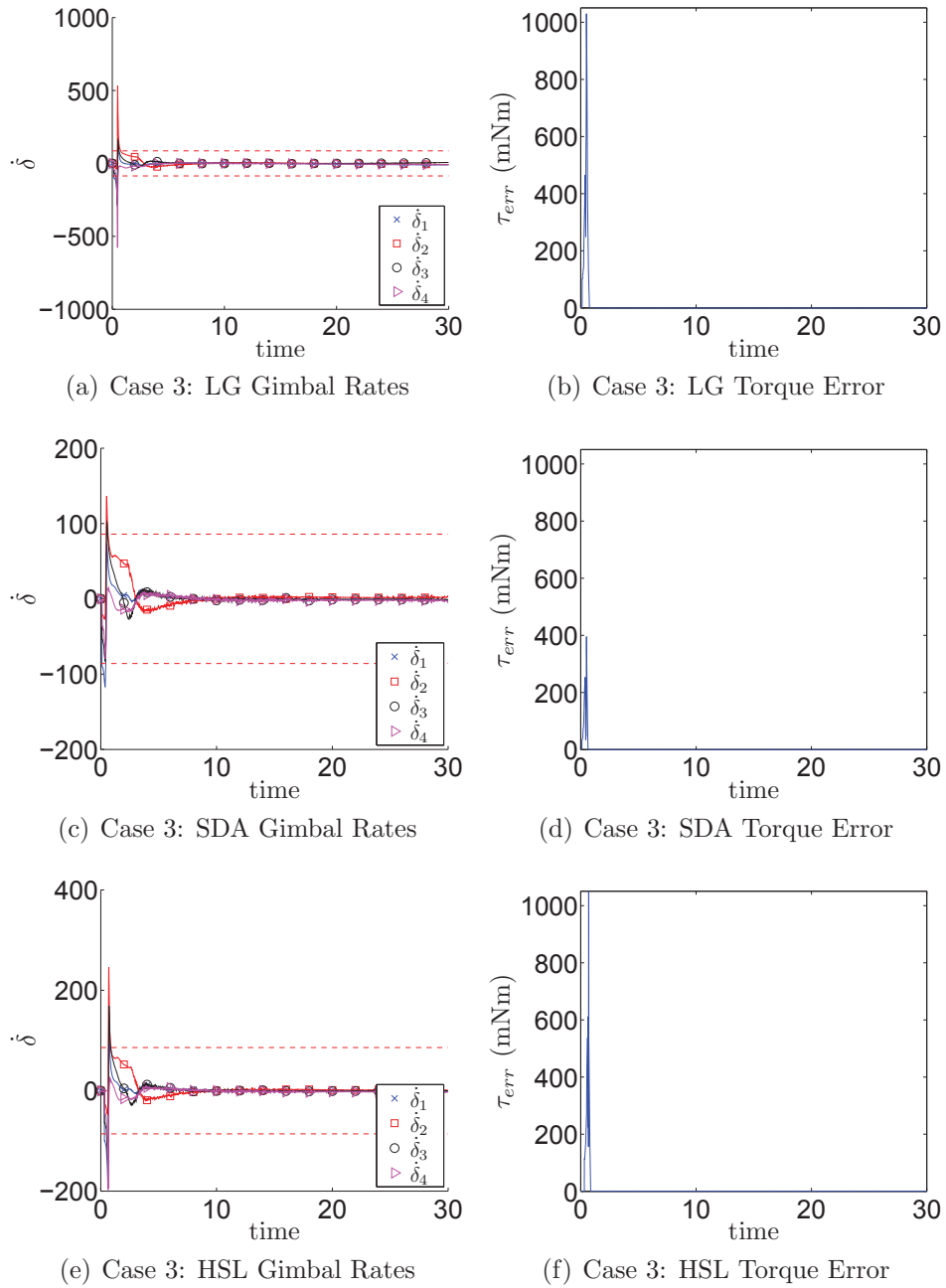(e) Case 3: HSL Gimbal Rates

(f) Case 3: HSL Torque Error

Figure 5.5. Torque Error

to the new experiment instead of decreasing as desired. These results suggest that even though we decreased the disturbance torques and have a better characterization of our platform, the other changes to the platform such as a decrease in the controller

gains resulted in a more significant impact on the torque error. However, there are two valuable pieces of information that can be obtained. The first is that with a better characterization of the MOI we can analyze the angular momentum during the maneuver and determine if the CMG array is well characterized. The second observation that can be made is that the anomaly in the third test case is repeatable, suggesting that this irregularity is not arbitrary and could be the result of another underlying cause. The underlying cause of the anomaly will be addressed in more detail in Sec. 5.7.1, but first we will analyze the angular momentum and determine if we have successfully reduced the gravitational disturbance torques and whether or not the CMG array is well characterized.

To analyze the presence of disturbance torques and determine whether or not the CMG array is well characterized we will need to compare the angular momentum of the platform during the maneuver to the estimated angular momentum of the CMG array. Since the MOI of the platform has been experimentally estimated and has an estimation accuracy of $\pm 1\%$ any errors over 1% of the total angular momentum can be attributed to disturbance torques or in a mischaracterization of the CMG array.

Figures 5.6(a), 5.6(c), and 5.6(e) are plotted from the old maneuver data. Figure 5.6(a) shows the platform angular momentum estimate, Fig. 5.6(c) shows the CMG angular momentum, and Fig. 5.6(e) shows the sum of the two. Figure 5.6(e) shows us what we refer to as momentum error. If there were no disturbance torques and our platform was perfectly characterized, then when we add the angular mo-

Table 5.6. Experimental results

Algorithm	Case	τ_{err} rms mN-m	Percent Difference
SDA	3	13.90	0
LG	3	12.63	-9
HSL	3	13.57	-2

144
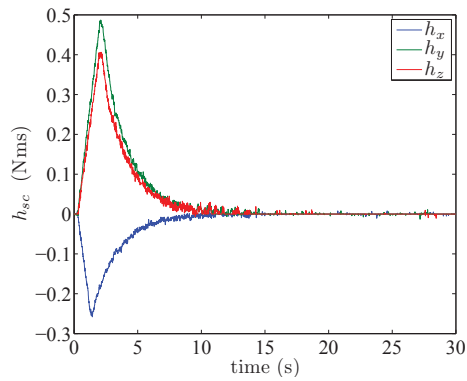
(a) Previous SimSat Platform Angular Momentum
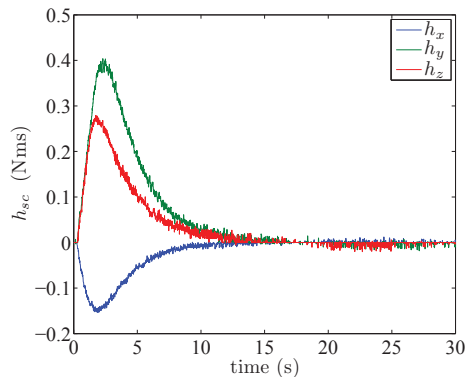
(b) New SimSat Platform Angular Momentum
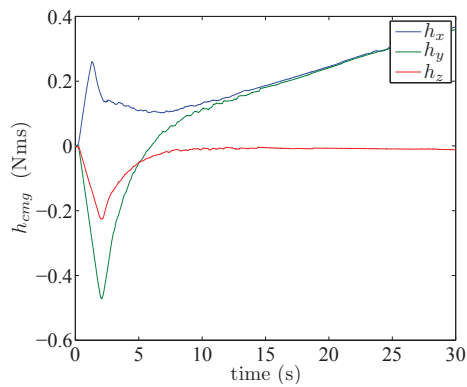
(c) Previous SimSat CMG Angular Momentum
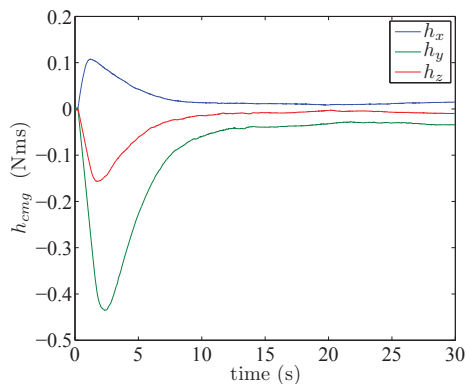
(d) New SimSat CMG Angular Momentum

(e) SDA Torque Error Near Hyperbolic Singularity

(f) HSL Torque Error Near Hyperbolic Singularity

Figure 5.6. Comparison of Previous Maneuver and Current Maneuver

mentum of the platform to the angular momentum of the CMG array we should get identically zero. We refer to a non-zero sum as the momentum error and this error suggests disturbance torques, platform mischaracterization, or a combination of both. From the first 7 seconds of Fig. 5.6(e) we see a large spike in the momentum error about the $Z-$axis that reaches a maximum at approximately four seconds. This spike c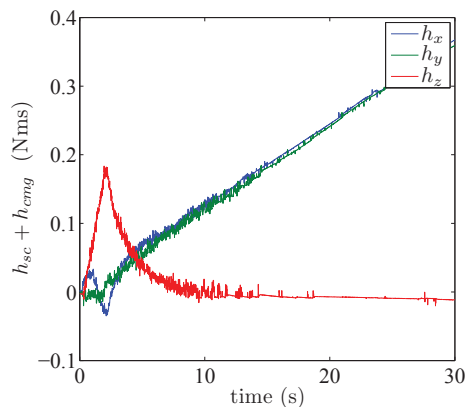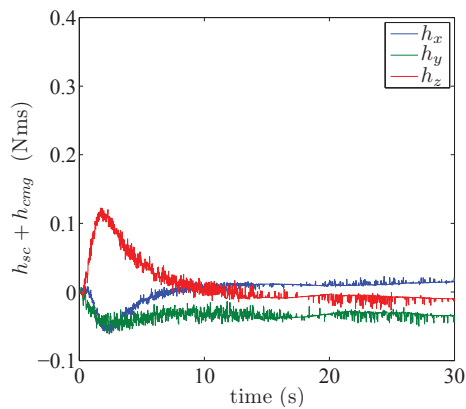orresponds to the spike in the angular momentum of the platform in Fig. 5.6(a). The strong correlation between the error and the maneuver itself suggests a mischaracterization of either the platform, the CMG array, or both. Since the platform MOI estimate is only accurate to an estimated 10% and the error shown in Fig. 5.6(e) is approximately 40% of the total angular momentum shown in Fig 5.6(a), this suggests either a mischaracterization in the CMG array or significantly less accurate MOI characterization than previously estimated.

Returning to Fig. 5.6(a), it is apparent that the maneuver is mostly complete at approximately 10 seconds. If we compare that to Fig.5.6(e), we notice a positive slope of the angular momentum in both the $X-$ and $Y-$axes suggesting disturbance torques of approximately 15 mN-m or approximately 6% of the available torque of our ACS.

The data from the new maneuver is shown in Figs. 5.6(b), 5.6(d), and 5.6(f). asdWhen we compare Fig. 5.6(b) to Fig. 5.6(a) it is apparent from the images that the new controller gains are less aggressive than the previous controller gains as the maneuver in Fig. 5.6(b) is smoother than the near bang-bang response shown in Fig. 5.6(a); additionally, during the second maneuver the platform incurs approximately 25% less angular momentum than in the previous, more aggressive maneuver. Figures 5.6(b), 5.6(d), and fig:errnew show the estimated platform angular momentum, the estimated CMG angular momentum, and the angular momentum error after the platform reconfiguration and gain changes. Figures 5.6(b) shows the lower gains

resulting in a smoother maneuver. Figure fig:errnew shows us that while the platform was maneuvering, there was an angular momentum error. This suggests that there is still a mischaracterization in either or both of the MOI and the CMG array. From the research presented in Ch. III we estimate that the MOI estimate is within $\pm 1\%$, this suggests and there is still a mischaracterization of the CMG array. It is recommended that future work include additional characterization of the CMG array. After verifying that there appear to be a decrease in the controller gains and a decrease in the disturbance torques, two potential causes for the anomalous maneuver results, we attempted to duplicate the gimbal rate anomaly in simulation. In the next section, we will develop a simplified 2-dimensional CMG array and test sensitivities to tuning parameters, time-delays, and gimbal rate saturation.

5.7.1 Identification of Sources of Gimbal Saturation.

To better understand the irregularities shown in Figures 5.5 we decided to attempt to duplicate the irregularities in simulation using SDA steering law on a simplified CMG array. This may seem counter-intuitive as this paper is primarily focused on analyzing HSL, but SDA is inherently less complicated and is designed to apply torque error to all singularities, which is why the presence of irregularities in the SDA maneuver stood out and made SDA a strong candidate for anomaly identification. To analyze the tuning parameters and attempt to duplicate the irregularities of the SDA steering law near the hyperbolic singularity, we considered the following two SGCMG array in the $X - Y$ plane. The CMG array has the following governing equations

$$\begin{bmatrix} h_x \\ h_y \end{bmatrix} = \begin{bmatrix} \cos \delta_1 + \cos \delta_2 \\ \sin \delta_1 + \sin \delta_2 \end{bmatrix}. \tag{5.67}$$

Where h_x and h_y is the angular momentum in the $X-$ and $Y-$axes respectively, δ_1

147

is the gimbal angle of the first CMG, and δ_2 is the gimbal angle of the second CMG. The CMG array has the following Jacobian

$$A = \begin{bmatrix} -\sin\delta_1 & -\sin\delta_2 \\ \cos\delta_1 & \cos\delta_2 \end{bmatrix}. \tag{5.68}$$

In order to simplify the equations, we couple the gimbal angles in a "scissor-pair" to produce a torque in only one axis. To construct the scissor pair, we apply the following constraint

$$\delta_2 = \pi - \delta_1 \tag{5.69}$$

which results in a scissor pair about the $Y-$axis and simplifies Eqs. (5.67) and (5.68) to

$$\begin{bmatrix} h_x \\ h_y \end{bmatrix} = \begin{bmatrix} 0 \\ 2\sin\delta_1 \end{bmatrix} \tag{5.70}$$

and

$$A = \begin{bmatrix} 0 \\ 2\cos\delta_1 \end{bmatrix} \tag{5.71}$$

respectively. If we originally desired a torque from this CMG array of 1 in the Y-axis, we can represent the CMG array in one dimension with the following characteristics

$$h = 2\sin\delta$$
$$\delta_0 = 0$$
$$\dot{h}_{des} = 1 \tag{5.72}$$
$$A = 2\cos\delta$$

where h is the angular momentum, δ is the gimbal angle, δ_0 is the gimbal angle at the start of the simulation, A is the Jacobian, and $\dot{h}_{des}$ is the desired torque from the CMG array. If we apply the MPPI steering law, our commanded gimbal rate $\dot{\delta}$ is calculated as

$$\dot{\delta} = A^{-1}\dot{h}_{des}. \tag{5.73}$$

For the first simulation, we implemented the MPPI steering at controller update frequency of 100 Hz. Figure 5.7 shows the gimbal angles and gimbal rates as the CMG approach the singularity at $\pi/2$. As expected, as A approaches zero A^{-1} becomes incredibly large, resulting in very large gimbal rates. Since the large gimbal rates associated with singularity are undesirable, we implemented SDA steering law and repeated the simulation.
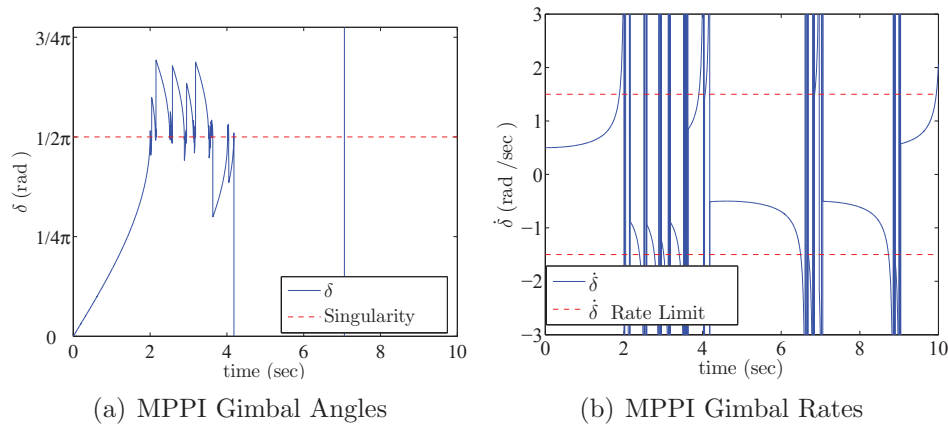

(a) MPPI Gimbal Angles   (b) MPPI Gimbal Rates

Figure 5.7. Results of Maneuver Implemented with MPPI Steering Law

To implement SDA steering law on the CMG array, we define the following parameters

149

$$m = \sigma_1 = A$$

$$\gamma(m) = \gamma_0 e^{(-\mu m)} \tag{5.74}$$

$$A^{sda} = \frac{A}{A^2 + \gamma(m)}$$

where m is the singularity measure, $\gamma(m)$ is the SDA avoidance term and is dependent on the singularity measure, γ_0 and μ are the SDA tuning parameters, and A^{sda} is the SDA modified control matrix. Once we have A^{sda} defined we can calculate the desired gimbal rates $\dot{\delta}$ as

$$\dot{\delta} = A^{sda} \dot{h}_{des}. \tag{5.75}$$

To best duplicate the experimental results, we chose the following tuning parameters, identical to the terms used for SDA in the previous experiments

$$\begin{array}{c} \gamma_0 = .01 \\ \mu = 1 \end{array}. \tag{5.76}$$

We then repeated the simulation with the controller update frequency at 100 Hz to approximate a maneuver with nearly-continuous controller updates. The results of the simulation are shown in Fig. 5.8. Figure 5.8(a) shows the gimbal angles for the simulation start at 0 and approach the singularity at $\pi/2$. Figure 5.8(b) shows the gimbal rates for the simulation. As expected, the SDA steering law drives the gimbal rate to zero as the array approaches the singularity at δ of $\pi/2$, but it is also important to point out that before the gimbal rates are driven to zero there is a short amount of time where gimbal rates of over 2.5 rad/sec are commanded, well over the rate limit of 1.5 rad/sec. This suggests that the small tuning parameters used in this simplified one-dimensional simulation, which were taken from the experiment, can lead to the large torque errors associated with gimbal rate saturation. Additionally,

there appears to be no apparent irregularities due to the discontinuous controller update for a controller update frequency of 100 Hz.

(a) Gimbal Angle with Original Tuning Parameters

(b) Gimbal Rate with Original Tuning Parameters
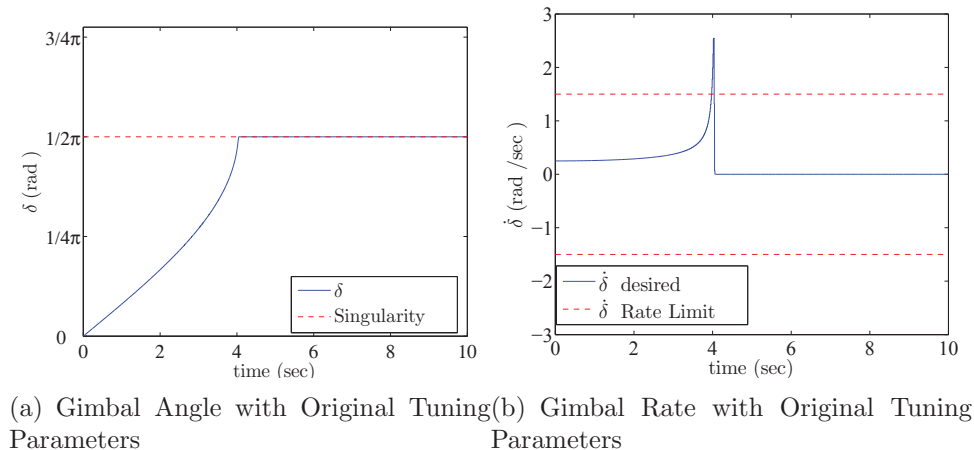
Figure 5.8. Gimbal Angle and Gimbal Rate with Original Tuning Parameters and 100 Hz Update Frequency

In addition to small tuning parameters leading to the irregularities in the primary experiment, we hypothesized that the controller update frequency might be a potential source of the irregularities. As a result, we repeated the SDA simulation with a controller update frequency of 10 Hz. The results are shown in Fig. 5.9. Similar to the gimbal rates experienced in the 100 Hz simulation, as the CMG approaches singularity the gimbal rates spike to over 2.5 rad/sec. However, due to the low update frequency the gimbal angle overshoots the desired gimbal angle of $\pi/2$ and begins a violent chatter about the singular position. This suggests that the controller update frequency must also be considered when considering tuning parameters.

Upon considering the results from Figs. 5.8 and 5.9 we decided to adjust the tuning parameters in an attempt to better satisfy the system limitations of SimSat. We repeated the simulation with

(a) Gimbal Angle with Original Tuning Parameters (b) Gimbal Rate with Original Tuning Parameters
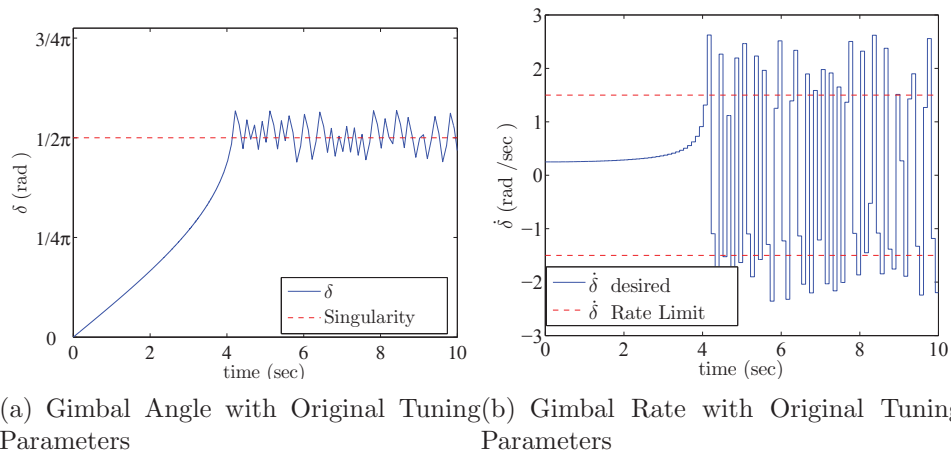
Figure 5.9. Gimbal Angle and Gimbal Rate with Original Tuning Parameters and 10 Hz Update Frequency

$$\begin{aligned} \gamma_0 &= .1 \\ \mu &= 6 \end{aligned} \qquad (5.77)$$

The results of the simulation are shown in Fig. 5.10. In Fig. 5.10(b) we see that the gimbal rates stay within the gimbal saturation rates of 1.5 rad/sec and Fig. 5.10(a) shows that the gimbal angle decays to the desired gimbal angle of $\pi/2$.

(a) Gimbal Angle with Original Tuning Parameters (b) Gimbal Rate with Original Tuning Parameters

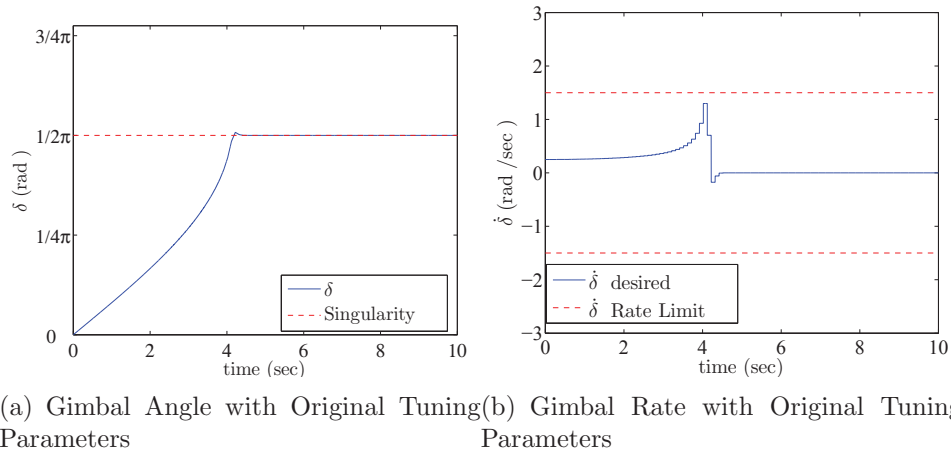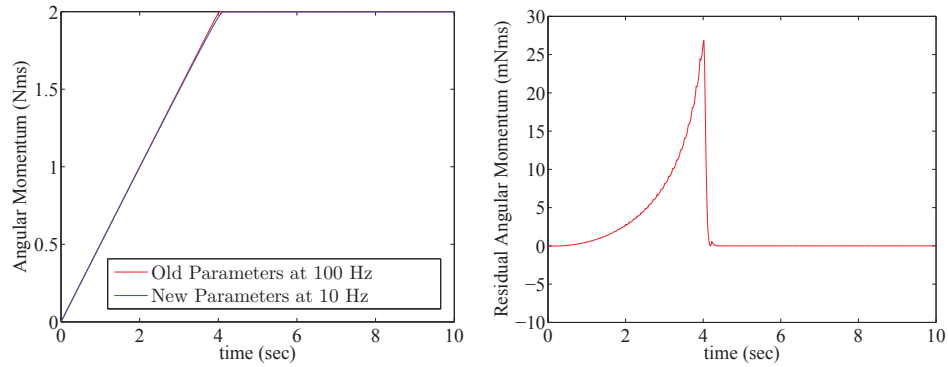**Figure 5.10. Gimbal Angle and Gimbal Rate with New Tuning Parameters and 100 Hz Update Frequency**

(a) Comparison of Angular Momentum with Old and New Tuning Parameters

(b) Increase in Torque Error from Increasing Tuning Parameters

Figure 5.11. Momentum Comparison of Previous and New Tuning Parameters

5.8   HSL Conclusion

The purpose of the experiment presented in this chapter was to experimentally analyze the CMG steering law developed by Leve [21]. After implementing LG, SDA, and HSL on SimSat and analyzing the results we concluded that the experimental results of this research concur with Leve's [22] simulated results while away from singularity. Our experimental data showed both a reduction in the RMS null motion and torque error were achieved by implementing HSL. When away from singularity HSL reduced the amount of torque error by around 90% and null motion by approximately 85%. Unfortunately, none of the three controllers were able to successfully avoid the hyperbolic singularity, and all three exceeded the hard rate limits set on SimSat. These rate limits in-turn resulted in a disturbance torque more than 10x larger than the torque error commanded by the singularity avoidance algorithms. After duplicating the irregularity in simulation, the researchers believe that SimSat was unable to avoid the singularity due to a slow controller update rate of 10 Hz and singularity avoidance constants that were too low relative to our on-board controller gains. Future work is suggested to both increase the gimbal rate refresh rate and

153

analyze and select platform specific singularity avoidance tuning parameters.

VI. Conclusions and Future Work

The future goal of this research was to implement feed-forward optimal control solutions on SimSat. However, after researching current characterization methods for terrestrial-based satellite attitude simulators it was concluded that we must first develop accurate and precise platform characterization methods. This began with a novel MOI estimation method followed by an active torque reduction methodology. After the success of the novel characterization and torque reduction methodologies, we decided to readdress the previously inconclusive research on the hardware validation of Hybrid Steering Logic (HSL) on SimSat. The conclusions of the three research topics will now be presented.

6.1 MOI Estimation

In Chapter III, a method for dynamic estimation of the MOI matrix was proposed and evaluated. This procedure started with the identification of some presumed error sources, specifically first-order torques and errors associated with time delays. The previous assumptions–trivial first-order disturbance torques, well defined time delays, and the ability to perform a pure rotation about a single axis–were analyzed and shown to be invalid for SimSat. It was concluded that a deviation from more traditional methods should be made so a modified version of MOI method for POI estimation created by Wiener [39] was implemented and evaluated. Previous researchers used a step maneuver for MOI estimation which was analyzed and deemed inefficient, noisy, and possibly unable to account for time delays. A new maneuver was proposed, implemented, and analyzed in this research that kept a larger percentage of data, could be curve fit for better noise rejection, and was experimentally shown to be insensitive to time delays. In addition, the first-order disturbance torques were

analyzed and deemed non-trivial while the second-order disturbance torques were experimentally verified trivial for maneuvers smaller than 5°. Since the developed maneuver is approximately $\pm 2.18°$, a method was proposed and implemented to estimate and remove angular momentum associated with the zero-and first-order disturbance torques. The experimental result was the identification and correction of the first-order disturbance torques resulted in the identification and correction of an otherwise indiscernible 6.5% erroneous bias in the MOI estimate about the $X-$axis. The three components of the new MOI estimation process–methodology, maneuver, and correction of disturbance torques–were combined and experimentally evaluated on SimSat. The result was an MOI matrix that was calculated from an overdetermined set of MOI estimates resulting in an average percent deviation of approximately 0.09% and a 96% improvement over the previous methodology [6].

6.2 Disturbance Torque Identification and Reduction

In Chapter IV, we experimentally identified and then developed and analyzed a method to actively correct for gravitational disturbance torques. Chapter IV started by presenting a torque characterization maneuver that confirmed the invalidity of the rigid body assumption on AFIT's satellite simulator called SimSat. We identified a second significant first-order disturbance torque which accounted for 14% of the available torque at a rotation of 15° about an axis in the $X - Y$ plane. Upon evaluating the potential sources of disturbance torques, we hypothesized that the disturbance torque was due to structural deflections and added structural reinforcements and reduced the ballast mass to decrease structural deflections. The torque characterization process was repeated, with a 91% decrease in first-order disturbance torques and a 87% decrease in all torques when evaluated at 15° rotation about a test axis in the $X - Y$ plane. In order to further decrease the disturbance torques, we added three

linear torque actuators to actively counteract the disturbance torques which resulted in an additional 55.7% decrease in first-order torques and 47% decrease in all disturbance torques when evaluated at a 15° rotation about the $X - Y$ plane. The total gravitational disturbance torque was decreased from approximately 14.92% to approximately 1.08% of SimSat's available torque when rotated 15° about an axis in the $X - Y$ plane. Additionally, enabling the linear actuators resulted in a 73% decrease in total disturbance torques when evaluated at 5°, dropping the gravitational disturbance torque to approximately 0.18% of the available torque. The result of this research suggests that the rigid body assumption should always be verified on satellite simulators. Additionally, this research provides a maneuver methodology to analyze the rigid body assumption. In the event that the platform fails the rigid body assumption, the equations of the dynamic imbalance can be calculated from the proposed torque characterization maneuver. A set of linear actuators can then be programmed to counteract not just the zero and first-order component of the dynamic imbalance but higher-order torques as well.

6.3   Hardware Testing of HSL

The purpose of the experiment presented in Chapter V was to experimentally analyze the CMG steering law developed by Leve [21]. After implementing LG, SDA, and HSL on SimSat and analyzing the results we concluded that the experimental results of this research concur with Leve's [22] simulated results while away from singularity. Our experimental data showed both a reduction in the RMS null motion and torque error were achieved by implementing HSL. When away from singularity HSL reduced the amount of torque error by around 90% and null motion by approximately 85%. Unfortunately, none of the three controllers were able to successfully avoid the hyperbolic singularity, and all three exceeded the hard rate limits set on SimSat. These

rate limits in-turn resulted in a disturbance torque more than 10x larger than the torque error commanded by the singularity avoidance algorithms. While exceeding rate limits near the hyperbolic singularity, HSL was unable to induce less torque error than SDA. The researchers believe that SimSat was unable to avoid the singularity due to a slow controller update rate of 10 Hz and singularity avoidance constants that were too low relative to our on-board controller gains. In order to verify that these were potential sources of the irregularity, a simple 2 SGCMG array was designed in simulation to analyze the tuning parameters and the update frequency. It was concluded that the tuning parameters result in gimbal rates of approximately 2.5 radians per second, larger than the gimbal saturation rate of 1.5 radians per second. Additionally, the controller update frequency 10 Hz caused a violent chatter when the CMG array approached singularity. The tuning parameters were increased and the simulation was repeated, resulting in neither gimbal rate saturation nor gimbal chatter. We suggest that future work focus on developing a method to choose the tuning parameters to best meet the platform capabilities and mission requirements.

6.4 Future Work

The research in Chapter III developed a new method for in-flight MOI estimation and made claims to precision by by analyzing and correcting for disturbance torques and over-determining the MOI estimation equations to allow for analysis of the residual between the single axis estimation and the best-fit MOI ellipsoid. We propose future work to include a direct measurement of the MOI and POI to validate the experimental in-flight results. Additionally, the MOI estimation process was able to correct for time delays but in doing so was also able to identify the time delays. Because time delays were one of the main reasons for not implementing an EKF for MOI estimation, future work could include using the time delays estimated from

the proposed MOI estimation methodology to implement a real-time MOI estimation methodology.

Chapter IV developed and analyzed a methodology for identifying and correcting for first- to third-order gravitational disturbance torques. Future research would involve simultaneously estimating the static imbalance as well as the dynamic imbalance. A key to this research path is to keep in mind that the solution to such estimation is underdetermined and an artificial constraint such as choosing the imbalance in the $Z-$axis that minimizes the two-norm of the deflections in the $X-$ and $Y-$axes should be implemented. Additionally, the linear actuators are currently wired to take an input position signal in the form of a 0-5 V input and use a controller on the actuator itself to close the loop with the position based potentiometer to reach the desired position. Throughout this research, we have concluded that the onboard controller algorithm discards small changes in position resulting in a series of 0.5 cm step-maneuvers as opposed to the desired maneuver that resembles a ramp. For future work, it is suggested that an Arduino® board be used to interpret the 0-5 V desired position input and control the actuator by providing an extend and contract command signal while using the actuators' position potentiometer output to close the control loop. The Arduino® board can calculate the control signal at a much higher rate than the on-board controller–allowing for better tracking of the desired actuator position– and with the ability to reprogram the desired control algorithm we should be able to decrease the noise rejection thresholds and allow for a better ramp response.

The increased mass characterization and disturbance torque correction presented in Chapters III and IV should allow for better a-priori calculations of optimal control solutions. This is a key component to near real-time implementation of optimal control solutions. The results from Chapter V suggest that the controller update

frequency of 10 Hz may be insufficient to avoid the CMG singularities on SimSat. Although the singularities may be avoidable with larger singularity avoidance tuning parameters, an increase in the tuning parameters would also mean an increase in the null-motion and torque error. We suggest future work in analyzing the singularity avoidance tuning parameters as a function of the gimbal rate update frequency to not only develop a methodology for choosing the singularity tuning parameters but also to determine how the operational torque errors increase with a decrease in gimbal rate command frequency. After the tuning parameters are chosen to suit the operational constraints of SimSat, we recommend repeating the HSL experiment on SimSat with the new tuning parameters.

In addition to research topics, there are some hardware specific modifications that we would suggest making to SimSat. The first would be to add a PhaseSpace motion capture system for external monitoring of SimSat orientation. This would allow us to correct for IMU drift and would allow for more repeatable experiments. Additionally, we recommend adding an Arduino® board attached to two current sensors, two voltage sensors, an alarm, and an on-board digital readout. This would allow us to monitor not only the voltage of the two on-board batteries, but also the amount of power that each battery provided to reach said voltage. The primary objective of this setup is to identify and avoid low-voltage scenario which results in damage to the electronics and incomplete experiments. The secondary benefit is that an integration of the current sensors would provide an easy reference to the percentage of battery consumption which for Lithium-Polymer batteries cannot easily be ascertained from the voltage. In addition to the percentage of battery consumption, a readout of the integrated battery current could also provide an early indication of battery failure if the battery reaches critical voltage before reaching its integrated amp rating of 5.5 Ah.

6.5 Summary

In this research we developed a novel methodology for characterizing the MOI of a terrestrial-based satellite attitude simulator. Afterwards, we analyzed the higher-order disturbance torques experienced by terrestrial-based satellite attitude simulators and implemented linear actuators to counteract the disturbance torques. We experimentally estimated the MOI to within an estimated 0.09% and reduced the gravitational disturbance torques from 14.92% to 1.18% of the available torque at 15° deflection. After estimating the MOI and counteracting the disturbance torques we readdressed the hardware validation of HSL. What we found is that after the configuration changes all three CMG steering algorithms analyzed were still unable to avoid the hyperbolic singularity. We were able to duplicate a similar anomaly in simulation and conclude that the tuning parameters should be chosen to better account for SimSat gimbal rate saturation limits and a controller update frequency of 10 Hz.

Bibliography

[1] N. Bedrossian. *Steering Law Design for Redundant Single Gimbal Control Moment Gyro Systems.* MS thesis, Massachusetts Institute of Technology, August 1987.

[2] R. Bordany, W. H. Steyn, and M. Crawford. "In-Orbit Estimation of the Inertia Matrix and Thruster Parameters of UoSAT-12," *22nd Annual AIAA/USU Conference on Small Satellites.* Logan, Utah, 2000. AIAA/USU.

[3] S. Chesi, Q. Gong, V. Pellegrini, R. Cristi, and M. Romano. Automatic mass balancing of a spacecraft three-axis simulator: Analysis and experimentation. *Journal of Guidance, Control, and Dynamics*, 37(1):197–206, 2014.

[4] J. E. Colebank, R. D. Jones, G. R. Nagy, R. D. Pollack, and D. R. Mannebach. *SIMSAT: A Satellite System Simulator and Experimental Test Bed for Air Force Research.* MS thesis, Air Force Institute of Technology (AU), March 1999.

[5] D. E. Cornick. "Singularity Avoidance Control Laws for Single Gimbal Control Moment Gyros," *Guidance and Control Conference.* Boulder,CO, 1979. AIAA.

[6] V. J. Dabrowski. *Experimental demonstration of an Algorithm to Detect the Presence of a Parasitic Satellite.* MS thesis, Air Force Institute of Technology (AU), March 2003.

[7] P. A. Ferguson. "On-Orbit Spacecraft Inertia and Rate Sensor Scale Factor estimation for Microsatellites," *22nd Annual AIAA/USU Conference on Small Satellites.* Logan, Utah, 2008. AIAA/USU.

[8] K. Ford and C. Hall. "Singular Direction Avoidance Steering for Control-Moment Gyros," *Guidance, Navigation and Control Conference. Journal of Guidance Control and Dynamics*, 23(4):648–656, 2000.

[9] B. Fornberg. *A Practical Guide to Pseudospectral Methods.* Cambridge University Press, 1995.

[10] D. Gallardo, R. Bevilaxqua, and R. Rasmussen. "Advances on a 6 Degrees of Freedom Testbed for Autonomous Satellites Operations," *Guidance, Navigation and Control Conference.* Portland, Oregon, August 2011. AIAA.

[11] J. W. Geitgey. *The Determination of Remaining Satellite Propellant using Measured Moments of Inertia.* Ms thesis, Air Force Institute of Technology (AU), March 2006.

[12] N. Hatcher and R. Young. "An Automatic Balancing System for Use on Frictionlessly Supported Attitude-Controlled Test Platforms,". volume 227, Langley Research Center, August 2013. NASA TN D-4426.

[13] M. S. Hines. *Fuel Estimation Using Dynamic Response.* MS thesis, Air Force Institute of Technology (AU), March 2007.

[14] D. Kalman. A singularly valuable decomposition: The svd of a matrix. *The College Mathematics Journal*, 27(1):2–23, 1996.

[15] B. Kim, E. Velenis, P. Kriengsiri, and P. Tsiotras. "A Spacecraft Simulator for Research and Education," *Proceedings of the AIAA/AAS Astrodynamics Specialists Conference, no. AAS 01-367.* Quebec City, Canada, August 2001. AIAA/AAS.

[16] D. H. Kim, D.-G. Choi, and H.-S. Oh. "Inertia Estimation of Spacecraft Based on Modified Law of Conservation of Angular Momentum". *Journal of Astronomy and Space Sciences*, 4(27):353–357, 2010.

[17] J.-J. Kim and B. N. Agrawal. "System Identification and Automatic Mass Balancing of Ground-Based Three-Axis Spacecraft Simulator," *2006 American Institute of Aeronautics and Astronautics, Guidance Navigation and Control.* Keystone, CO, August 2006. AIAA.

[18] J. J. Kim and B. N. Agrawal. Automatic mass balancing of air-bearing-based three-axis rotational spacecraft simulator. *Journal of Guidance, Control, and Dynamics*, 32(3):1005–1017, 2009.

[19] J. J. Kim and B. N. Agrawal. "System Identification and Automatic Mass Balancing of Ground-Based Three-Axis Spacecraft Simulator," *Guidance, Navigation and Control.* volume 32, pages 1005–1017, Chicago, IL, 2009. American Institute of Aeronautics and Astronautics.

[20] A. Y. Lee and J. A. Wertz. "In-Flight Estimation of the Cassini Spacecraft's Inertia Tensor". *Journal of Spacecraft and Rockets*, 39(1):153–154, 2002.

[21] F. A. Leve. *Novel Steering and Control Algorithms for Single-Gimbal Control Moment Gyroscopes.* PhD thesis, The University of Florida, 2010.

[22] F. A. Leve and N. G. Fitz-Coy. Hybrid Steering Logic for Single-Gimbal Control Moment Gyroscopes. *Journal of Guidance Control and Dynamics*, 33(4):1202–1212, 2010.

[23] Y. Li and Y. Gao. "Equations of Motion for the Automatic Balancing system of 3-DOF Spacecraft Attitude Control Simulator," *Third International Symposium on Systems and Control in Aeronautics and Astronautics (ISSCAA).* pages 248–251, Harbin, China, June 2010. IEEE.

[24] Y. Liu, J. Zhou, H. Chen, and X. Mu. "Experimental research for flexible satellite dynamic simulation on three-axis air-bearing table". *Journal of Aerospace Engineering*, 227:369–380, 2013.

[25] C. G. McChesney. *Design of Attitude Control Actuators for a Simulated Spacecraft.* MS thesis, Air Force Institute of Technology (AU), March 2011.

[26] C. D. McFarland. *Near Real-Time Closed-Loop Optimal Control Feedback for Spacecraft Attitude Maneuvers.* MS thesis, Air Force Institute of Technology (AU), March 2009.

[27] H. L. Mork and P. C. Wheeler. "Three-Axis Attitude Control System Air-Bearing Tests with Flexible Dynamics," *AIAA Guidance and Control Conference.* Key Biscayne, FL, August 1973. AIAA.

[28] M. C. Norman, M. A. Peck, and D. J. O'Shaughnessy. In-orbit estimation of inertia and momentum-actuator alignment parameters. *Journal of Guidance, Control, and Dynamics*, 34(6):1798–1814, 2011.

[29] J. Prado, G. Bisiacchi, L. Reyes, E. Vicente, F. Contreras, M. Mesinas, and A. Juarez. Three axis air bearing based platform for small satellite attitude determination and control simulation. *Journal of Applied Research and Technology*, 3(3):222–237, 2005.

[30] N. R. Roach, W. C. Rohe, and N. F. Welty. *A Systems Engineering Approach to the Design of a Spacecraft Dynamics and Control Testbed.* MS thesis, Air Force Institute of Technology (AU), March 2008.

[31] J. L. Schwartz and C. D. Hall. "System Identification of a Spherical Air-Bearing Spacecraft Simulator," *Proceedings of the 14th AAS/AIAA, Space Flight Mechanics Meeting.* Maui, HI, February 2004. AAS/AIAA.

[32] J. L. Schwartz, M. A. Peck, and C. D. Hall. Historical Review of Air-Bearing Spacecraft Simulators. *Journal of Guidance Control and Dynamics*, 26(4):446–452, 2003.

[33] M. Sidi. *Spacecraft dynamics and control : a practical engineering approach.* Cambridge University Press, Cambridge New York, 1997.

[34] G. A. Smith. "Dynamic Simulators for Test of Space Vehicle Attitude Control Systems," *Proceedings of the Conference on the Role of Simulation in Space Technology, Part C.* Blacksburg, VA, 1964. Virginia Polytechnic Inst. and State University.

[35] S. Tanygin and T. Williams. Mass property estimation using coasting maneuvers. *Journal of Guidance, Control, and Dynamics*, 20(4):625–632, 1998.

[36] S. P. Viswanathan, A. Sanyal, and L. Holguin. "Dynamics and Control of a Six Degrees of Freedom Ground Simulator for Autonomous Rendezvous and Proximity Operation of Spacecraft," *Guidance, Navigation and Control Conference.* Minneapolis, Minnesota, August 2012. AIAA.

[37] R. K. Wangsness. *Introduction to Theoretical Physics, Classical Mechanics and Electrodynamics.* John Wiley and Sons, Inc., 1963.

[38] B. Wie, D. Bailey, and C. Heiberg. Singularity robust steering logic for redundant single-gimbal control moment gyros. *Journal of Guidance, Control, and Dynamics*, 24(5):865–872, 2001.

[39] K. Wiener and R. Boynton. "Using the "Moment of Inertia Method" to Determine Product of Inertia," *51st Annual Conference of the Society of Allied Weight Engineers.* Hartford, CT, May 1992. S.A.W.E.

[40] J. Wright and E. Swenson. "Comparison of Statically Optimized Proportional-Integral-Derivative and Functionally Optimized Controllers," *Guidance, Navigation and Control Conference.* Minneapolis, MN, August 2012. AIAA.

[41] J. Wright, E. Swenson, and F. Leve. "Hardware Testing of Hybrid Steering Logic for Single-Gimbal Control Moment Gyroscopes," *Guidance, Navigation and Control Conference.* Minneapolis, MN, August 2012. AIAA.

[42] J. S. Young. *Development of an Automatic balancing System for a Small Satellite Attitude Control Simulator.* Master's thesis, Utah State University, 1998.

[43] R. A. Zeledon and M. A. Peck. "Singularity-Free Constrained Steering Law for Triplet Control Moment Gyros," *Guidance, Navigation and Control Conference.* Toronto, ON, Canada, August 2010. AIAA.

REPORT DOCUMENTATION PAGE

The public reporting burden for this collection of information is estimated to average 1 hour per response, including the time for reviewing instructions, searching existing data sources, gathering and maintaining the data needed, and completing and reviewing the collection of information. Send comments regarding this burden estimate or any other aspect of this collection of information, including suggestions for reducing the burden, to Department of Defense, Washington Headquarters Services, Directorate for Information Operations and Reports (0704-0188), 1215 Jefferson Davis Highway, Suite 1204, Arlington, VA 22202-4302. Respondents should be aware that notwithstanding any other provision of law, no person shall be subject to any penalty for failing to comply with a collection of information if it does not display a currently valid OMB control number.
PLEASE DO NOT RETURN YOUR FORM TO THE ABOVE ADDRESS.

1. REPORT DATE *(DD-MM-YYYY)*	2. REPORT TYPE	3. DATES COVERED *(From - To)*
26 Mar 2015	Dissertation	September 2010 - March 2015

4. TITLE AND SUBTITLE

Advancements of In-Flight Mass Moment of Inertia and Structural Deflection Algorithms for Satellite Attitude Simulators

5a. CONTRACT NUMBER

5b. GRANT NUMBER

5c. PROGRAM ELEMENT NUMBER

6. AUTHOR(S)

Wright, Jonathan W, Capt, USAF

5d. PROJECT NUMBER

5e. TASK NUMBER

5f. WORK UNIT NUMBER

7. PERFORMING ORGANIZATION NAME(S) AND ADDRESS(ES)

Air Force Institute of Technology
Graduate School of Engineering and Management (AFIT/EN)
2950 Hobson Way
Wright-Patterson AFB OH 45433-7765

8. PERFORMING ORGANIZATION REPORT NUMBER

AFIT-ENY-DS-15-M-261

9. SPONSORING/MONITORING AGENCY NAME(S) AND ADDRESS(ES)

Intentionally Left Blank

10. SPONSOR/MONITOR'S ACRONYM(S)

11. SPONSOR/MONITOR'S REPORT NUMBER(S)

12. DISTRIBUTION/AVAILABILITY STATEMENT

Distribution Statement A. Approved for Public Release; Distribution Unlimited

13. SUPPLEMENTARY NOTES

This work is declared a work of the U.S. Government and is not subject to copyright protection in the United States.

14. ABSTRACT

Experimental satellite attitude simulators have been used to test and analyze control algorithms; driving down risk before implementation on operational satellites. Ideally, the dynamic response of a terrestrial-based experimental satellite attitude simulator matches that of an on-orbit satellite. Unfortunately, gravitational disturbance torques and poorly characterized moments of inertia introduce uncertainty into the system dynamics leading to questionable experimental results. This research consists of three distinct, but related contributions to the field of developing robust satellite attitude simulators. First, existing approaches to estimate mass moments and products of inertia are evaluated followed by a proposition and evaluation of a new approach that increases both the accuracy and precision of these estimates using typical on-board satellite sensors. Next, to better simulate the micro-torque environment of space, a new approach to mass balancing satellite attitude simulator is presented, experimentally evaluated, and verified. Finally, we experimentally analyzed a control moment gyroscope singularity avoidance steering law.

15. SUBJECT TERMS

satellite attitude dynamics and controls, satellite attitude simulator, air bearing, satellite, attitude, simulator, simsat, moment of inertia, MOI, structural deflection, hybrid steering logic, HSL, control moment gyroscope, CMG

16. SECURITY CLASSIFICATION OF:			17. LIMITATION OF ABSTRACT	18. NUMBER OF PAGES	19a. NAME OF RESPONSIBLE PERSON
a. REPORT	b. ABSTRACT	c. THIS PAGE			Dr. Eric D. Swenson, AFIT/ENY
U	U	U	UU	181	19b. TELEPHONE NUMBER *(Include area code)* (937) 255-3636 x 7479 eric.swenson@afit.edu

Standard Form 298 (Rev. 8/98)
Prescribed by ANSI Std. Z39.18